Cladding of High Hardness Materials by Directed Energy Deposition

Yoko Hirono

A Thesis for the Degree of Ph.D. in Engineering

Cladding of High Hardness Materials by Directed Energy Deposition

2024

Graduate School of Engineering
Kyoto University

Yoko Hirono

Table of Contents

* Stellite is a trademark of Kennametal Inc.

1 Introduction

The additive manufacturing (AM) industry has grown significantly since the first patent was granted in 1986 [1]. The global metal and polymer AM market size in 2021 was valued at EUR 8.33 billion [2]. AM has since evolved into one of the most promising future-oriented manufacturing technologies [3]. Because of the transition of AM from rapid to functional prototyping [4], AM has historically been used in diverse industries, including aerospace and automobiles [5], [6], [7].

Among the AM techniques, directed energy deposition (DED) is suitable not only for part fabrication from scratch but also for dissimilar metal joining, partial coating, graded metal creation, repairing damaged parts, and creating functionally improved materials [8], [9]. This is because DED allows additional materials to be added to an existing workpiece in specific areas. To maximize these features and improve productivity, a new type of hybridization that combines DED with traditional subtractive machining process has been studied [10]. Thus, DED has had a high adoption level in industry, especially in aerospace [11], [12].

DED enables the addition of high hardness materials to the surface of inexpensive base materials in critical areas, thereby reducing manufacturing costs and waste. Consequently, DED applications have recently spread increasingly into new industrial fields, producing hard facing of molds and dies used for cold press forming processes, gear teeth, bearing seats, rotary cutting dies, and cam shaft [13], [14]. Furthermore, wear resistant coating and cladding fabrication by DED has been rapidly increasing, with alloy tool steels and other materials often preferred [15]. Specifically, high-speed steel and Stellite, a Co-based superalloy, are typically used in hard facing applications [16], [17].

For these applications, maintaining both hardness and preventing cracking is paramount. However, a trade-off is made between high hardness and low crack frequency. Predicting and controlling hardness and cracks remains a challenge; therefore, determining the appropriate deposition conditions is crucial. To obtain the appropriate deposition conditions, researchers previously focused on melt pool condition as one index to predict the properties of a deposited workpiece and evaluate the relationship between the melt pool conditions and geometry of the deposited test pieces [18]. The obtained results have been utilized to control the laser power and feed rate for maintaining the melt pool temperature at the desired value during deposition processes. However, achieving the desired geometry does not necessarily mean that better mechanical properties will be obtained. Therefore, understanding the mechanical properties that are temperature-history dependent is important because the DED process includes melting and solidification cycles.

Some studies have attempted to obtain the deposition conditions for high hardness materials through experiments. Rahman et al. found out that the micro-hardness of laser metal deposited vanadium-rich high-speed steel could be improved by increasing the laser processing speed [19]. Tekumalla et al. investigated the hardness and microstructure of high-speed steel with different vanadium content ratios [20]. However, few studies discuss how the temperature history should be controlled or attempt to control or design the temperature history at a practical level.

Moreover, many researchers have used various approaches in an attempt to suppress or prevent cracking of the deposited material, substrate material, or between the two of them [15], [21]. Regarding the deposited Co-based superalloys, although substrate preheating effectively prevents cracking, surface hardness has been found to decrease upon preheating, with a maximum decrease of 10 HRC (171 HV) [22]. This negative outcome must be resolved because Co-based superalloys are beneficial for hard facing applications.

The objective of this study is thus to develop methodologies for achieving hard, crack-free claddings in practical applications. The applicable materials focused on are high-speed steel and Stellite, which are in high demand in hard facing applications in industrial fields. To achieve this objective, the following two methodologies are applied.

1) This study investigates the range of cooling rates and thermal histories that can be achieved under practical deposition conditions.
2) This study clarifies the deposition strategy for producing hard, crack-free depositions of high-speed steel and Stellite by considering the influence of the cooling rate and thermal history.

The organization of the thesis is as follows. Chapter 2 summarizes the status and challenges of DED in hard facing applications. By referring to past research, the mechanisms that influence hardness and clacking during deposition are described. Thereafter, the main theme pertaining to the control of temperature history is stated. Chapter 3 describes the investigation on the cooling rate of the workpiece, which influences the hardness and crack development in practical applications of DED. A methodology for estimating the cooling rate during the deposition process was developed. Chapter 4 describes the experimental investigation on the deposition condition for the Co-based super alloy, Stellite#6, to achieve hard, crack-free coatings. The influence of laser power and preheating on the hardness and crack development is discussed to clarify the decrease in hardness owing to preheating that was reported in a previous study. Chapter 5 describes the thermal analysis model developed in this study to estimate the thermal history of the deposited workpiece. The effectiveness of the model for designing a deposition strategy that prevents softening owing to thermal effects is demonstrated by experiments using high-speed steel. Chapter 6 provides a case study that shows a practical example of the high hardness material cladding fabricated by DED. Finally, the conclusions of the study are outlined in Chapter 7.

2 Demands and Issues in DED

2.1 Introduction

This chapter explains the objective and approach of this study and summarizes the current demands and issues in DED. The organization of this chapter is as follows. Section 2.2 provides an overview of hybrid DED, which combines DED with subtractive machining, and describes its advantages and applications in industrial fields. Section 2.3 provides the specific application that this study focuses on, that is, the cladding of high hardness material, and describes the requirements and challenges by referring to previous studies. Section 2.4 describes the objective and approach of this study toward these challenges. Finally, the conclusions of this chapter are outlined in Section 2.5.

2.2 Hybrid DED

As mentioned in Chapter 1, DED can be used to perform part restoration and function addition. In addition, the development of hybrid DED technology has enabled a single machine to complete these applications, which were previously performed off-site or by an external company using multiple machines.

One practical application of DED is in the mold repair process, as shown in Fig. 2.1 [23]. The damaged part of the mold requiring repair is identified and removed by subtractive machining. The hard material is then deposited by DED, and the mold repair is completed by finishing with subtractive machining. Figure 2.2 shows a comparison between the conventional repairing process and that using hybrid DED. As shown in Fig. 2.2, hybrid DED can decrease the setup times and reduce the processing time by almost half. Thus, manufacturing productivity can be dramatically increased. Moreover, the following advantages are also highlighted: Historically, large amounts of energy have been used to repair parts that were either discarded or remanufactured in conventional processes. As a result, cracks or defects were often found in the repaired part after subtractive machining, resulting in the part needing to be repaired again. In contrast, hybrid DED machines eliminate the need for rework and reduce the man-hours required. Furthermore, instability caused by manual work is eliminated, and the entire process can be performed by a single chucking operation. The hybrid DED-repaired molds last three times longer than that of conventionally manually repaired molds. In the past, many mold parts were discarded or repaired by hand or robot welding. Thus, in addition to reusing discarded parts, restoration machining using hybrid DED machines is expected to save a great deal of energy.

1. Die condition before repair
2. Target areas for repair
3. Machined die before deposition
4. Repair in-process
5. Repaired die

Fig. 2.1 Mold restoration process using a hybrid DED machine.

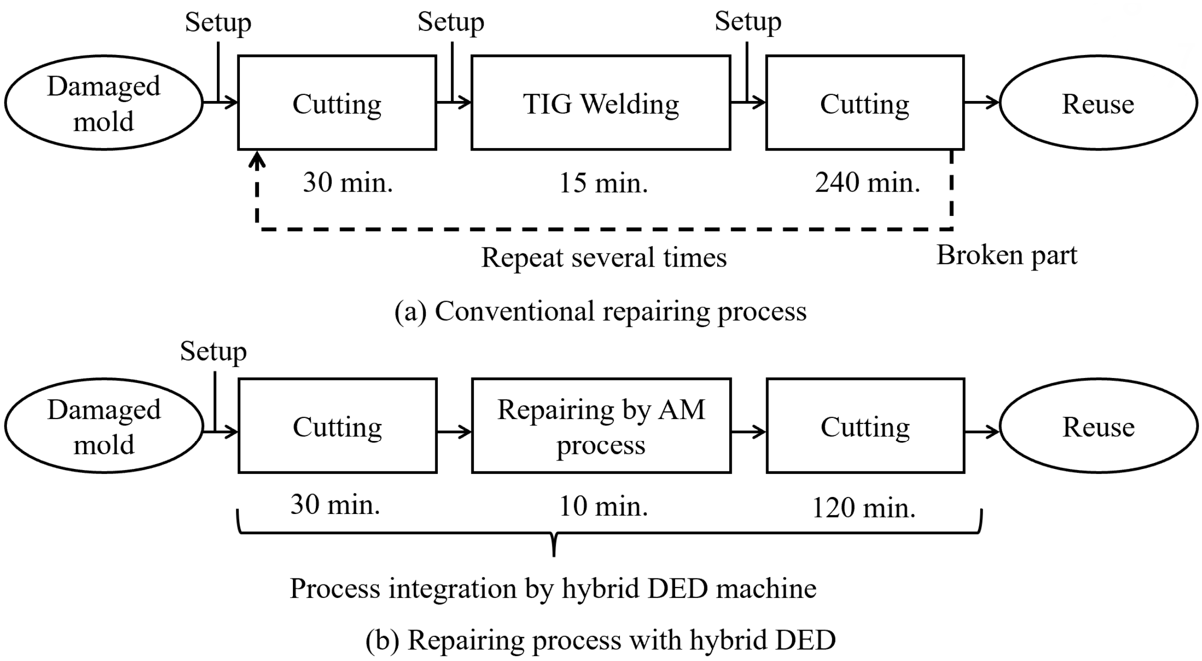

Fig. 2.2 Comparison between conventional and hybrid DED repairing process.

A consensus has been reached among users that the adoption of hybrid DED reduced manufacturing costs, waste production, and energy consumption, i.e., CO_2 emissions, achieving the social goal of Carbon neutrality and the circular economy [24].

Here, another DED application, bimetallic deposition, is introduced. The DED method allows a combination of dissimilar metals, and bimetallic deposition sometimes deposits stainless steel on the outside of a part and a copper alloy on the inside. By layering stainless steel with high heat and corrosion resistance on the outside of a part and a copper alloy with high thermal conductivity on the inside, the functionality and value of heat exchangers can be improved. For example, Fig. 2.3 shows images of the process for producing a bimetallic heat exchanger workpiece. The introduction of a hybrid machine with a 5-axis controlled vertical machining center allows the same machine to perform both deposition and machining using DED, enabling the production of this type of part in a single production step. Applied cases of this approach can be found across oil and gas, offshore, and space industries.

Therefore, the practical application of the DED hybrid process is the focus of this study, with the objective of providing a guideline for the successful operation of DED.

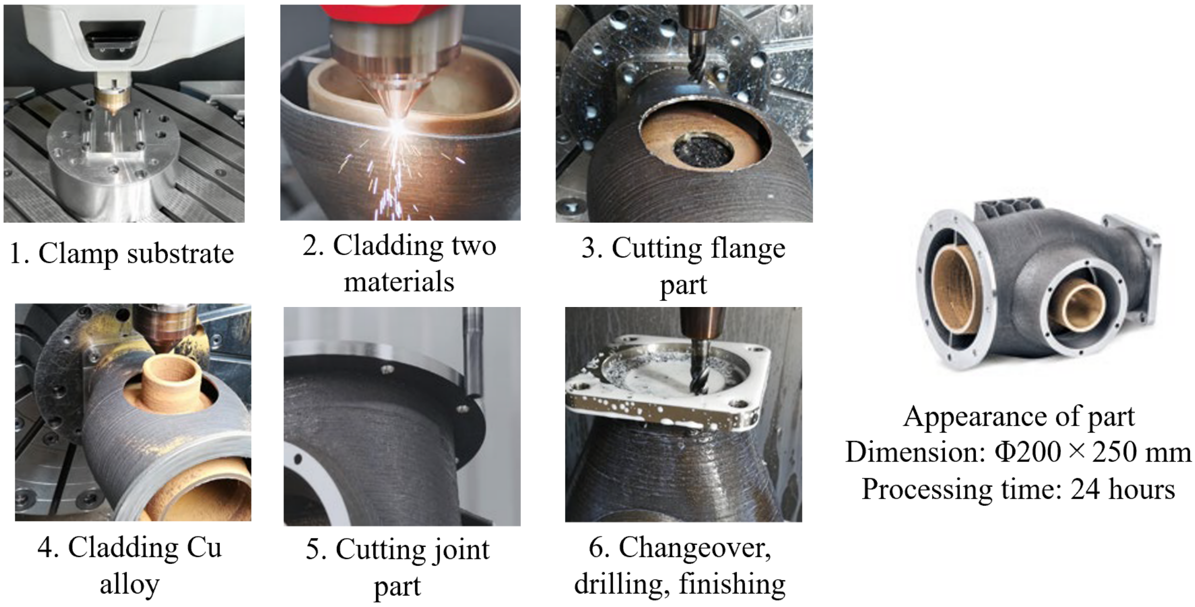

Fig. 2.3 Fabrication of a bimetal heat exchanger using a hybrid DED machine.

2.3 Targeted DED Application and Challenges

2.3.1 Targeted DED Application

This study focuses on high hardness material cladding. Figure 2.4 shows an example of an actual application of the additive–subtractive hybrid process wherein a die cut roll is produced. In this application, a hybrid DED machine is utilized to clad high hardness, corrosion-resistant materials on specific regions of the part. In the conventional process, the raw material is a corrosion-resistant material (Fig. 2.4(a)) that is machined by a subtractive process to the required shape. Thereafter, the portion of the part requiring high hardness is coated with hard chrome-plating (Fig. 2.4(b)). By contrast, when using a hybrid DED machine, an inexpensive material can be used as the raw material (Fig. 2.4(a’)). After machining the material to the required shape, high-hardness and corrosion-resistant materials are cladded onto the specified regions by DED (Fig. 2.4(b’)). This hybrid process contributes to sustainable manufacturing because hard chrome-plating can be replaced by this process, thus reducing manufacturing costs. The recent demand for carbon neutrality and circular economy also supports such processes.

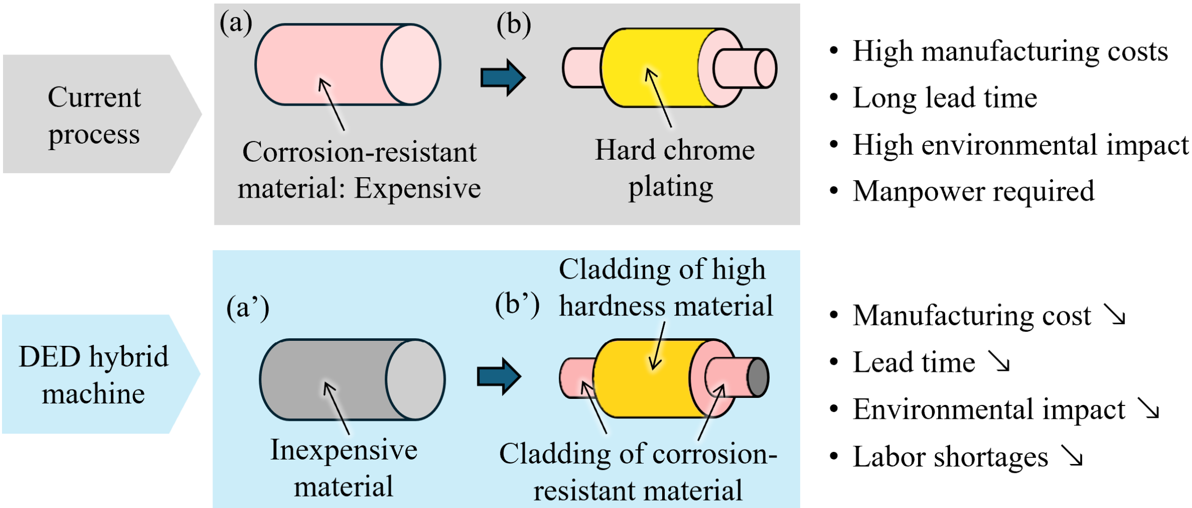

Fig. 2.4 Comparison of the conventional process with the innovative process using hybrid DED in the production of a die cut roll part.

2.3.2 DED Process

Figure 2.5 shows the DED process with a metal power, which is the focus of this study. A base material or deposited workpiece is irradiated with the laser beam to form the local heating area, referred to as the melt pool. Metal powder transported by carrier gas moves through the laser nozzle and is fed into the melt pool. The deposited material is shielded by a shielding gas to prevent the powder from entering the nozzle and protect the laser optical lenses from powder contamination. An inert gas is generally used to locally purge the atmosphere from the melt pool area and prevent oxidization. The laser nozzle is moved to deposit the material in specified geometries. Thus, the DED process includes melting and solidification cycles, and temperature changes occur not only in the melting and solidifying regions but also at specific points far from these regions. Therefore, deposited workpieces have a complex temperature history.

Here, terms related to deposition conditions that are controllable in the DED process are defined in Table 2.1. Note that the energy density, E [J/mm^2], is expressed as in Eq. (2.1).

$$E = \frac{60P}{F \cdot D}, \tag{2.1}$$

where P is the laser power [W], F is the nozzle feed rate [mm/min], and D is the laser spot diameter [mm]. When the energy density is changed, the degree of melting of the powder and substrate changes. If the energy density is not appropriate, the powder does not melt sufficiently, resulting in voids, as shown in Fig. 2.6. These multiple interdependent conditions complicate the DED process.

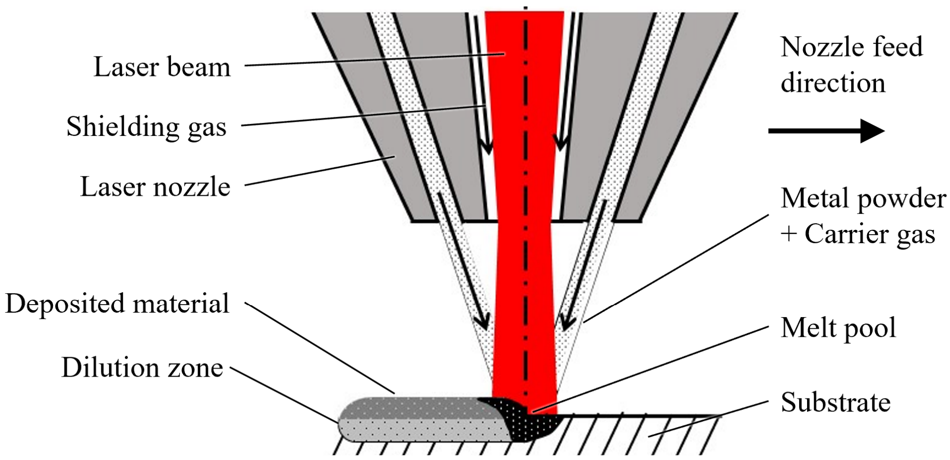

Fig. 2.5 DED process with a metal powder.

Table 2.1 Terms related to deposition conditions.

Term	Unit	Definition and description
Laser power	[W]	Amount of energy supplied per unit time Energy density per unit area changes
Powder feed rate	[g/min]	Amount of powder fed per unit time Amount of energy fed to the object to be deposited changes
Nozzle feed rate	[mm/min]	Speed at which the nozzle is scanned Energy density changes
Dwell time	[s]	Time interval between the current and next deposition Temperature of the object to be deposited changes
Preheating	[°C]	Temperature input to object before deposition Temperature of the object changes
Deposition path	[-]	Line spacing and nozzle feed direction Temperature of the object to be deposited varies

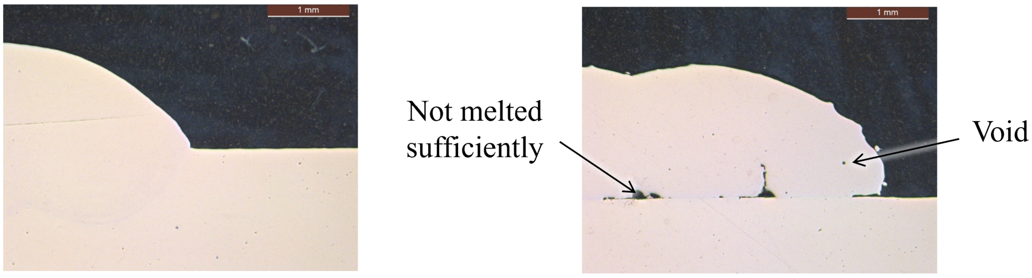

(a) Deposited with appropriate energy density (b) Deposited with inappropriate energy density

Fig. 2.6 Cross-section of the beads deposited with appropriate and inappropriate energy densities.

The terms related to the change in temperature and the control thereof for obtaining the desired deposition are defined in Table 2.2. Among them, the cooling rate for solidification and thermal history are illustrated in Fig. 2.7. Figure 2.7(a) shows a thin-wall-shaped workpiece deposited by DED. Figure 2.7(b) shows the temperature distribution of the deposited workpiece and its surroundings, obtained using a thermal camera. The thermal camera measured the temperature distribution during the deposition process. Figure 2.7(c) shows the temperature change over time at a specific point, recorded after initial solidification of the deposited powder at the specific point until the deposition process was finished. This temperature change over a comparatively long span of time is defined as thermal history. Figure 2.7(d) shows a magnified view of the temperature change shown in Fig. 2.7(c). As shown in Fig. 2.7(d), the temperature change per unit time during solidification is defined as the cooling rate for solidification, which is a temperature change on the microscale, in contrast to thermal history, which is temperature change on the macroscale.

Once the type and required specifications of the deposited material have been determined, the deposition conditions are determined according to the following steps.

i. What type of structure and composition does the deposited material require to meet the desired specifications? For example, a martensitic structure is required to obtain high hardness.
ii. What physical field history should be specified to obtain the required structure and composition? For example, the deposition temperature is maintained above the martensitic transformation point during the entire deposition process and then immediately cooled.

iii. How can the specified physical field history be realized? For example, deposition is performed in succession.

iv. Determine the set of specific conditions for realizing the specified deposition conditions.

Accordingly, (i) is defined as the material strategy, and (ii) through (iv) are included in this study as the deposition strategy.

Table 2.2 Terms related to deposition conditions.

Term	Definition and description
Cooling rate for solidification	Temperature change per unit time during solidification in the region of melting and solidification = Temperature change on the microscale
Thermal history	Temperature change over a long span of time after the first solidification = Temperature change on the microscale
Material strategy	Deposited material structure and composition required to obtain the desired specifications
Deposition strategy	Deposition conditions, cooling rate, and thermal history considered to obtain the desired structure and composition

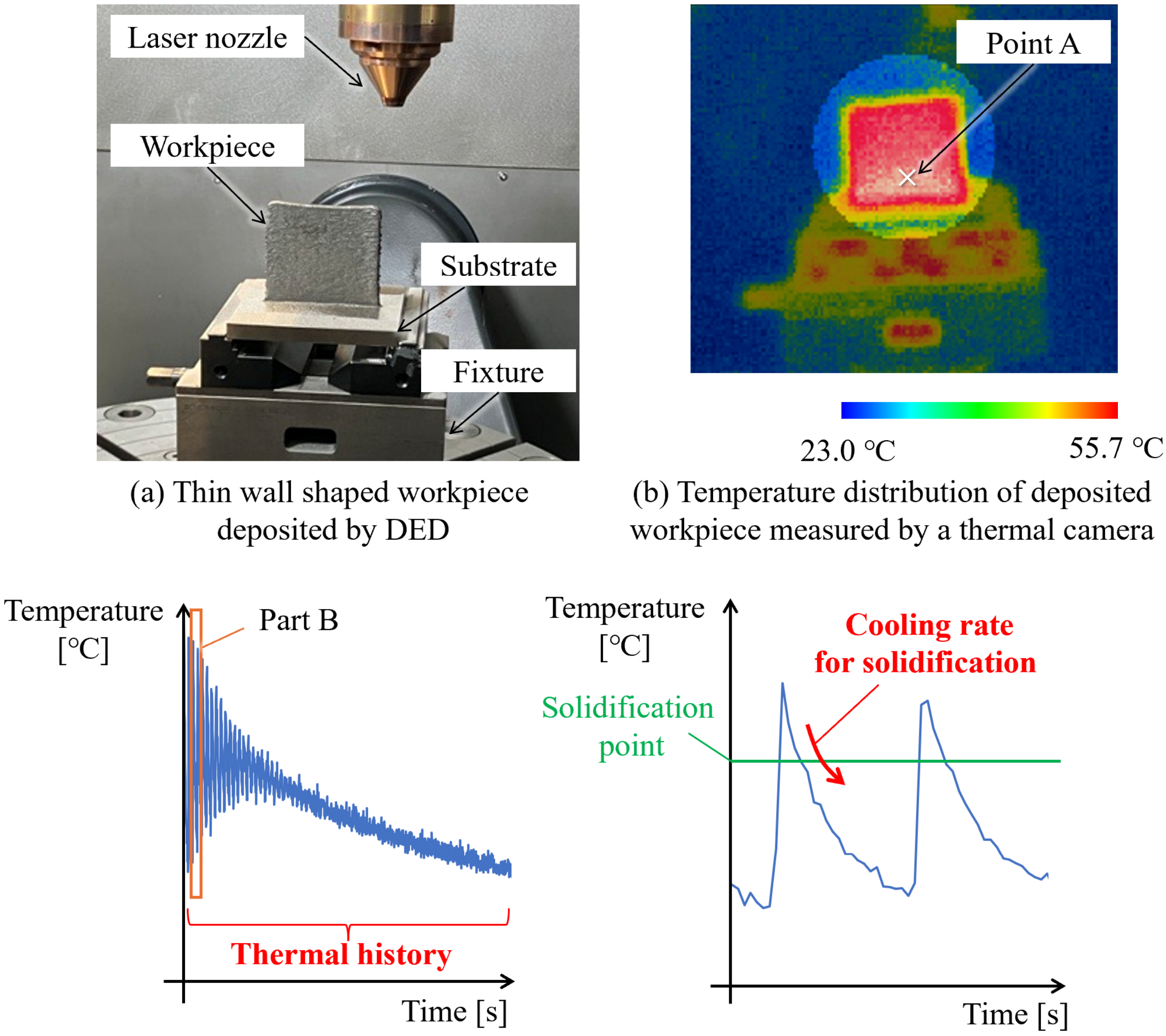

(a) Thin wall shaped workpiece deposited by DED

(b) Temperature distribution of deposited workpiece measured by a thermal camera

(c) Temperature change during deposition process at Point A

(d) Magnified view of Part B

Fig. 2.7 Cooling rate and thermal history indicated in terms of temperature change at a specific point during the deposition of the thin-wall-shaped workpiece.

2.3.3 Factors Contributing to Hardness and Cracking

For hard facing applications, the simultaneous maintaining of hardness and prevention of cracking is paramount [13], [14], [15]. Figure 2.8 shows the factors influencing the hardness and crack development generally considered. As shown in Fig. 2.8, hardness and crack development can be attributed to metallurgical and thermo-mechanical phenomena. From the viewpoint of metallurgical phenomena, the hardness of deposited parts is known to be affected by grain size, microstructure, and carbide precipitation. Crack occurrence in turn is influenced by the strength or toughness of the material and thermal stress. The precipitation of brittle materials such as carbide decreases the toughness of the material, and large temperature gradients owing to rapid heating and cooling during the process increase the thermal stress. Furthermore, these influential factors change as the thermal history and cooling rate change. In other words, the deposition strategy is important for achieving hard, crack-free deposition.

However, determining the optimal deposition conditions is challenging owing to the DED process, which involves complex melting and solidification cycles induced by thermal energy. Therefore, various studies have been conducted on the factors that contribute to the hardness and crack development of deposited parts.

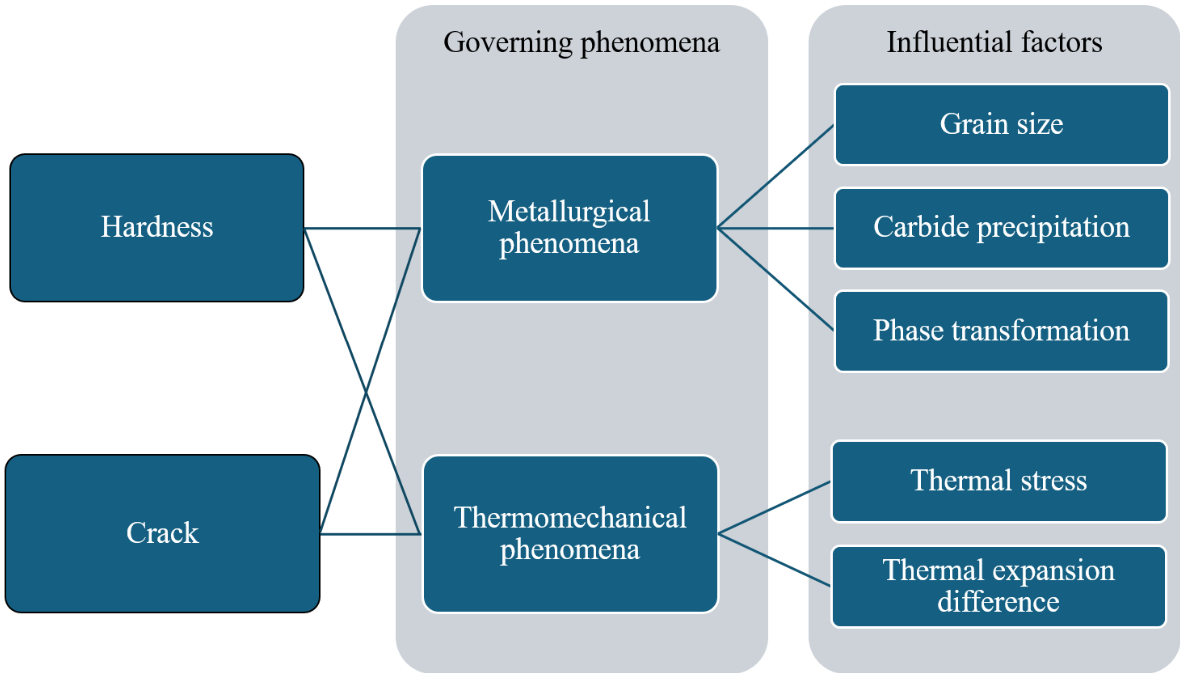

Fig. 2.8 Factors and physical phenomenon influencing hardness and cracking.

Zuback and DebRoy reviewed studies investigating the relationship between the cooling rate and hardness of deposited parts [25]. They pointed out that, in general, as the heat input increases, the cooling rate reduces owing to heat accumulation, resulting in an increase in grain size and coarsening of the microstructure, which in turn reduces the hardness. In other words, a decrease in grain size correlates with an increase in hardness of the deposited part.

Furthermore, Li et al. conducted a microstructural analysis on parts deposited by electron beam melting [26]. They pointed out that higher cooling rates with reduced line energy resulted in finer crystal grains and precipitated carbides, which led to improved micro-hardness.

To prevent crack development, many researchers have used various approaches in an attempt to suppress or prevent cracking of the deposited material, substrate material, or between the materials. Preheating is one of the major countermeasures used for suppressing crack development [27] because it decreases the cooling rate that results in the smaller residual thermal stress. Zhou et al. showed that the temperature gradient in the deposited material could be decreased by increasing the average preheating temperature [28]. However, the high preheating temperature led to increased dilution of the substrate and deposited materials, which can decrease the hardness of the deposited material near the substrate [29], [30]. Typical preheating has been conducted by scanning the laser beam before the deposition process [21], [27]. Induction heaters have also been used because of their high efficiency, fast heating, safety, cleanness, and accurate controllability [31], [32].

2.3.4 High-Speed Steel and Stellite Cladding

As discussed in Chapter 1, high-speed steel and Stellite, which are used in the majority of the hard facing, are targeted in this study. For the cladding of these materials, although experimental research for determining the deposition conditions has been conducted thus far, knowledge necessary to select a deposition strategy is lacking.

Locs et al. conducted an experimental study on the DED deposition of the high-speed steel, M2, and demonstrated a hardness of HRC 63 for coating application [33]. Rahman et al. produced a high-speed steel alloy by laser cladding and highlighted the occurrence of cracks in the case of multiple-layered cladding [34]. Although cracking was suppressed by preheating at 150 ± 10 ℃, the hardness of the intermediate layers decreased owing to tempering by re-heating. Although the reduction in hardness was overcome by the addition of Co, this countermeasure is restricted to certain applications. Another approach for preventing hardness reduction resulting from tempering was proposed by Fukuyama et al. [35]. They introduced additional laser heating processing to maintain the deposited workpiece temperature above the martensitic transformation temperature throughout deposition. However, whether or not the actual temperature exceeded the martensitic transformation temperature was not evaluated.

Costa et al. simulated the thermal history of the workpiece through the single line wall deposition of material SUS420, which is not a high-speed steel but a martensitic material [36]. They reported that the temperature was maintained above the martensitic transformation temperature throughout deposition without an interpass dwell time between the layers and that martensitization occurred only during cooling after deposition, resulting in hardening. They also indicated that to avoid temper softening, the workpiece temperature during deposition should not be decreased to levels where a martensitic phase change can occur. In other words, martensitic structure is also a factor influencing hardness. Although their simulation results suggested an effective strategy for achieving high hardness and material strength, experimental validation was not conducted. In addition, the scalability of this approach is limited because the simulation carries a high computational cost owing to the consideration and calculation of temperature and phase transition dependencies.

A few studies have investigated the deposition strategy for Stellite. The effect of preheating on Co-based superalloys was investigated by Alimardani et al. and Fallah et al., but the preheating process was conducted by scanning the laser beam across the top surface of the substrate [27], [22]. Moreover, the surface hardness has been confirmed to decrease by preheating in deposited Co-based superalloys. The maximum decrease found was 10 HRC (171 HV) [22]. Co-based superalloys are beneficial for hard facing applications; thus, a solution for this hardness decrease must be found.

2.3.5 Techniques for Controlling Thermal History in DED

As described in the previous subsections, thermal history is known to have a significant effect on the quality of deposition, such as hardness and cracking. The temperature range and time within a certain temperature range in the thermal history are crucial because they significantly influence the microstructure evolution. For high hardness steels, the melting, austenitizing, and martensitic phase change temperatures are important. The temperature history of DED is complex because the cyclic heating and cooling periodically include remelting and solidification processes. In this subsection, existing techniques for controlling the thermal history of DED are reviewed.

Farshidianfar et al. investigate controlling the grain size and hardness of a deposited material by measuring the cooling rate in real time and controlling the nozzle feed rate at a target value in a closed loop [37], [38]. In their study, an infrared camera was mounted off-axis to the nozzle to measure the temperature of the melt pool and its surroundings. The cooling rate was calculated by dividing the temperature change at the point of interest by the interval between consecutive images. Although closed-loop control of the cooling rate improved the uniformity of the microstructure and hardness in thin-wall deposition, deviations remained owing to post-solidification heating cycles of the subsequent layers. In other words, not only the temperature at the time of deposition but also the temperature history of the heat-affected zone during deposition of the subsequent layers influenced the final hardness. In their study, the cooling rate was controlled by adjusting the nozzle feed rate.

In addition to changing the nozzle feed rate, the cooling rate has been controlled by changing the deposition parameters, such as laser power and powder feed rate [39], [40]. However, controlling the geometry by changing the deposition conditions is considered difficult because the deposition width or height can change.

Alternatively, to change the cooling rate, Kim et al., Ren et al., and Sefidi et al. investigated the effect of changing the deposition path strategy on the thermal history [41], [42], [43], and Yokota et al. used forced cooling [44]. Moreover, Costa et al. proposed changing the dimensions of the base material [36]. However, the effects were limited by the workpiece geometry.

Controlling the cooling rate by adjusting the interpass dwell time, which is a resting time interval between the deposition of layers, is considered a practical solution.

Guévenouxa et al. investigated the effect of the interpass dwell time between layers on the microstructure of thin-wall deposition using Inconel 718 and confirmed by electron back scattered diffraction (EBSD) analysis that the grain size decreased with dwell time [45]. Furthermore, they suggested that specific micro-structural gradients at the interface between the original and repaired deposited parts could be controlled by controlling the dwell time. However, their study only compared the presence and absence of dwell time, and the effect of dwell time length itself was not investigated and the cooling rate was not measured. Finally, the mechanism of the effect of dwell time on microstructure has not yet been elucidated.

2.4 Research Objective and Approach

Based on the background described in Section 2.3, the research objective of this study is to solve the following challenges.

1) When the cooling rate and thermal history are changed in consideration of practical process constraints, it is effective to use the dwell time. However, the range of the cooling rate and thermal history change with the dwell time required is not clear.
2) The exploration of deposition conditions for Stellite is insufficient. The mechanism of reduction of the hardness with preheating has not been clarified.
3) The relationship between hardness / cracking and cooling rate / thermal history is not fully elucidated. Although simulation is effective for elucidating these relationships and devising deposition strategies, the simulation reported in a previous study carries a high computational cost.

Approaches to solve the above three challenges and achieve the research objective are described in Chapters 3,4, and 5, respectively.

In Chapter 3: The cooling rate was measured by changing the dwell time, and the effect of the cooling rate on the hardness of the deposited part was investigated. Therein, grain size was considered a factor affecting hardness. To exclude the effects of phase transformation and carbides, SUS316L is used as the deposition material because the austenite in SUS316L is in a (quasi-)stable phase at both high and low temperatures, thus preventing martensitic transformation even when the material is rapidly cooled, as in the case of DED. The temperature distribution of the melt pool was measured, and the cooling rate was calculated from the time variation of the temperature distribution. To measure the temperature distribution in the melt pool, a DED system was developed in which an infrared camera is installed coaxially with the laser for deposition. The difference in this system from those of previous studies is that the cooling rate can be measured without being affected by the scanning direction of the laser, and the installation of a camera coaxially to the laser is advantageous. Furthermore, using a thermal camera, the surface temperature of the workpiece during deposition was measured, and the effects of the dwell time on it were investigated.

In Chapter 4: Two types of deposition experiments were conducted to experimentally investigate the deposition conditions for cladding Co-based superalloys by DED while preventing cracking and reduced hardness. In one experiment, the preheating temperature was changed with the laser power constant. In the other experiment, the laser power was changed with the preheating temperate contact. The material of interest was Stellite 1, a Co-based superalloy widely used in die-cut rolls and screw shafts. Stellite has high wear resistance and is suitable for parts requiring excellent resistance to various forms of wear and high strength over a wide temperature range [31]. An efficient induction heating apparatus was employed in these experiments. Because only the induction target specimen was heated, heat loss owing to surrounding elements was minimized and high temperatures could be reached [46]. An induction heater was used for preheating, and the effect of relatively high preheating temperatures (400 to 600 ℃) compared to those of previous studies was investigated. A compositional analysis was conducted on the deposited workpiece to investigate the factors causing cracking and hardness changes.

In Chapter 5: The effect of thermal history on workpiece hardness and cracking in the cladding of M2, a high-speed steel, was investigated through a combination of numerical analyses and experimental techniques. To obtain numerical results in a practical time period, a simplified temperature simulation model was employed that ignored nonlinear phenomena such as phase transformation. Whether or not the model could be used to determine a deposition strategy that does not reduce hardness was verified.

2.5 Summary of Chapter 2

In this chapter, AM and DED are described holistically from the viewpoint of their history, market, and applications. Furthermore, the challenges associated with the practical application of these technologies in industrial fields are addressed by referring to past research. Finally, the objectives of this study are declared. The contents are summarized as follows.

1) The application of DED technology for high hardness coating in industrial fields is in high demand, not only to reduce manufacturing costs but also to reduce environmental impacts.

2) For practical application, maintaining high hardness without cracking is a challenge. Various studies have been conducted, highlighting the importance of the cooling rate and thermal history during the deposition process.

3) This study focuses on high-speed steel and Stellite, and the objective is to elucidate the influence of the cooling rate and thermal history on hardness and mechanical cracking through a combination of numerical and experimental techniques.

3 Effect of Cooling Rate on Hardness

3.1 Introduction

One of the most promising AM technologies is DED, which excels at partial coating and repairing with both standard and dissimilar metal depositing. However, determining the optimal deposition parameters to obtain the desired shapes and mechanical properties is difficult because of the complex process of melting and solidification cycles by thermal energy. Although some studies have focused on the cooling rate as a temperature change factor and investigated its relationship with mechanical properties, they have not evaluated the range within which the cooling rate changes.

In this chapter, a range of cooling rates and their influence on hardness in DED were investigated under practical conditions using the austenitic stainless steel, SUS316L. The goal was to control the hardness of the deposited part by adjusting the cooling rate. Among the factors contributing to the hardness of the deposited part, grain size is particularly affected by cooling rates. Hence, this study focused on grain size to evaluate the effect of DED technology. Herein, a method is proposed for calculating the cooling rate based on the temperature distribution in the melt pool, captured by a camera placed coaxially to the laser beam. The interpass dwell time, which is a resting time interval between the deposition of layers, was varied, and the effects thereof on the cooling rate and hardness were investigated. Furthermore, the surface temperature of the workpiece during deposition was measured with a thermal camera.

The organization of this chapter is as follows. Section 3.2 provides the experimental setup and method. Section 3.3 describes the results. Section 3.4 discusses the obtained results. Finally, the conclusions of this chapter are outlined in Section 3.5.

3.2 Experimental Setup and Method

3.2.1 Experimental Setup and Materials

The purpose of the experiment was to investigate the range of cooling rates in DED deposition, how the hardness and crystalline structure change within that range, and the relationship between them. Figure 3.1 shows a schematic of the experimental setup used in this study. As shown in the figure, a thin-wall shape was deposited on the base metal. The laser used was a diode laser with a wavelength of 1020 nm and a spot size of 3.0 mm. The metal powder is fed into the melt pool formed on the base material by the laser through a nozzle and melted for deposition. To prevent oxidation at the deposition point, argon gas was supplied from the center of the nozzle to form a protective area around the melt pool.

The metal powder used was SUS316L, an austenitic stainless steel. The grain size ranged from 53 to 150 μm, and the powder was gas-atomized. Because the material did not undergo martensitic transformation, the hardness was strongly dependent on the grain size, and the cooling rate during solidification was considered important. The surface of the base material, carbon steel JIS S50C, was face-milled to a roughness of Ra 6 μm and clamped to the machine table by a centering clamping device.

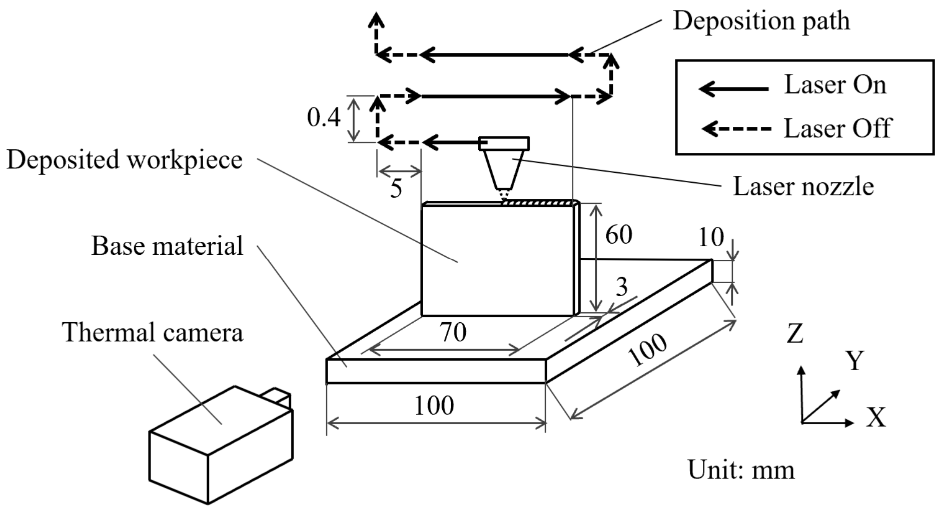

Fig. 3.1 Schematic of the measuring temperature setup and deposited layer size.

A zigzag path was used for deposition, in which the direction of deposition changed for each layer. To avoid the effect of acceleration/deceleration of the nozzle feed, the nozzle was moved without laser irradiation for 5 mm before and after deposition. To change the cooling rate, the interpass dwell time was varied during the deposition process. Table 3.1 lists the deposition conditions.

The surface temperature of the workpiece during deposition was measured using a thermal camera. The maximum measurement temperature of the thermal camera used was 900 ℃, and the measurement wavelength ranged from 8 to 14 μm.

Table 3.1 Deposition conditions.

Workpiece No.	W1	W2	W3	W4	W5	W6
Laser power [W]	1800					
Feed rate [mm/min]	1000					
Powder feed [g/min]	12					
Carrier gas flow [L/min]	6					
Shielding-gas flow rate [L/min]	5					
Layer height [mm]	0.4					
Interpass dwell time [s]	0	3	6	9	12	24

3.2.2 Calculation Method

The cooling rate was calculated from the temperature distributions measured in and around the melt pool. Figure 3.2 shows a schematic of the measurement system. A charge-couple device (CCD) camera was installed coaxially with the laser, and measurements were taken directly from an angle above the melt pool. In addition, a filter that only allowed light with a wavelength of 740 nm to penetrate was installed in front of the coaxial camera. This measurement system has the same configuration as that used by Kledwig et al. [47]. For the conversion of light intensity captured by the coaxial camera into temperature, Planck's law was applied, as expressed by Eq. (3.1) [48].

$$L(\lambda, T) = 2C_1/[\lambda^5 \cdot \{\exp(C_2/\lambda T) - 1\}], \tag{3.1}$$

where $L(\lambda, T)$ [W·sr^{-1}·m^{-3}] is the spectral radiance value from the object, λ [m] is the wavelength of radiation emitted from the object, T [K] is the absolute temperature of the object, C_1 [W·m^2] is the first constant of radiation (= c^2h = 5.9548×10^{-17}), C_2 [m·K] is the second constant of radiation (= ch/k = 0.014388), c is the speed of light in vacuum (= 2.99792458×10^{-8} [m·s^{-1}]), h [J·s] is Planck's constant (= 6.6256×10^{-34}), and h is Boltzmann's constant (= 1.38054×10^{-23} [J·K^{-1}]). Using Eq. (3.1), a λ of 740 nm and estimated temperature range of 900 to 2000 ℃ are applied to obtain the conversion curve shown in Fig. 3.3, assuming that the spectral radiances at 900 and 2000 ℃ are equivalent to the minimum (= 0 digit) and maximum (= 4096 digits) values in the grayscale of the CCD camera, respectively. Using this conversion curve, any radiance value between 0 and 4096 digits is converted to temperature. It should be noted that Planck’s law holds for black bodies, with an emissivity of 1. In actual measurement objects, emissivity varies with temperature. Therefore, the measurement method using this conversion curve may have measurement errors. However, the application of this temperature measurement method using only one wavelength was shown in a previous study to have relatively small errors [47].

The method used to calculate the cooling rate is described below. Figure 3.4 shows an example of the temperature distribution measured by the camera. In the first image, the average temperature is taken at the center of the image perpendicular to the nozzle feed direction. In the second image, the average temperature is taken at a position Δd from the center because the point at the center of the first image has moved to a distant position based on the product of the nozzle feed rate and the camera’s frame capture interval.

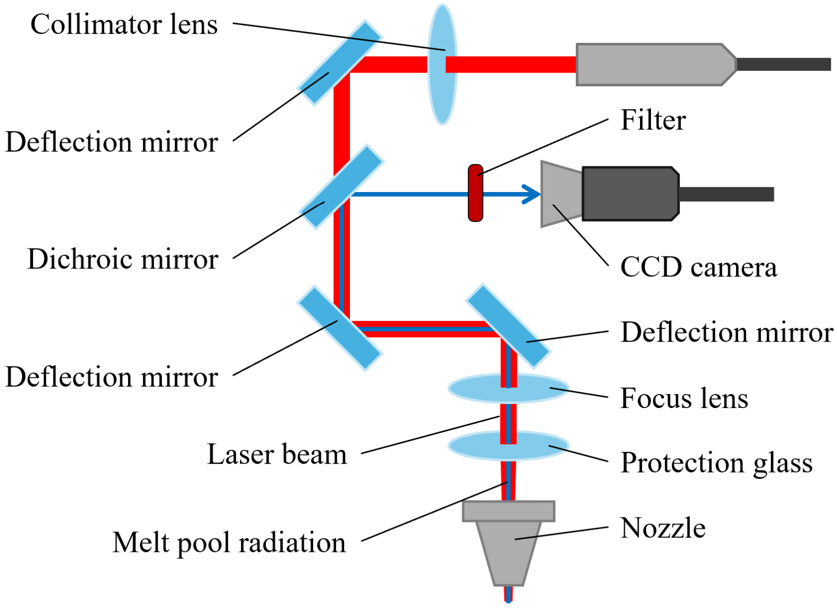

Fig. 3.2 Measurement of melt pool temperature distribution with CCD camera mounted along with the laser beam axis.

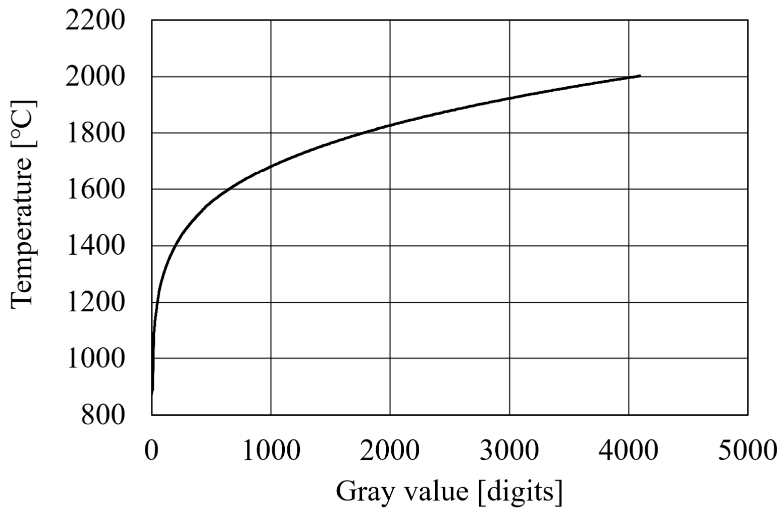

Fig. 3.3 Light intensity and temperature conversion curve.

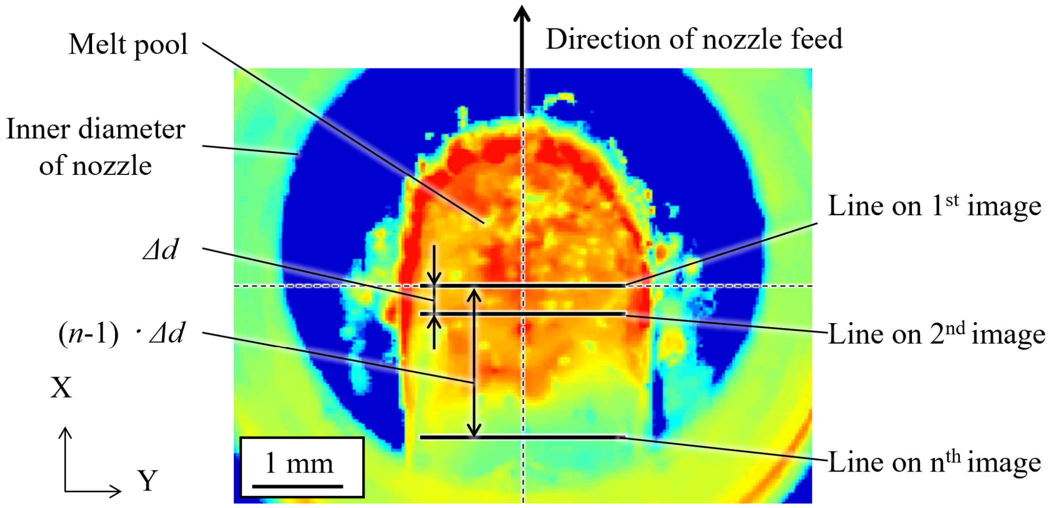

Fig. 3.4 Temperature evaluation lines and melt pool displacement per one frame delta d on a melt pool image (length of the lines is 2.2 mm).

In this way, the average temperature at the line can be calculated for all successive *n* images. In this study, the images were taken at 200 Hz, and the nozzle feed rate was 1,000 mm/min; thus, Δd was 0.083 mm. The line length was 2.2 mm, and the average temperature was calculated from 24 consecutive images. Figure 3.5 shows one example of the calculated average temperature using this method. In Fig. 3.5, the average temperature approximated by a quadratic function and function slope of 1400 ℃, that is, the solidification temperature of SUS316L, was calculated to be the cooling rate. Furthermore, the approximation obtained by using a quadratic function shows high fitness with a coefficient of determination (R^2) of 0.99. It should be noted that there were other cases in which the average temperature was obtained only above 1400 ℃. In such cases, extrapolation was performed with a quadratic function to estimate the change below 1400 ℃ and calculate the cooling rate. In these cases, the R^2 exceeds 0.9. Furthermore, Fig. 3.6 shows other cases in which the average temperature was obtained below 1000 ℃. As shown in Fig. 3.6, a gradual decrease in temperature over time is observed from approximately 1000 ℃. This trend is observed for all dwell time conditions at a deposition height of 0.4 mm. These data are approximated by a quadratic function to approximate temperature changes below 1000 ℃. Furthermore, the R^2 is 0.99, indicating a high degree of fit. The cooling rate for the data measured above 1200 ℃ in Fig. 3.6 was also approximated by a quadratic function, and no significant difference from the cooling rate approximated by a quadratic function was observed. This can suggest that it is reasonable to extrapolate or approximate the temperature variation up to approximately 1400 ℃ with a quadratic function. The cooling rate was calculated at three locations in the same deposition layer, and the average was used as the cooling rate for that layer.

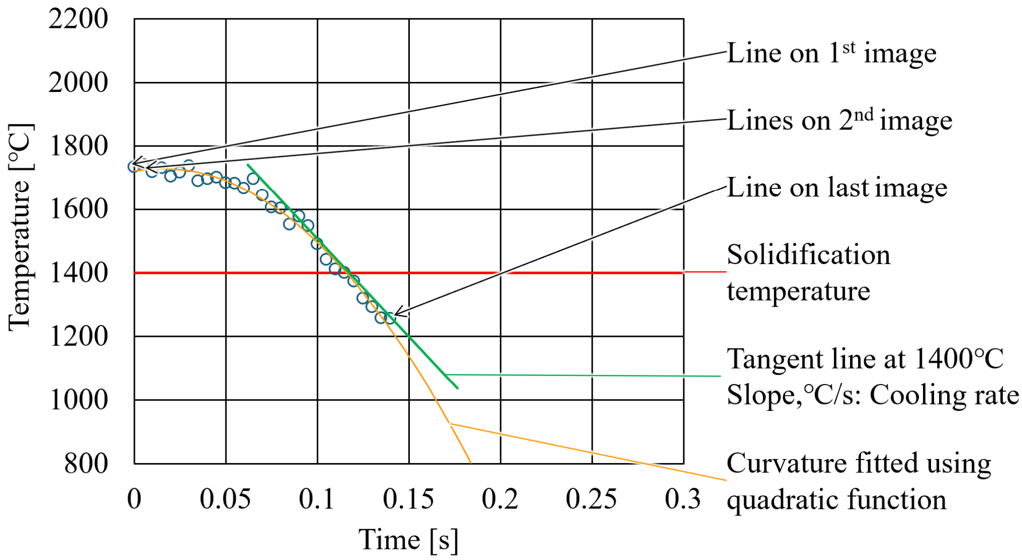

Fig. 3.5 Calculation results of the average temperature and estimation of the cooling rate for a dwell time of 12 s and deposition height of 10 mm.

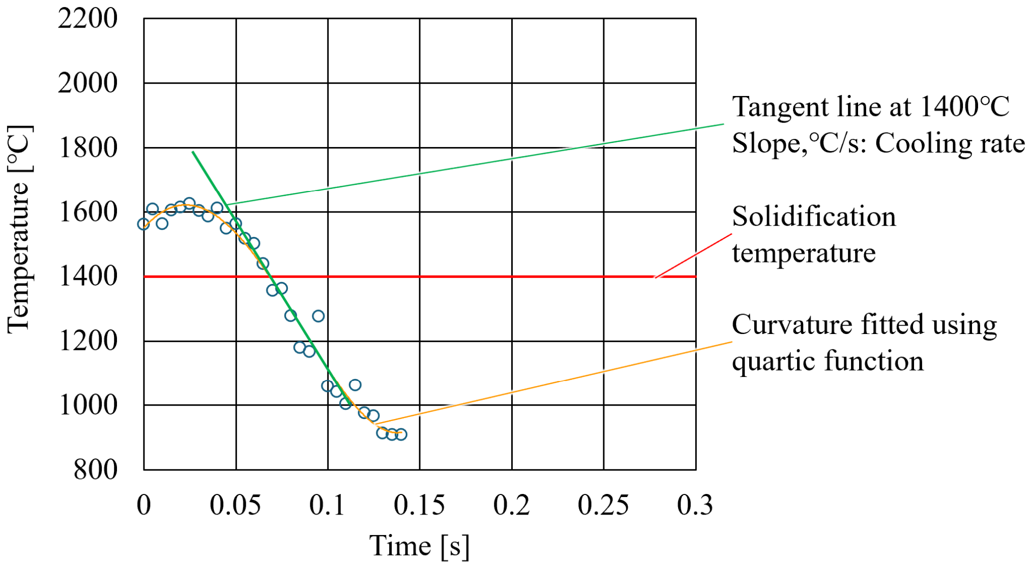

Fig. 3.6 Calculation results of the average temperature and estimation of the cooling rate for a dwell time of 9 s and deposition height of 0.4 mm.

3.2.3 Evaluation Method

As shown in Fig. 3.7(a), the deposited specimens were cut at three positions to measure the hardness. A wire electrical discharge machining (EDM) was used to cut the specimens, and the cross-sections were polished for measurement. As shown in Fig. 3.7(b), the hardness was measured at the center of the cross-section of the deposited part, with the surface of the base material used as the reference height (0 mm). Figure 3.7(c) shows the heights of the measurement points. The measurement interval near the base material–cladding interface was shorter than that in other regions because the change in hardness in that region was larger. The measurements were taken at three cross-sections to obtain an average value for the hardness at each height. Notably, because the deposited shapes differ from one other, the measurement intervals in region A differ at cutting positions I and III of workpiece W1, the cutting position II of workpiece W1, and those of the other workpieces, as shown in Fig. 3.7(c). As described in Subsection 3.3.1, the workpiece W1 had a lower height than the other workpieces and a concave shape at cutting position II.

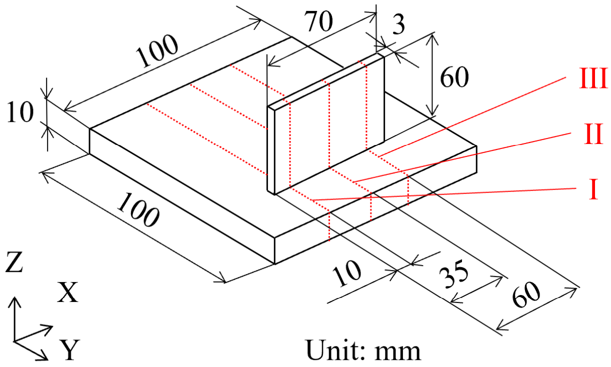

(a) Workpiece and cutting positions, I, II and III

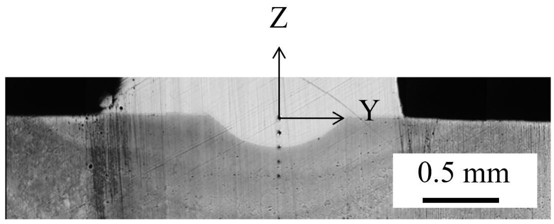

(b) Interface of base material and cladding part

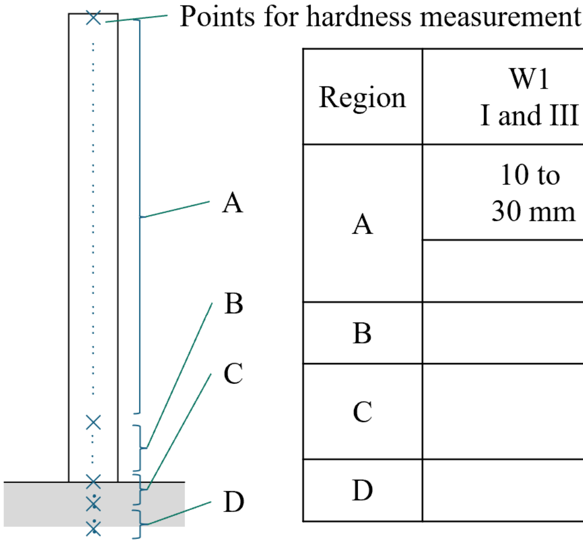

Region	W1 I and III	W1 II	W2 to W6 I to III
A	10 to 30 mm	10 to 20 mm	10 to 60 mm
	10 mm increments		
B	0.4, 1, 2, 3, 5 mm		
C	-0.4 to 0 mm 0.1 mm increments		
D	-1.2, -0.7 mm		

(c) Cross-section of workpiece and heights of points for hardness measurement for each workpiece

Fig. 3.7 Hardness measurement schematic.

The measuring instrument used was the micro-Vickers hardness tester (HMV-G-FA-D, Shimadzu Corporation, Japan). After ion milling the cross-section, the crystal structure was observed using EBSD to evaluate the grain size and phase. A compositional analysis was also performed using energy dispersive X-ray spectroscopy (EDX).

3.3 Investigation

3.3.1 Deposition Results

Figure 3.8 shows an overview of the deposited specimens. As shown in Fig. 3.8(a), the specimen deposited without dwell time has a concave shape in the center, and the deposition height is lower than the target deposition height. By contrast, as shown in Fig. 3.8(b), the specimen deposited with a dwell time of 6 s has a uniform rectangular shape, and the target deposition height is achieved.

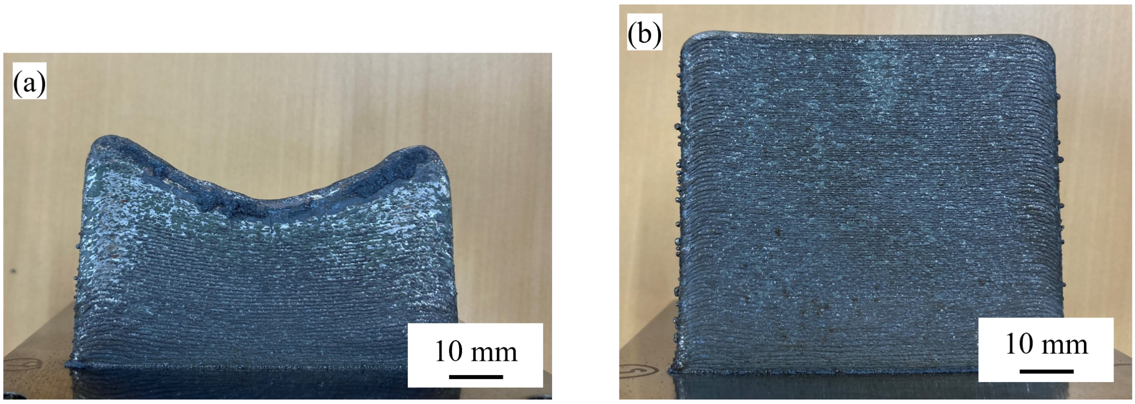

Fig. 3.8 Overview of samples deposited with interpass dwell times of (a) 0 and (b) 6 s.

3.3.2 Calculation Results

Cooling rates were calculated at heights of 0.4, 2, 10, 20, 30, and 40 mm from the base material. The calculated cooling rates are shown in Fig. 3.9. For each dwell time, the cooling rate is highest at a height of 0.4 mm, which is near the interface. In addition, the cooling rate decreases as the height further increases to 2 and 10 mm. To investigate the effect of dwell time on the cooling rate at various heights from the base material, the relationship between the dwell time and cooling rate was evaluated, as shown in Fig. 3.10. In Fig. 3.10(a), the cooling rate tends to decrease slightly as the dwell time increases for a height of 0.4 mm. The cooling rate decreased by approximately 27% from a dwell time of 0 to 12 s. Figure 3.10(b) shows that the cooling rate also tends to slightly decrease as the dwell time increases at a height of 2 mm, with a decrease of approximately 14%. In contrast, Fig. 3.10(c) shows that at a height of 10 mm, the cooling rate is less affected by the dwell time and tends to remain constant. Although longer dwell times are expected to result in cooler temperatures for deposited parts and faster cooling rates for the subsequent deposition layer, the opposite trend is observed. This outcome is considered to be owing to the large effect that cooling by heat conduction has on the cold base material. However, at a height of 20 mm, the cooling rate tends to slow down as the dwell time becomes shorter, as shown in Fig. 3.10(d). As the height further increases, from 30 to 40 mm, the cooling rate increases for shorter dwell times, as shown in Fig. 3.10(e) to (f), respectively.

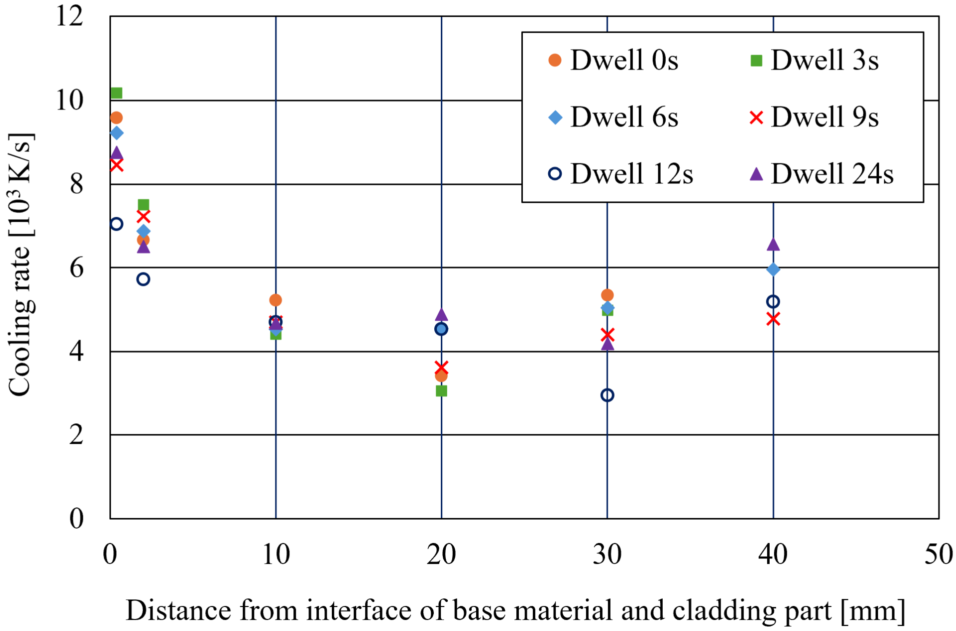

Fig. 3.9 Cooling rate for each deposition condition at each deposition height.

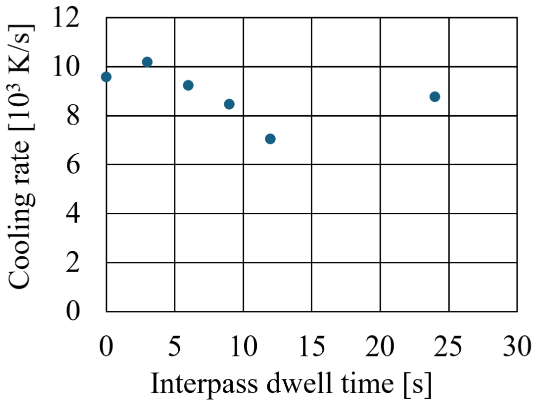

(a) Deposition height 0.4 mm

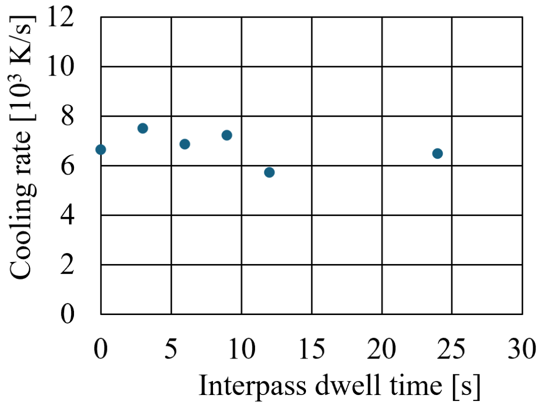

(b) Deposition height 2 mm

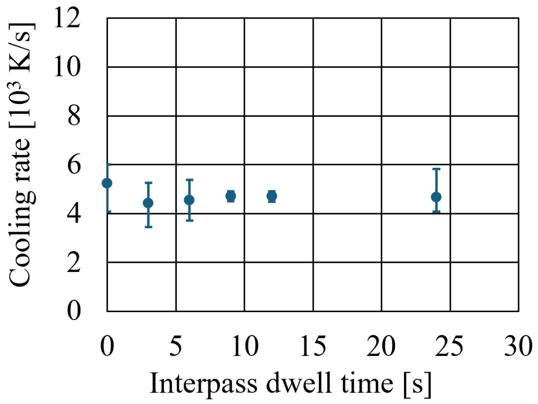

(c) Deposition height 10 mm

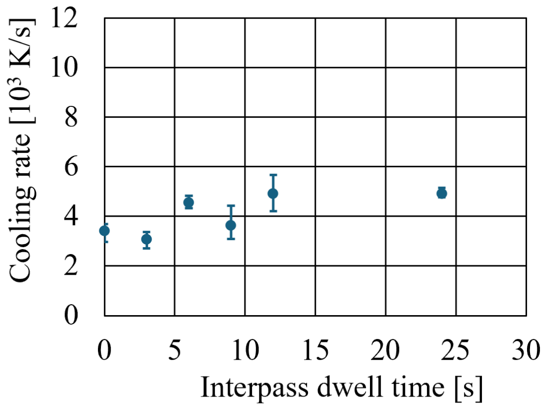

(d) Deposition height 20 mm

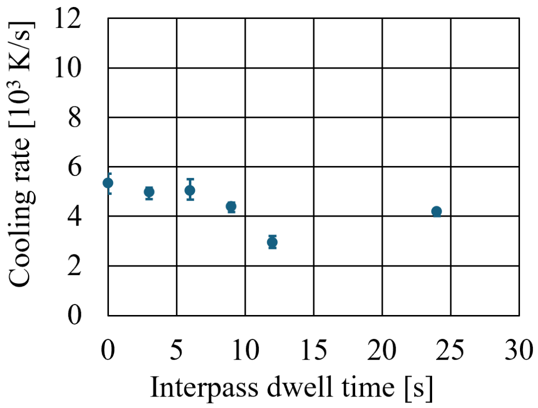

(e) Deposition height 30 mm

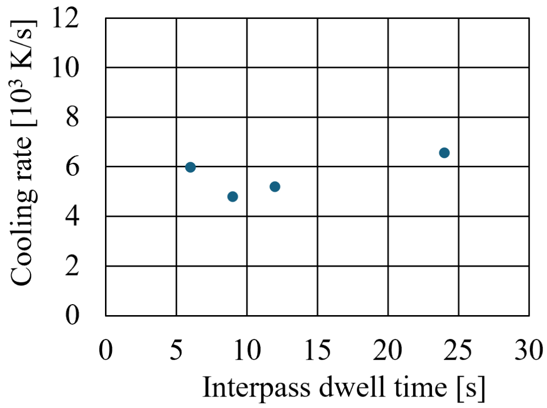

(f) Deposition height 40 mm

Fig. 3.10 Cooling rate for each interpass dwell time condition at each deposition height.

3.3.3 Measurement Results of Hardness

Figure 3.11 shows the measured hardness. As shown in the overall view in Fig. 3.11(a), for all specimens, the hardness is higher near the interface and on the base material side. In addition, the hardness gradually decreases from a height of 0 to 20 mm and tends to be almost constant when the height exceeds 20 mm. As shown in the magnified view in Fig. 3.11(b), the highest hardness is at a height of approximately -0.3 mm, presumed to be owing to the hardening of the base material. Furthermore, at heights of 0.4 to 2 mm, the hardness appears to decrease with increasing dwell time. At these heights, the cooling rate tends to decrease with dwell time, as shown in Fig. 3.10(a) and (b). One can infer that the cooling rate decreases with increasing dwell time, thereby increasing the grain size and decreasing the hardness. This suggests that, under the conditions used in this study, for thin-layer applications such as coatings, a shorter dwell time would result in higher hardness, which is preferable.

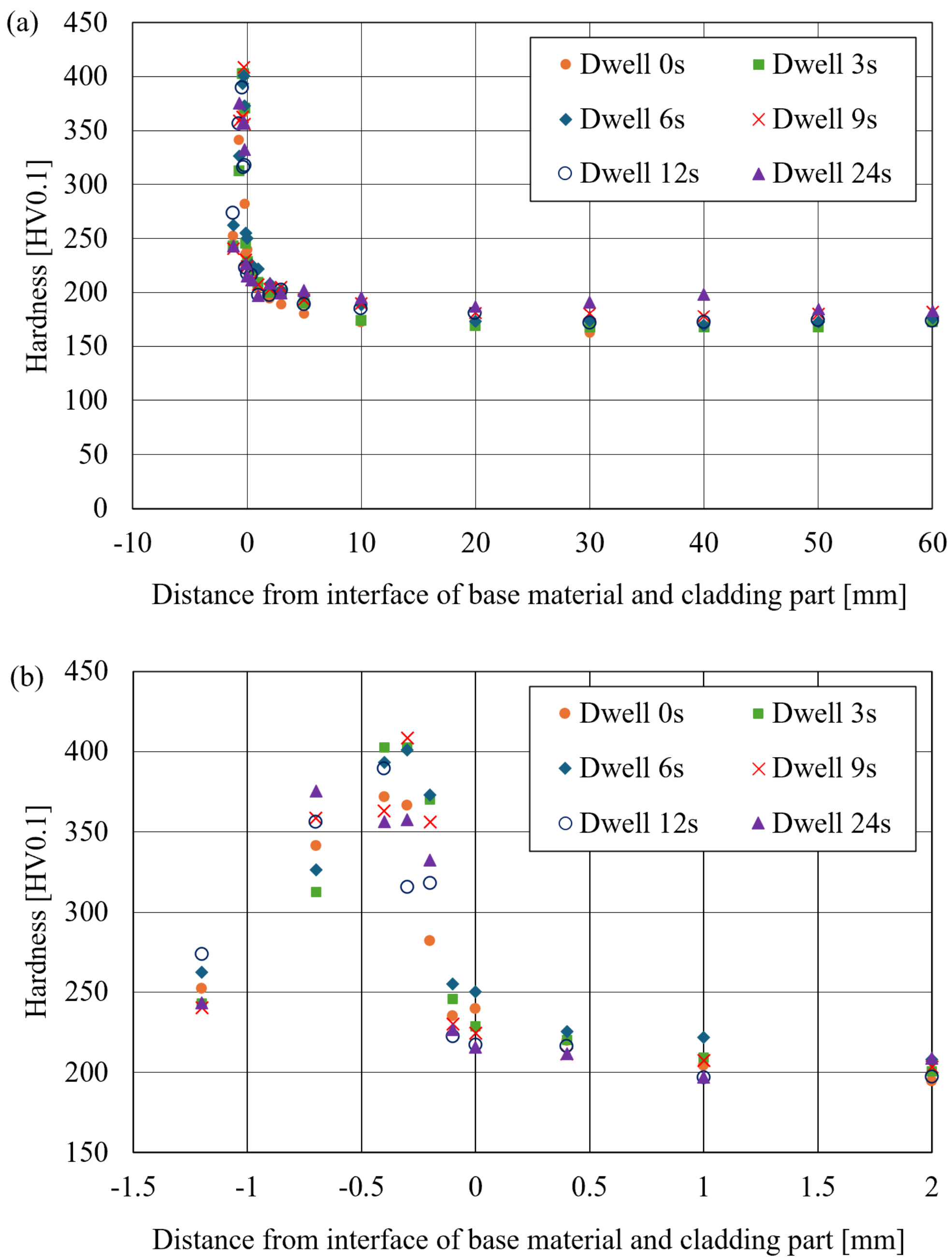

Fig. 3.11 (a) Measured hardness of each workpiece for the entire region and (b) magnification of the near interface between the base material and cladding.

3.3.4 Measurement Results of Workpiece Temperature

Figure 3.12 shows the history of the maximum workpiece temperature during deposition. The maximum workpiece temperature is the temperature of the pixel that exhibits the highest temperature in a thermal camera image. The temperature rises in the same manner regardless of dwell time up to a height of 3 to 4 mm. Thereafter, the temperature continues to increase up until a height of approximately 20 mm and then plateaus at a constant temperature as the increase in dwell time is shortened.

Figure 3.13 shows the measured temperature history at one specific pixel (2.1 mm square) located at a height of 18.8 mm from the base material surface. Starting from layer 47, the maximum temperature during the deposition of each subsequent layer was plotted. For the layer-by-layer deposition, the shorter the dwell time, the higher the temperature of that area.

The cooling rate during solidification or microscopic temperature change discussed in Subsection 3.3.2 tended to be significantly affected by the deposition height, whereas the effect of dwell time tends to be less significant in comparison. That being said, Figs. 3.12 and 3.13 show that the dwell time influences the maximum achievable and surface temperatures of the deposited part. In other words, dwell time affects macroscopic temperature changes, inferring that it has an effect on phase transformation.

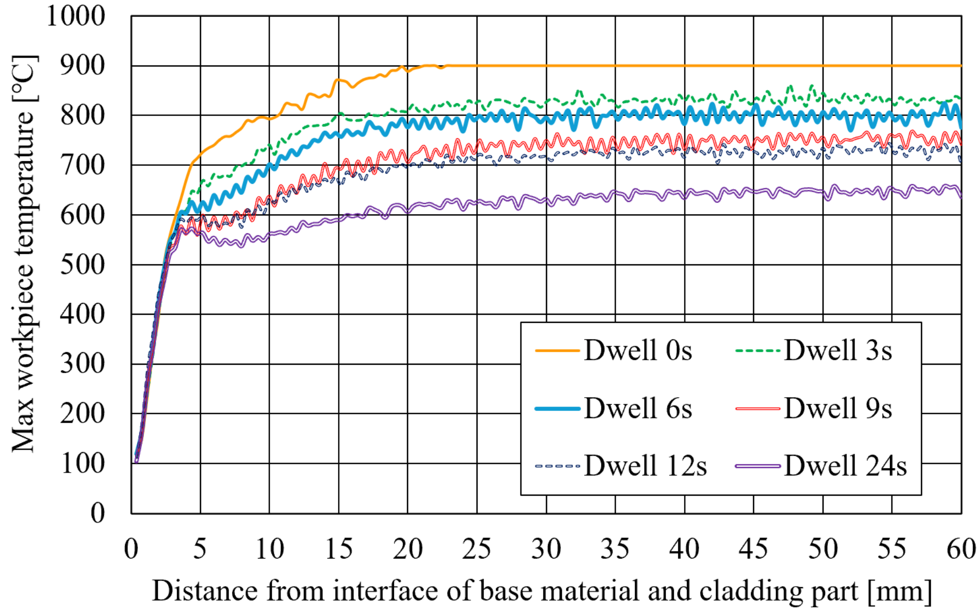

Fig. 3.12 History of maximum workpiece temperature for each dwell time condition.

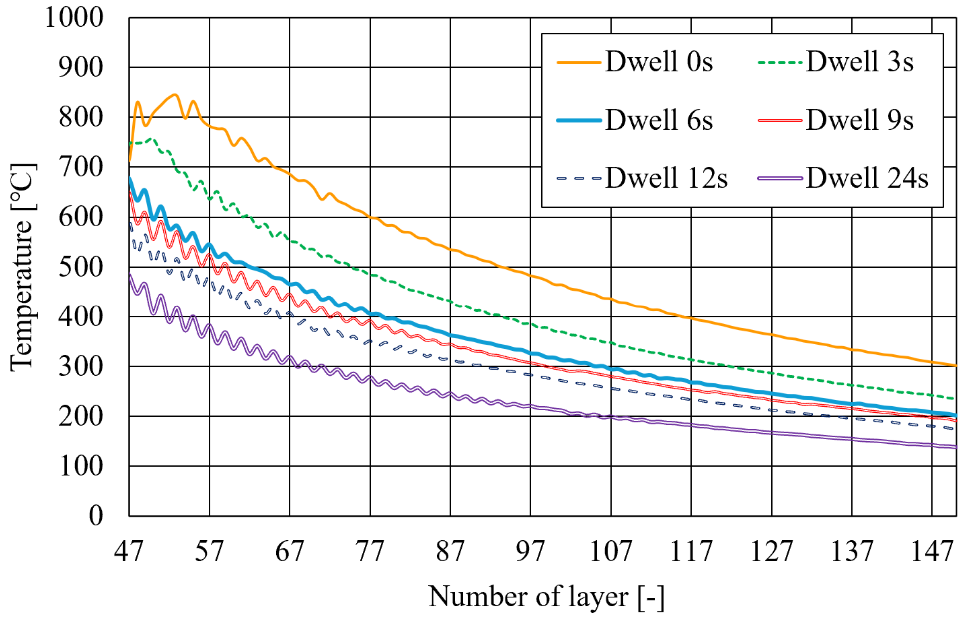

Fig. 3.13 History of workpiece temperature at a fixed point for each dwell time.

3.4 Discussion

3.4.1 Grain Size and Microstructure Near the Interface

As shown in Subsection 3.3.1, the decrease in hardness of the upper layers with and without dwell is considered to result from heat accumulation in the upper layers and the coarsening of the crystal grains in SUS316L. In contrast, a previous study showed that the upper layers become harder [36]. This inconsistency is considered to stem from the fact that the SUS420 used in the previous study was maintained at a temperature higher than the martensitic transformation temperature by heat accumulation, resulting in hardening by martensitic transformation during cooling with the occurrence of grain coarsening. In other words, heat accumulation is a softening factor for SUS316L and both a hardening and softening factor for SUS420, which may account for the difference between the previous study and this study in terms of hardness of the deposited part, apart from the diluted portions.

To verify that the workpieces in this study had different grain sizes and hardnesses, EBSD analysis was performed. Figure 3.14 shows the inverse pole figures obtained through EBSD. The inverse pole figures were obtained through the grain size evaluation method that uses the intercept method, which is standardized in JIS G0551 (2020) to evaluate the grain size [49]. The method is as follows. (1) The number of grains (N) captured by a test line of known length is measured on the microstructure image. (2) N is measured in five or more lines, and the average value of N is obtained. (3) The average value of N is divided by the length of the test line on the microstructure image to obtain "the mean number of grains intercepted per millimeter." The reciprocal of this value is "the mean lineal intercept length." (4) The grain size index is determined by comparing these values with the table "Number of grains as a function of various parameters" in JIS G0551 (2020), and the average grain size is obtained.

In this study, as shown in Fig. 3.15, the test lines were taken vertically and horizontally, and the average of five lines was taken as the average grain size. The length of the test line was set to 0.5 mm for the figure obtained at a height of 0 mm and 1 mm for those obtained at other heights. Figure 3.16 shows the grain size at each deposition height evaluated as described above. The figure shows that the grain size is reduced by the dwell time. In particular, a fine crystal structure can be observed near the interface with the base material. In addition, Fig. 3.17 shows the phase maps observed by EBSD. As shown in Fig. 3.17, the entire deposited part is face center cubic, and martensitization is unlikely to occur.

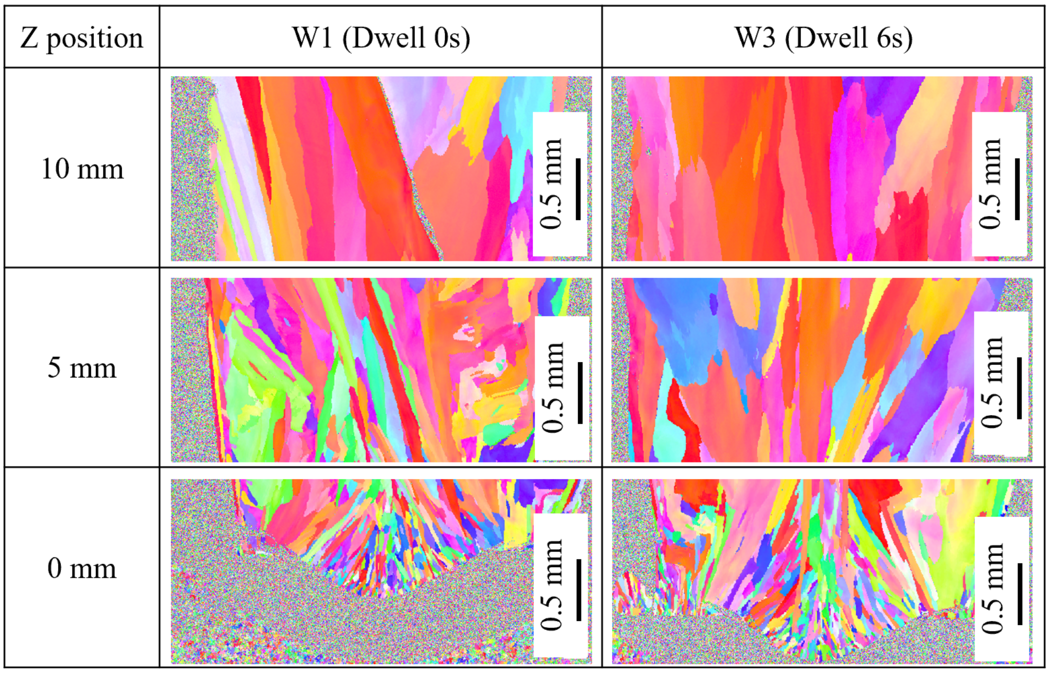

Fig. 3.14 Inverse pole figures observed with EBSD for workpieces W1 and W3.

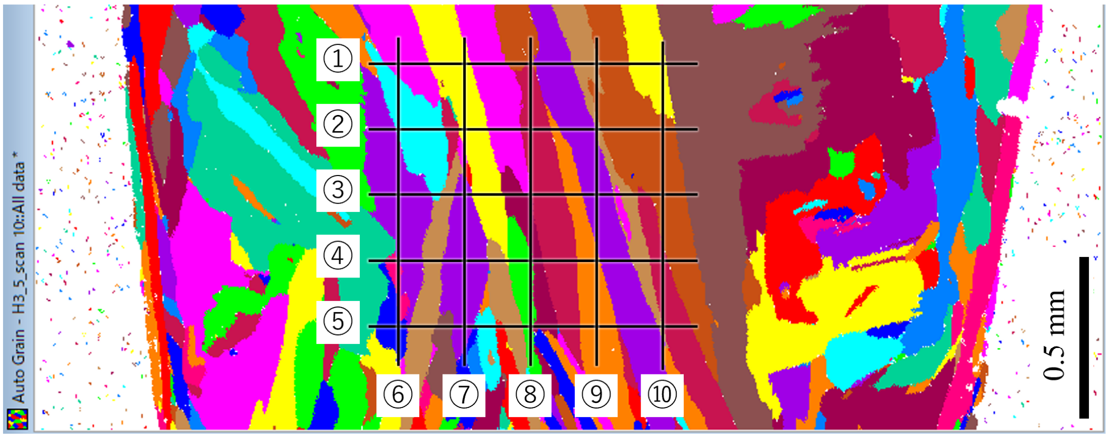

Line	①	②	③	④	⑤	Ave. (Horizontal)	Ave.
N	11	11	14	15	16	13.4	9
Line	⑥	⑦	⑧	⑨	⑩	Ave. (Vertical)	Ave. grain size
N	5	5	4	4	5	4.6	88 μm -125 μm

Fig. 3.15 Test lines on the inverse pole figure for evaluating grain size for W1, Z = 5 mm.

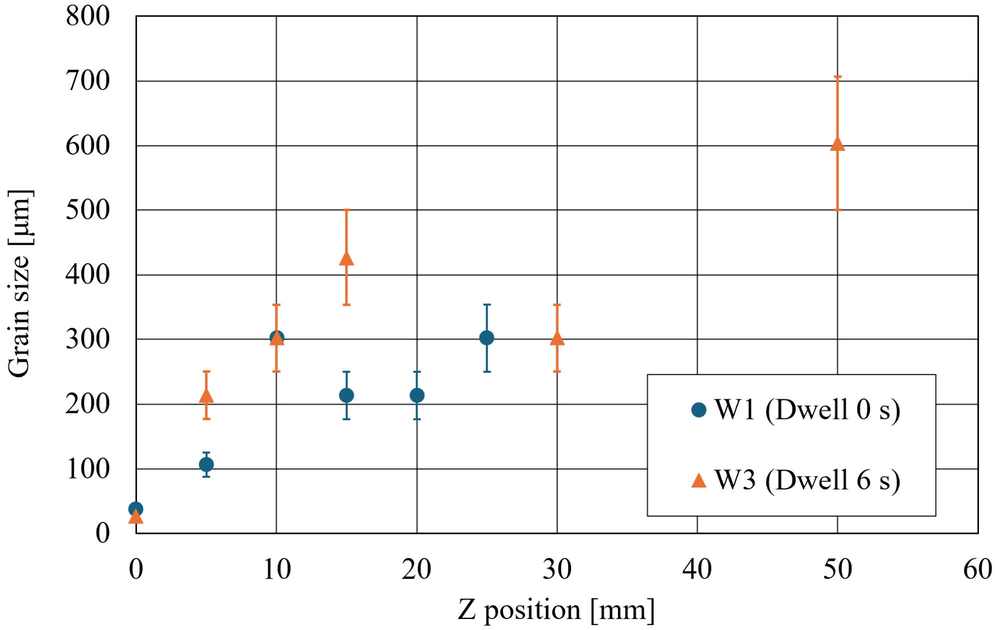

Fig. 3.16 Grain size at each deposition height for workpieces W1 and W3.

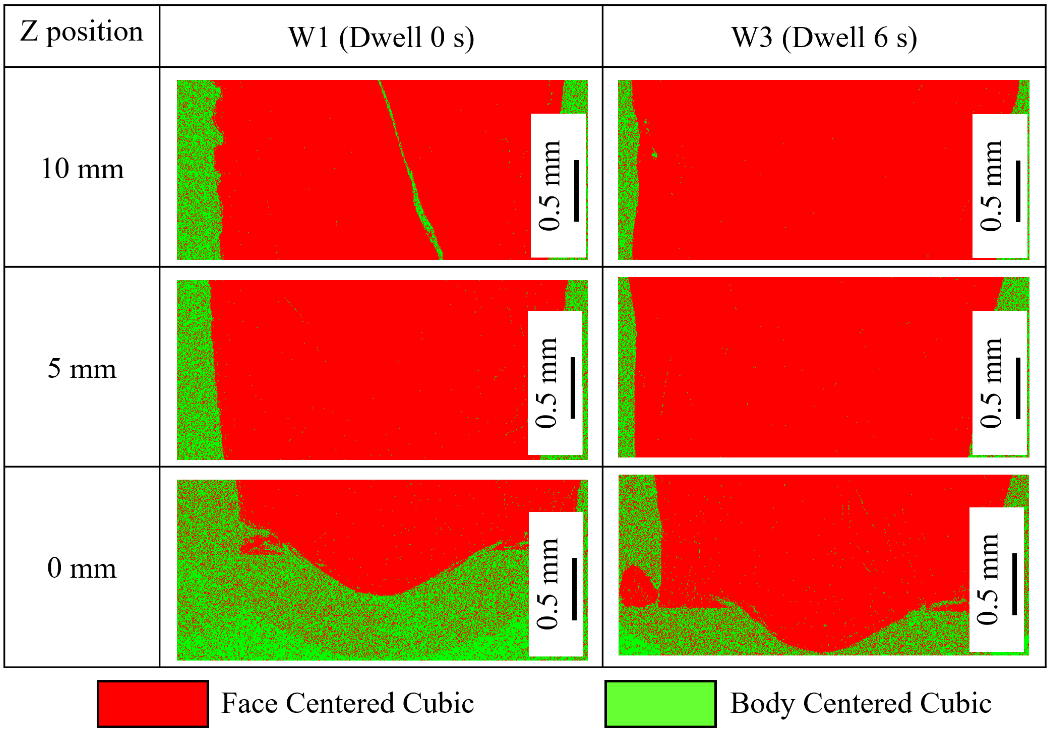

Fig. 3.17 Phase maps observed by EBSD for workpieces W1 and W3.

As shown in Fig. 3.11, the hardness fluctuates greatly near the interface between the base material and deposited part (height range from -0.1 to 0.4 mm). This is due to the effect of the cooling rate on the grain size. However, as shown in Fig. 3.7, the interface region is a dilution layer between the base material and deposited part, and this dilution of the base material may have an effect on the different hardnesses under each condition. To verify this assumption, an EDX analysis was performed. The results are shown in Fig. 3.18. The figure shows that there is no significant change in composition between W1 without dwell time and W3 with a dwell time of 6 s. This suggests that grain size is a strong contributor affecting the change in hardness at the interface. It should be noted that grains grow even around the recrystallization temperature, and grain growth is determined by the temperature and holding time. The recrystallization temperature of SUS316L ranges from 800 to 950 ℃ according to Hirota et al. and Zhao et al [50], [51]. As shown in Fig. 3.13, in this study, the temperature exceeding 800 ℃ when the dwell time is 0 s is held for approximately 50 s, corresponding to a deposition time for 10 layers. This holding time is relatively short for grains to adequately grow during recrystallization. Therefore, the effect of grain growth around the recrystallization temperature on the final grain size in the deposition experiments of this study is considered to be insignificant.

The hardness, phase composition, and grain size at each height are schematically shown in Fig. 3.19. The changes in these characteristics according to height are considered attributable to the effect of the cooling rate, which can be estimated by measuring the temperature distribution near the melt pool.

Z position	SEM, Maps (Fe, C) and Composition [wt %]

15 mm

W1

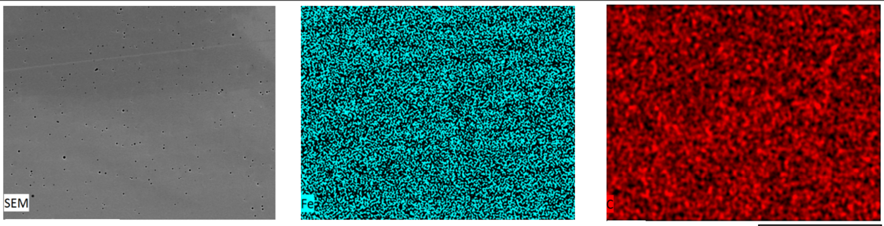

Fe	C	Cr	Ni	O	Si	S	Mo	P	Mn
76.0	3.2	12.1	6.7	0.4	0.8	0.7	0.0	0.0	0.0

W3

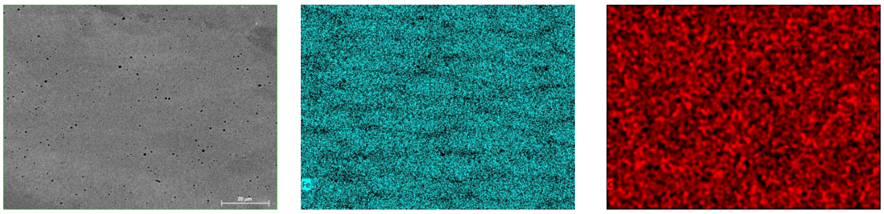

Fe	C	Cr	Ni	O	Si	S	Mo	P	Mn
76.6	3.1	12.1	6.3	0.5	0.8	0.7	0.1	0.0	0.0

0 mm

W1

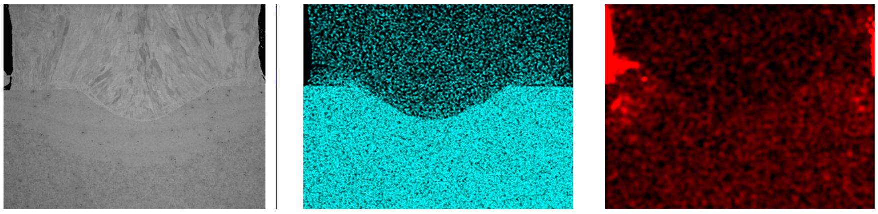

Fe	C	Cr	Ni	O	Si	S	Mo	P	Mn
89.5	4.6	4.7	0	0.3	0.6	0.31	0.0	0.0	0.0

W3

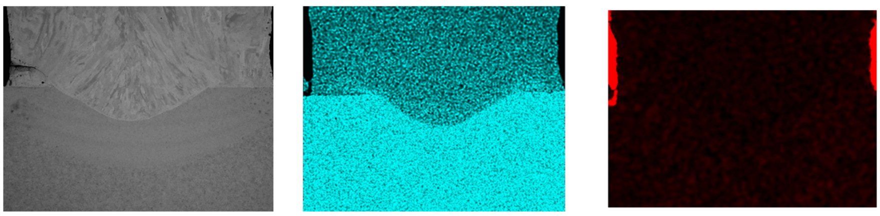

Fe	C	Cr	Ni	O	Si	S	Mo	P	Mn
88.8	5.9	4.1	0	0.4	0.6	0.3	0.0	0.0	0.0

Fig. 3.18 Composition analysis results for workpieces W1 and W3 obtained by EDX.

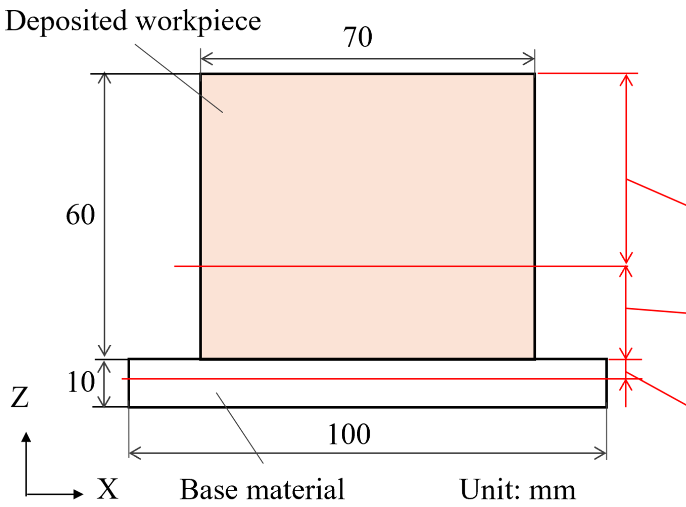

Z [mm]	Hardness [HV]	State
20 ~	160 ~ 180	Austenite + large grain
0 ~ 20	170 ↑ 250	Austenite + small grain
-0.5 ~ 0	~ 400	Hardened base material

Fig. 3.19 Schematic of the hardness, phase composition, and grain size changes as well as deposition height.

3.4.2 Relationship between Cooling Rate and Hardness

Figure 3.20 shows the relationship between the calculated cooling rate and hardness. The figure shows that the hardness varies between 160 and 220 HV under the deposition conditions used in this study. The cooling rate ranges from 3×10^3 to 10×10^3 K/s. The order of magnitude is 10^3 K/s, which is equivalent to that observed in previous studies [38], [52]. Moreover, a linear correlation exists between the cooling rate and hardness, both of which are affected by the deposition height.

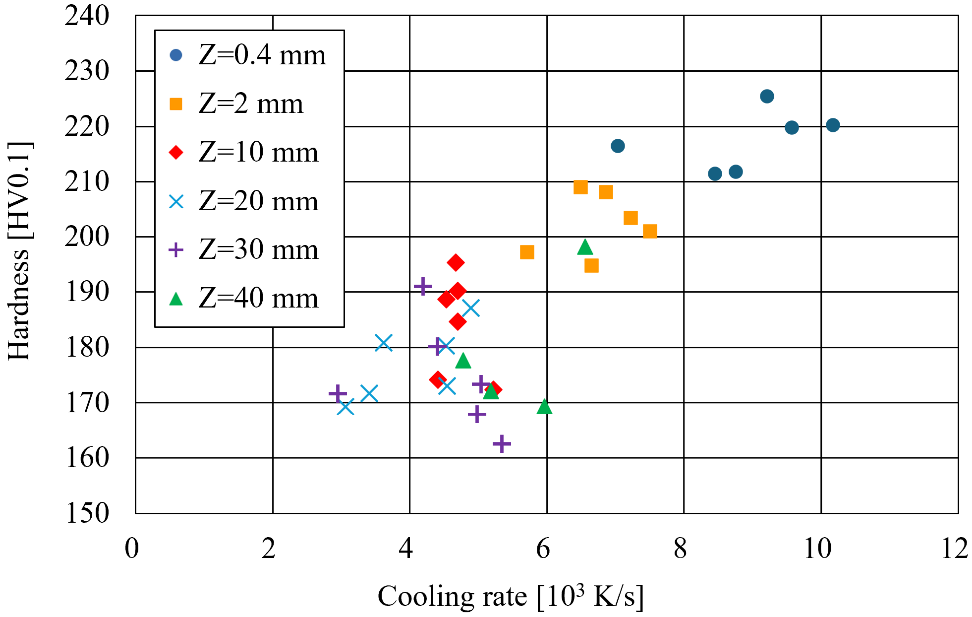

Fig. 3.20 Relationship between cooling rate and measured hardness.

3.5 Summary of Chapter 3

To investigate the effect of the cooling rate on the mechanical properties of DED, deposition tests were performed by varying the dwell time between the layers, and the relationship between the cooling rate, hardness, and crystalline structure of the specimens was evaluated. The following conclusions were obtained.

1) The calculated cooling rates were larger near the interface and lower for heights of 10 mm and higher. In contrast, the change owing to the dwell time at each height was small. Therefore, the microscopic cooling rate during solidification can be is not significantly affected by the dwell time but is affected by the deposition height.

2) The shorter the dwell time, the higher the surface temperature of the workpiece measured during deposition. Thus, the macroscopic temperature change affecting the crystal evolution and phase change was influenced by the dwell time.

3) Under the deposition conditions in this study, the cooling rate ranged from 3×10^3 to 10×10^3 K/s. The hardness ranged from 160 to 220 HV, and a correlation between the cooling rate and hardness was observed.

4 Influences of Substrate Preheating

4.1 Introduction

Chapter 3 clarifies the ranges wherein the interpass dwell time, cooling rate, and hardness change in the practical application of DED. However, the dwell time or cooling rate chosen for desirable hardness may result in cracks easily occurring on the workpiece. Determining the appropriate deposition parameters is crucial because predicting and controlling cracking remains difficult. This chapter discusses the effect of substrate preheating by investigating the influence of an induction heater on crack generation in Co-based superalloys during DED. An induction heater was chosen because of its high efficiency, low waste heat, and ability to quickly and directly induce high workpiece temperatures. The material used in this study is Stellite 1, which is widely used for die cut rolls and screw shafts. To investigate the effect of preheating, experiments were conducted by changing the process parameters: preheating temperature and laser power.

The organization of this chapter is as follows. Section 4.2 provides the experimental setup and method. Section 4.3 investigates the influence of preheating temperature and laser power on hardness and crack development. Section 4.4 further investigates the influence of microstructure, dilution, and cooling rate. Finally, the conclusions of this chapter are outlined in Section 4.5.

4.2 Experimental Setup and Method

Two experiments were conducted. The objective of the first experiment was to investigate the effect of substrate preheating on crack generation in DED using an induction heater. To achieve this purpose, the following method was selected. The hardness of the deposited material was investigated after deposition with different preheating temperatures, irrespective of whether cracks developed or not.

The objective of the second experiment was to investigate how to prevent the surface hardness from decreasing during preheating. This was accomplished by adjusting the laser energy and induction energy. The targeted mechanical properties have been achieved with low laser energy and high induction energy [53]. Hence, the effect of laser power on surface hardness at the same induction heating energy was investigated in the second experiment.

4.2.1 Experimental Setup and Materials

Figure 4.1 shows a schematic of the DED process with induction preheating. The experimental setup used for this study consisted of a laser, an optical system, a powder nozzle, an induction heating device, and a radiation thermometer.

The substrate plate was set on the insulated block to minimize heat conduction from the substrate to the table. The induction heating device was placed below the substrate plate. The temperature of the substrate plate side was measured using a radiation thermometer because the temperature of the specimen’s surface varied owing to the influence of accumulated non-melted powder.

The type of laser was a fiber laser, with a maximum power of 8000 W. The spot diameter of the optical system was 3.0 mm. The type of powder nozzle was a multi-jet nozzle with four ports. Table 4.1 lists the specifications of the induction heating device and radiation thermometer. The substrate plate size was 100 mm × 100 mm × 10 mm, and the material was carbon steel, S50C. The surfaces of the substrate plate were machined by face milling to a surface roughness of Ra 6 μm.

Gas-atomized Stellite 1 powder of particle size 53–150 μm was used as the deposition material. The chemical composition of Stellite 1 is listed in Table 4.2.

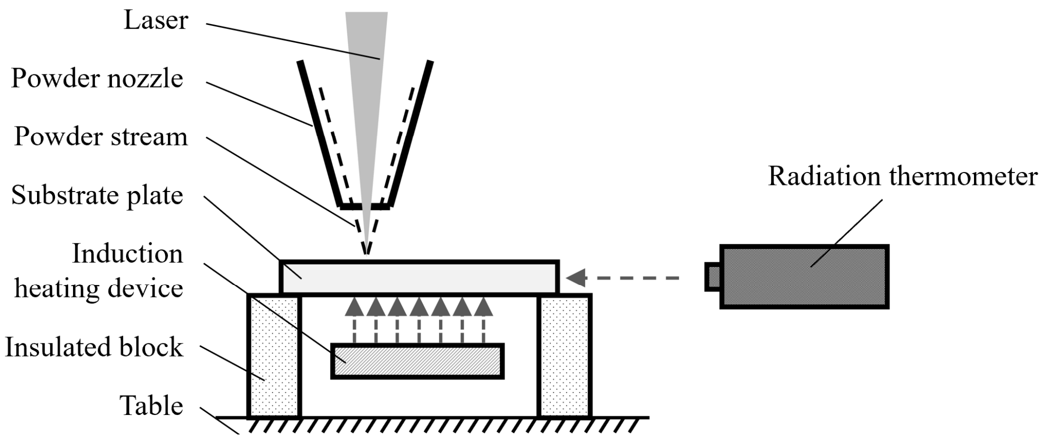

Fig. 4.1 Schematic of the DED process with induction preheating.

Table 4.1 Specification of the experimental equipment.

Induction heating device	Maximum power	10.0 kW
	Frequency	150-400 kHz
	Coil size	Φ70 mm
Radiation thermometer	Measurement range	400-3100 °C
	Resolution	1 °C
	Response time (95%)	0.1 s

Table 4.2 Chemical composition of Stellite 1 (in wt.%).

Co	C	Cr	Ni	W	Si	Fe	Mn
48.6	2.50	33.0	1.00	12.5	1.30	1.00	0.10

4.2.2 Experimental Method

A schematic of the deposition process and path pattern are shown in Fig. 4.2. Figure 4.2(a) shows seven test pieces on the substrate. The test pieces consisted of six tracks under the following respective conditions. The first track was deposited on the substrate 5 mm from the front and 15 mm from the left. The deposition length was 70 mm. The side-by-side overlap of the tracks was 50%, and the width of each of the six tracks was 10.5 mm. The distance between each set of six tracks was 2 mm. Laser irradiation commenced at the start of each track and stopped at the end of the track. Figure 4.2(b) shows the front view. As shown in Fig. 4.2(c), six tracks were deposited in a zigzag path. The first path started from the left-hand side and the second from the right-hand side, continuing back-and-forth until a total of six tracks were deposited. The arrow in Fig. 4.2 (c) indicates the deposition direction.

Table 4.3 lists the deposition conditions. These conditions were determined by preliminary single-track experiments. The powder feed rate was 25 g/min and remained within ± 3% of this value throughout the experiments. Argon gas, at a flow rate of 4 L/min, was used as a carrier gas to deliver the powder to the process zone. The same Argon gas, at a flow rate of 6 L/min, was used as a shield gas to protect the optics.

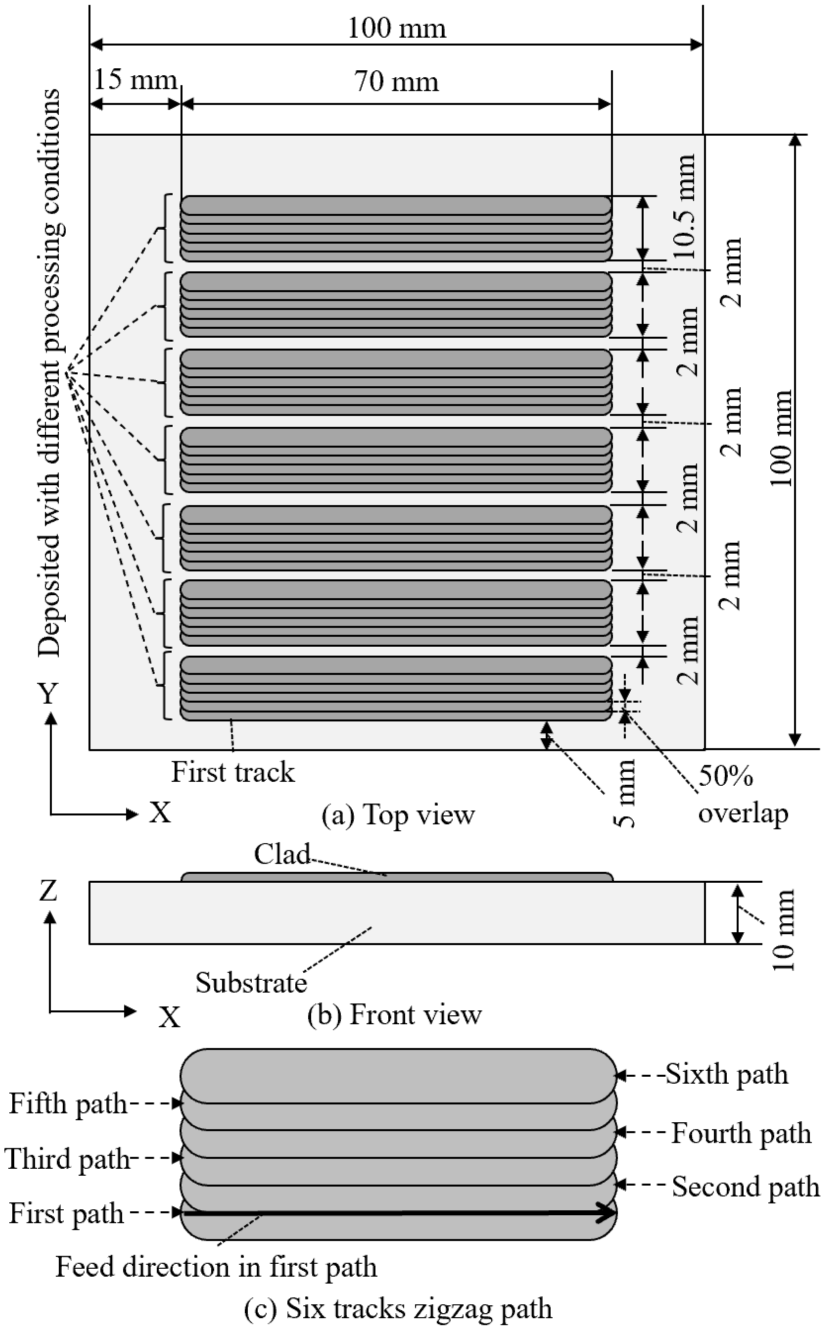

Fig. 4.2 Schematic of the deposition process and path pattern.

Table 4.3 Deposition conditions determined by single-track preliminary experiments.

Power [W]	Feed Rate [mm/min]	Powder Mass Flow [g/min]	Carrier Gas Flow Ar [L/min]	Shield Gas Flow Ar [L/min]	Diameter of Laser Beam [mm]
2400	1000	25	4	6	3.0

In the experiment investigating the influence of the preheating temperature on cracking and hardness, the preheating temperatures were 400, 500, and 600 ℃. In the experiment investigating the effect of laser power on the hardness of the surface, the preheating temperature was fixed at 500 ℃, and the laser power varied from 500 to 2400 W (500, 1000, 1500, 1750, 2000, and 2400 W).

4.2.3 Evaluation Method

This subsection describes the method used to evaluate the deposited test pieces. First, the crack generation process during deposition was observed. Figure 4.3 shows a schematic of the measurement apparatus. As shown in the figure, a high-speed camera, Phantom Miro LC311 (AMETEK, USA), was used to take images of the substrate from the front. The resolution was set to 640 × 400 pixels at a frame rate of 500 fps. An appearance evaluation was conducted to assess cracking. The deposited test pieces were cleaned and polished before examining the cracking within the deposited tracks.

Thereafter, the hardness of the test pieces was investigated. Each test piece was cut by wire EDM, and the cross-sections of the test pieces were polished. The hardness was measured on the polished surface by averaging the measurement results at five points. The measuring device used to test the hardness was an AAV500 micro-Vickers hardness tester (Mitsutoyo, Japan). A load of 1.9 N was applied to each indent. The measured point was 0.5 mm above the deposition surface to avoid influencing the substrate plate. Finally, a microstructural observation using scanning electron microscopy (SEM) Merlin VP Compact (Zeiss, Germany) and a compositional analysis using EDX XFLAS6-30 (BRUKER, USA) were performed on the cross-sections of the specimens.

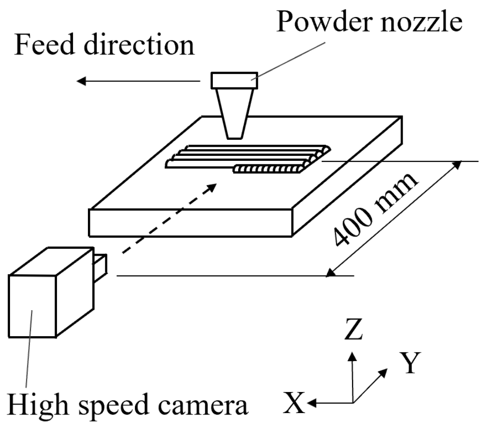

Fig. 4.3 Setup for crack observation using a high-speed camera.

4.3 Investigation of Hardness and Cracks

4.3.1 Influence of Preheating on Hardness and Cracks

Figure 4.4 shows an image of the test piece deposited with a laser power of 2400 W, but without preheating. As shown in the figure, cracks occur perpendicular to the deposition feed direction. All cracks are observed to extend through all six tracks. The conclusion can be drawn that crack generation occurred after all six tracks were deposited. Figure 4.5 shows the tracks deposited with preheating. As shown in the figure, no cracks occurred in the test pieces at 400, 500, or 600 ℃ preheating. The preheating mechanism having a profound effect on cracking is theorized to be a mixture of a reduction in thermal stress and cooling rate [54]. The three respective preheating temperatures were not observed to induce substantially different appearances.

Figure 4.6 shows the relationship between preheating temperature and hardness. The hardness without preheating was 770 HV. Conversely, the hardness with preheating was approximately 600 HV, indicating a decrease of approximately 175 HV.

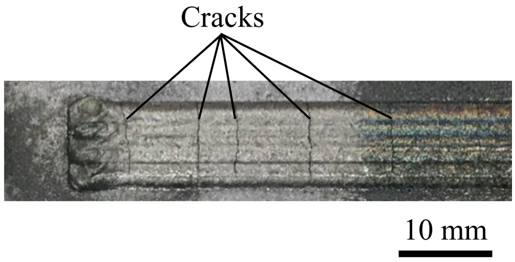

Fig. 4.4 Multiple cracks across a layer of Stellite 1, deposited on a S50C steel substrate without preheating (laser power of 2400 W).

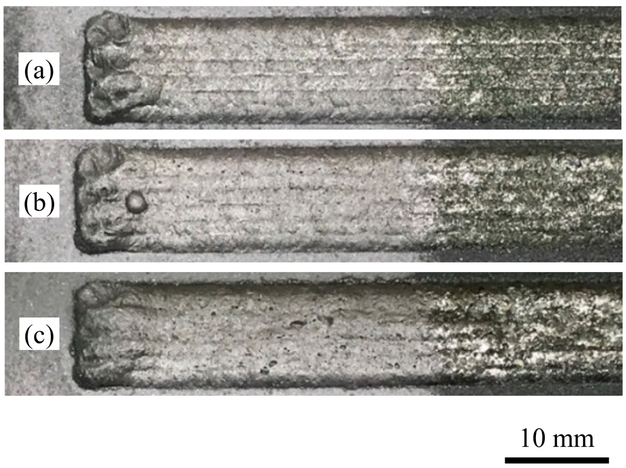

Fig. 4.5 Appearance of the test pieces at preheating temperature of (a) 400, (b) 500, and (c) 600 ℃ (laser power of 2400 W).

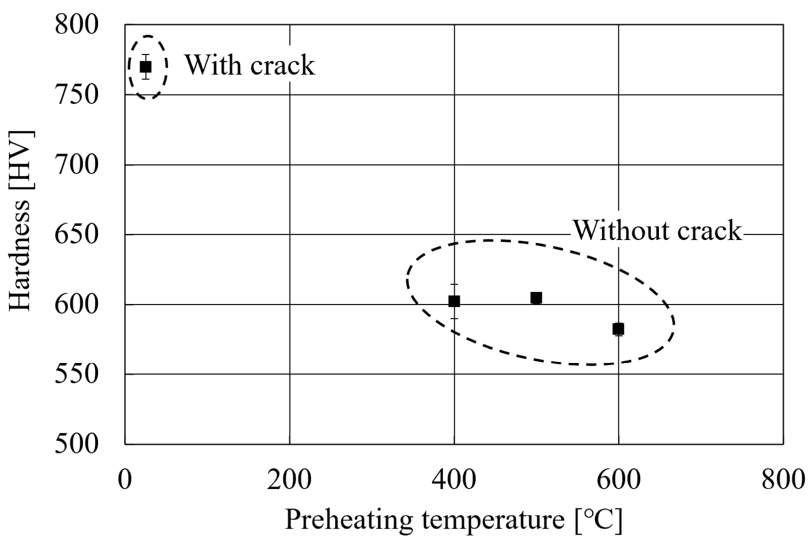

Fig. 4.6 Relationship between the preheating temperature and hardness of the test pieces (laser power of 2400 W).

4.3.2 Effect of Laser Power on Hardness and Cracks

Figure 4.7 shows the result of the appearance evaluation in the second experiment investigating the effect of laser power on the hardness of the surface, with the same induction heating energy. A melt pool did not form at 500 W (Fig. 4.7(a)) owing to a lack of heat energy. Several cracks can be observed at 1000 (Fig. 4.7(b)) and 1500 W (Fig. 4.7(c)). No cracks occurred above 1750 W (Fig. 4.7(d)–(f)). The boundary indicating whether cracks would or would not occur was found to be in the laser power range of 1500 to 1750 W in this test setup.

Figure 4.8 shows the relationship between laser power and hardness. Hardness has a negative correlation with laser power. The hardness for 1000 and 1500 W exceeds 700 HV, thus closer to the hardness value of 770 HV without preheating.

The range of hardness for Stellite 1 is 51–60 HRC (528–697 HV) according to the specification sheet provided by the powder supplier [55]. Because the average of this range is 612.5 HV, the hardness of the deposited test pieces should preferably exceed this average value. Although no cracks occurred at 2000 or 2400 W, the hardness under these conditions was less than 600 HV. Thus, hardness must be increased under these conditions. Deposition at a laser power of 1750 W did not induce cracks, and the hardness was 642.3 HV, which is 29.8 HV more than the average 612.5 HV. Therefore, the desired condition was 1750 W in this experiment.

The results of Subsections 4.3.1 and 4.3.2 show that cracks occur in the absence of preheating and no cracks occur when preheating is conducted. However, preheating decreases the hardness. When preheating is conducted, cracks occur, but hardness increases when laser power is reduced.

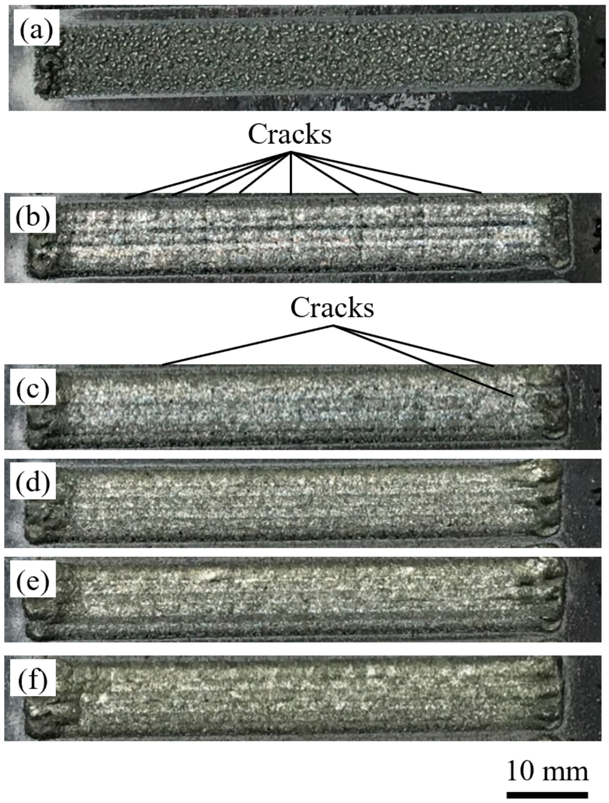

Fig. 4.7 Appearance of the test pieces at a preheating temperature of 500 ℃ and laser power of (a) 500, (b) 1000, (c) 1500, (d) 1750, (e) 2000, and (f) 2400 W.

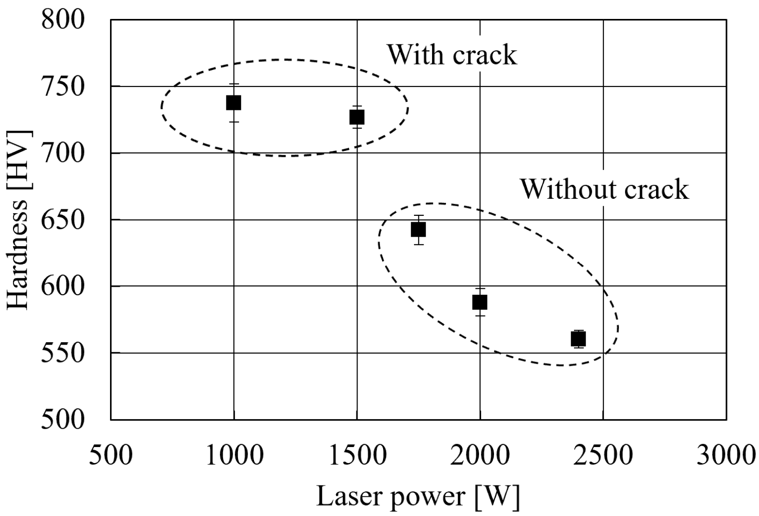

Fig. 4.8 Relationship between laser power and hardness of the test pieces (preheating temperature of 500 ℃).

Figure 4.9 shows the results of the crack observation using the high-speed camera during deposition with no preheating and a laser power of 2400 W. In the figure, “0 frame” is the time at which the deposition of the sixth track was completed and the laser was turned off. In other words, the images were taken after the powder nozzle had already passed. Note that the powder nozzle’s track direction was from right to left, from the perspective of the camera, as shown in Fig. 4.3. Figure 4.9(a), (b), (c), and (d) show the deposited track before crack development, a crack parallel to the track, a crack parallel to the track 0.5 s after solidification, and a crack perpendicular to the track, respectively. Cracks can be observed both after deposition of all six tracks, as shown in Fig. 4.4, and also immediately after solidification of one deposited track.

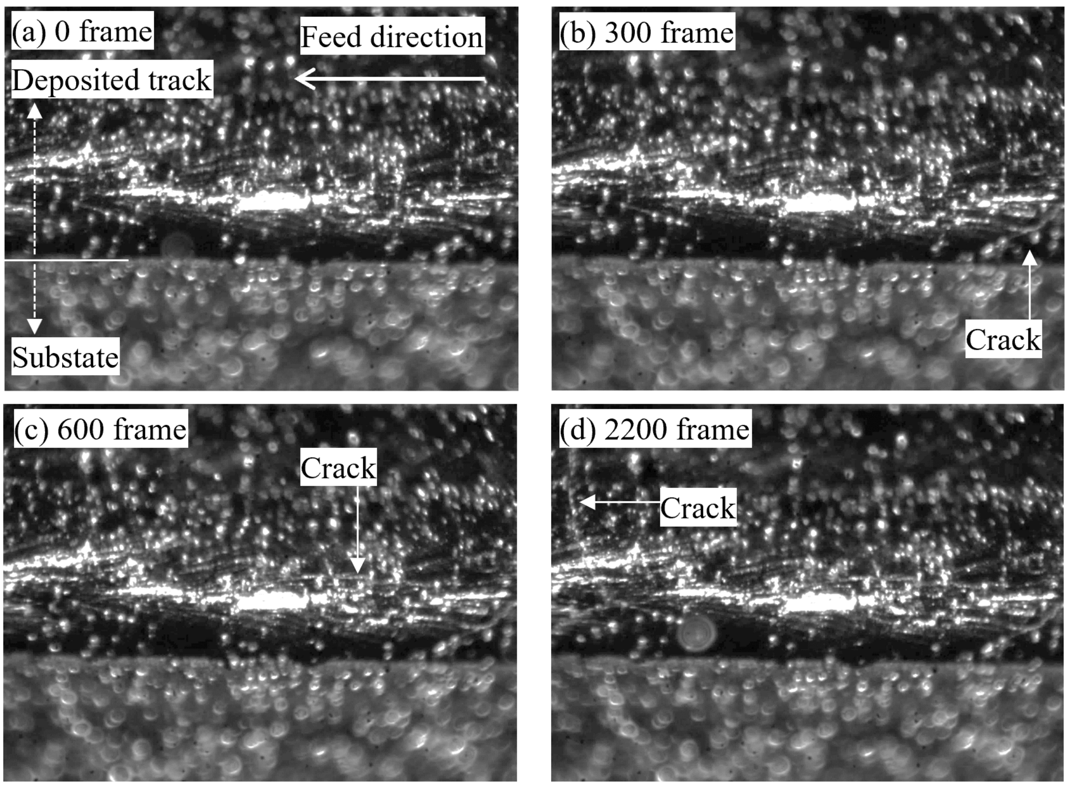

Fig. 4.9 Observation of cracks using images taken with a high-speed camera:
(a) before crack generation at 0 frame, (b) parallel crack with path at 300 frame,
(c) 0.5 s after solidification at 600 frame, and (d) vertical crack with path at 2200 frame.

4.4 Investigation on Crack Occurrence and Hardness Variation Mechanisms

4.4.1 Influence of Microstructure

Based on the results of a previous study, one can infer that carbide precipitates influence crack development and hardness [56]. In that study, steel was coated with Stellite 6 powder using high-speed flame spraying. The microstructure of the coating was described as consisting of Co-rich dendrites, surrounded by hard carbide particles ($Cr_{23}C_6$). This coating was found to reduce the tensile strength of the base metal.

In this study, microstructural observations by SEM and composition mapping by EDX were performed on the deposited specimens. Figure 4.10 shows the SEM images for the specimens deposited in the first experiment. The figure shows that, without preheating, the precipitates extending needle-like in the direction of the substrate (Z direction) are densely distributed in large quantities. In the upper part of the coating (A), precipitates can be observed to be randomly oriented without any direction. The thickness of the precipitates increases with increasing preheating temperature, and the density of the precipitates decreases.

Compositional mapping by EDX was performed to investigate the composition of the precipitates. Figure 4.11 shows the results obtained for the middle part of the coating (B) of the test piece deposited in the first experiment with a preheating temperature of 500 ℃ and a laser power of 2400 W. A comparison between Figs. 4.11(a) and 4.10 reveals that the precipitate is a Cr-rich phase. Figure 4.11(b) shows that the Cr-rich phase also contains carbon, i.e., the phase is presumed to be composed of carbide particles such as $Cr_{23}C_6$ or Cr_7C_3. In other words, without preheating, the amount of hard, brittle carbide particles increased in the deposited material. This increase resulted in an increase in hardness and cracking susceptibility, eventually leading to crack formation. As shown in Fig. 4.11(c), Co, a major component of Stellite 1, is found in higher concentrations, whereas Cr is not, and vice-versa.

For a more detailed investigation, the obtained SEM images were binarized to quantify the ratio of the Cr-rich phase in the deposited material. Figure 4.12(a) shows the SEM images of the middle part of the coating (B) and binarized images from the first experiment with different preheating temperatures. Figure 4.12(b) shows the

SEM images from the second experiment, in which the laser power was varied combined with preheating. In the SEM images, the microstructure appears to transition into a fine needle-like structure, and the density of the precipitates increases as the laser power or prehearing temperature decreases. This trend is similar to that observed in Fig. 4.10, which shows the results with and without preheating, suggesting that the cooling rate influenced the observed microstructure. These outcomes are consistent with the results of a previous study that reported higher material hardness when needle-like precipitates were densely distributed, as well as cellular growth owing to a large temperature gradient and equiaxed dendrite growth owing to a small temperature gradient (Smoqi et al., 2022) [18]. The top surface of the coating was observed to have a shape similar to that of an equiaxed dendrite owing to slow cooling.

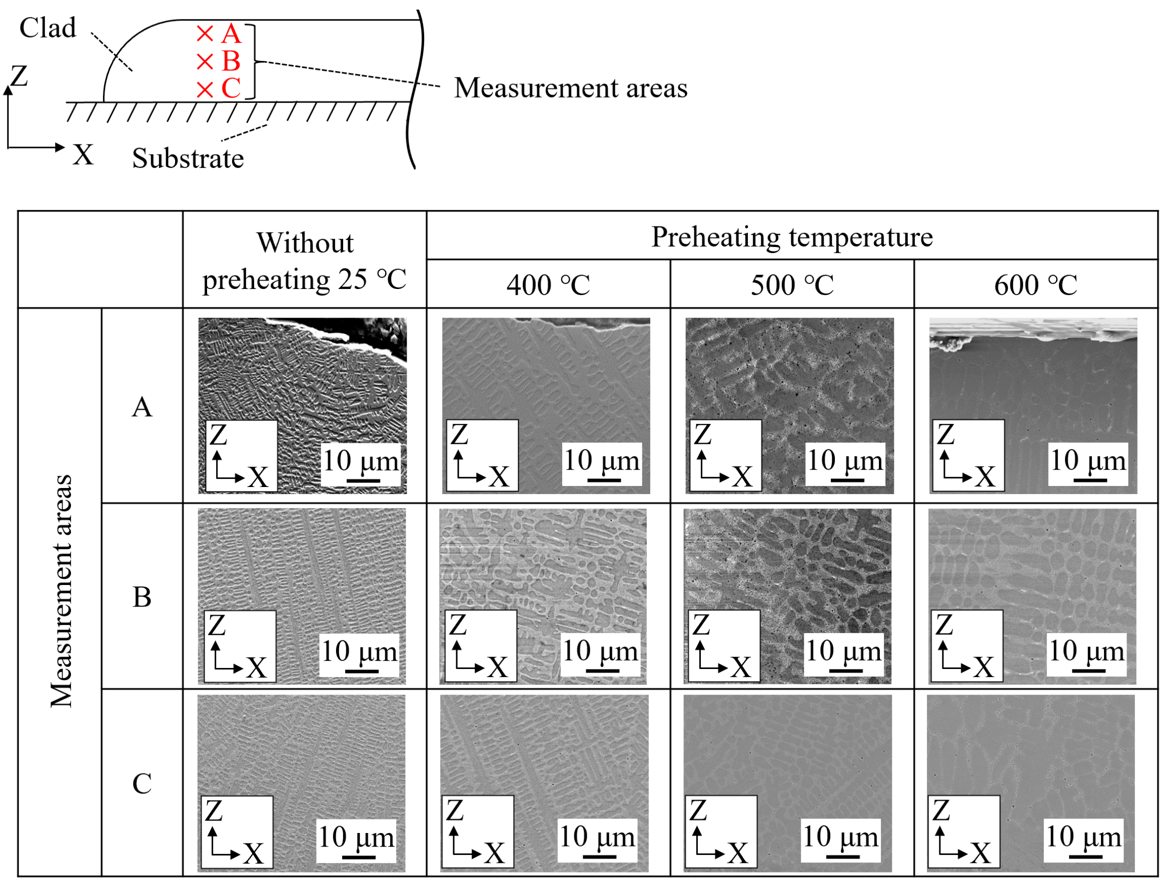

Fig. 4.10 SEM images for each test piece deposited with different preheating temperatures.

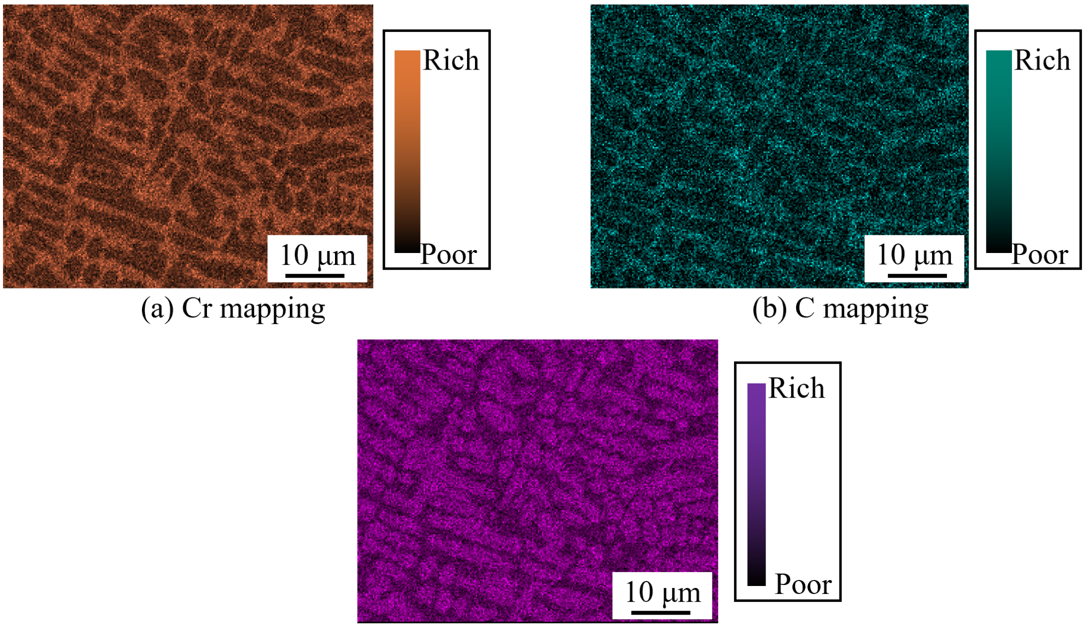

(a) Cr mapping

(b) C mapping

(c) Co mapping

Fig. 4.11 EDX mapping images of the test piece deposited with a preheating temperature of 500 ℃ and laser power of 2400 W (measurement area is B as for Fig. 4.10).

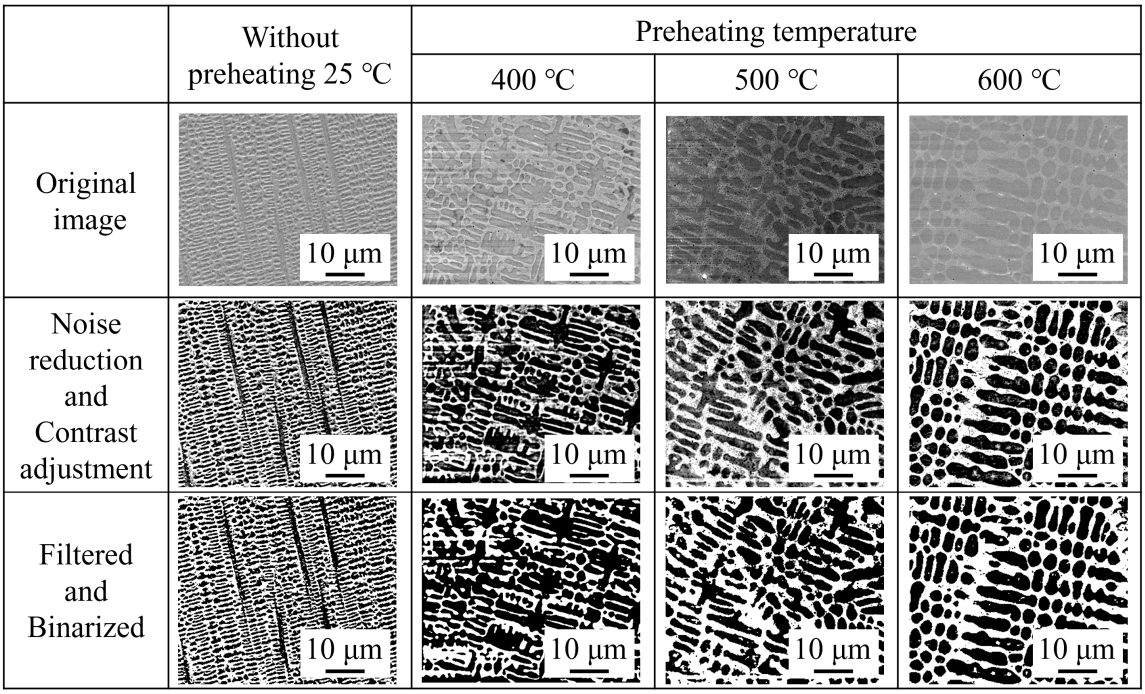

(a) Test pieces deposited with different preheating temperature

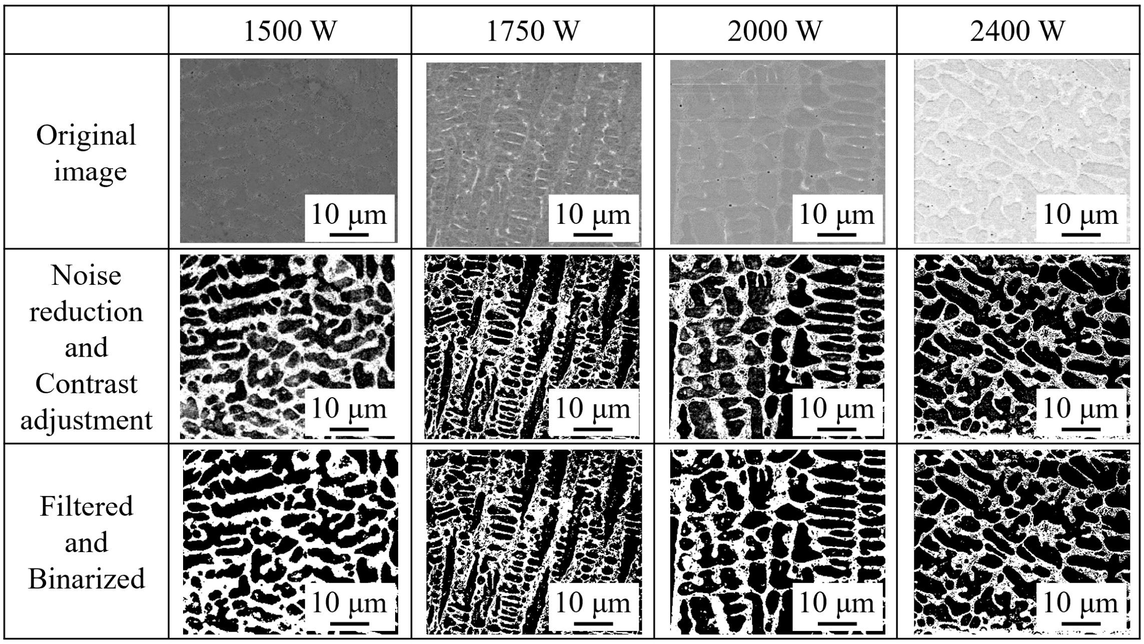

(b) Test piece deposited with different laser power

Fig. 4.12 SEM and its binarized images.

The binarized images shown in Fig. 4.12 reveal Cr-rich areas, shown in white, indicating that the previously discussed carbide particles contribute to a more brittle yet hard material. The ratio of the white part to the rest of the image was used to express the relationship in Fig. 4.13, which shows the ratio of the Cr-rich phase obtained by binarization and the hardness in the first and second experiments, respectively. Figure 4.13 reveals a correlation between the ratio of the Cr-rich phase and the hardness of Stellite 1. The black areas in the binarized images indicate that the amount of Cr in these areas is lower than the white areas. Thus, the black areas are Co-rich phases; the Cr is presumed to have been dissolved in the Co as pointed out in previous research [57].

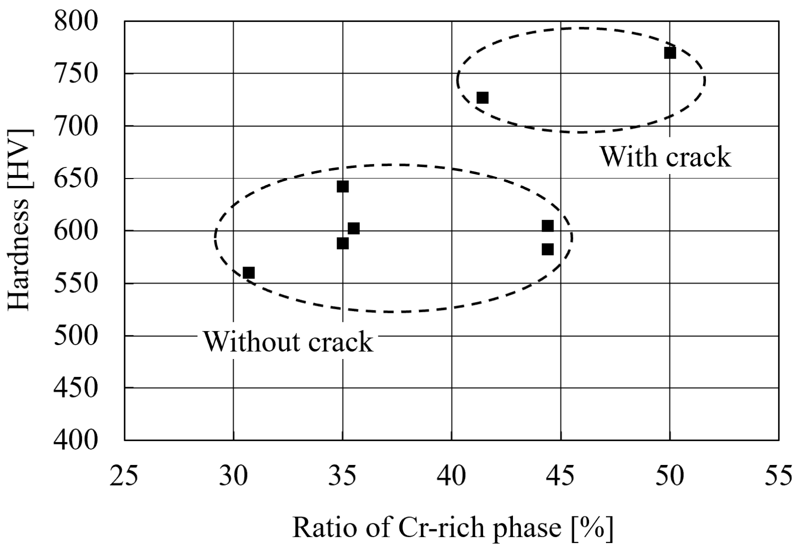

Fig. 4.13 Relationship between hardness and the Cr-rich phase ratio for each test piece.

4.4.2 Influence of Dilution

The possibility of a reduction in hardness owing to dilution was also investigated. The relationship between the intensity of Fe and depth was investigated using EDX line mapping. Figure 4.14 shows an example of the EDX line mapping results and a schematic thereof. In Fig. 4.14(a), the cyan line indicates the intensity of Fe in the SEM image shown in the background. In Fig. 4.14(b), the horizontal axis indicates Fe intensity, and the vertical axis indicates the position in the depth direction from the surface of the deposited material. Below depth A, the Fe intensity is high because of the S50C substrate. However, Fe intensity decreases from depth A to depth B before ultimately becoming constant. The low Fe intensity represents the deposited Stellite, and the transition from depth A to depth B represents the dilution zone. Therefore, the distance between depth A and depth B represents the dilution zone depth.

Figure 4.15 shows the measurement results for the specimens deposited with different preheating temperatures and their associated estimated dilution zone depths. The figure demonstrates that the degree of dilution does not change significantly, regardless of the preheating temperature. In other words, the substrate component is not likely to diffuse and influence the composition of the deposited material. Thus, dilution does not have a considerable effect on hardness and crack development.

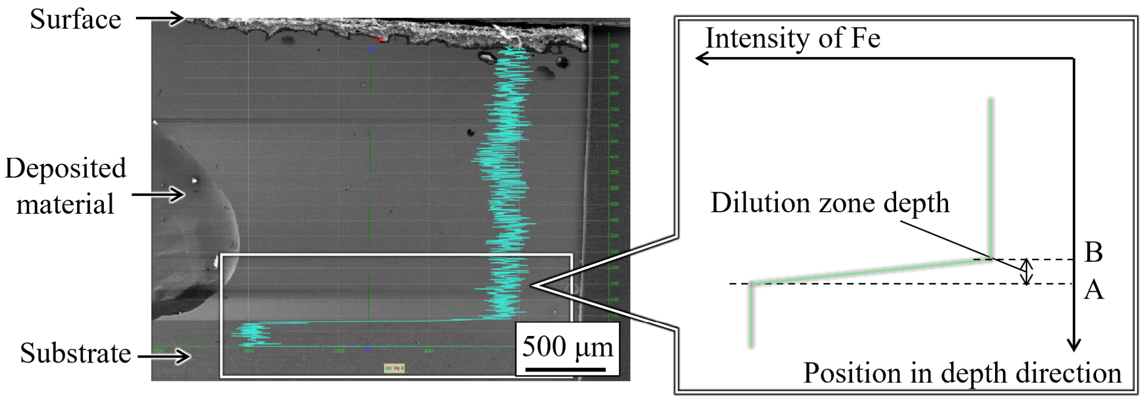

(a) Example of EDX line mapping result

(b) Schematic diagram of EDX line mapping result

Fig. 4.14 EDX line mapping example of Fe intensity and a schematic thereof.

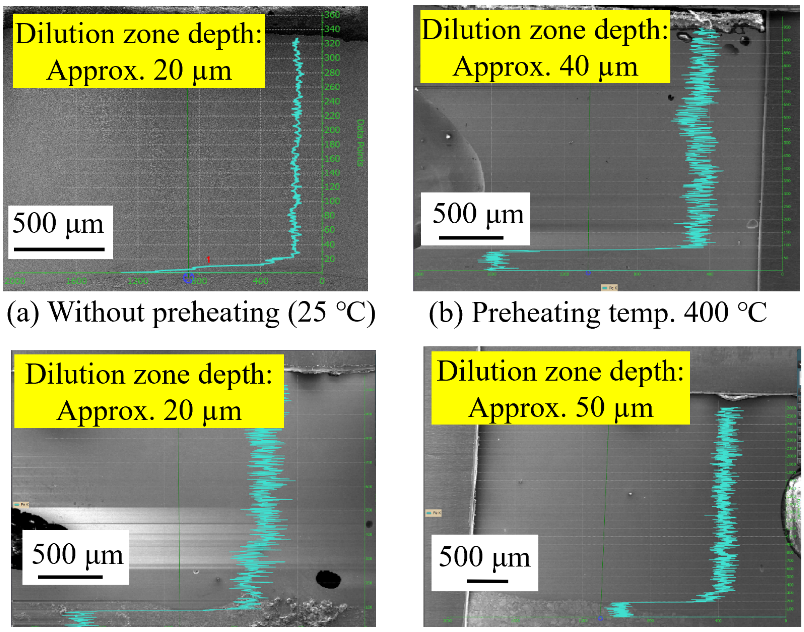

(a) Without preheating (25 °C) (b) Preheating temp. 400 °C

(c) Preheating temp. 500 °C (d) Preheating temp. 600 °C

Fig. 4.15 Dilution zone depth estimated by EDX line mapping for each test piece deposited with different preheating temperatures.

4.4.3 Influence of Cooling Rate

The change in material properties owing to carbide particle precipitation can be inferred to affect hardness and crack development. Moreover, the magnitude of thermal stress is considered to influence the development of cracks or lack thereof. Thermal strain is known to decrease when the cooling rate is low [58], indicating that it is dependent on the cooling rate.

Hence, to investigate the cooling rate, the spacing of the dendrite arms was investigated. In a previous study, dendrite arm spacing was measured using the SEM images of specimen cross-sections to obtain the cooling rate; the study highlighted a negative correlation between arm spacing and the cooling rate [18]. They also calculated the cooling rate from the following relationship,

$$\lambda_1 = 80(\varepsilon^{-0.33}), \tag{4.1}$$

where λ_1 is the dendrite arm spacing [μm], and ε is the cooling rate [K/s]. Using this equation, the cooling rate can be expressed as a function of the dendrite arm spacing as follows:

$$\varepsilon = (\lambda_1/80)^{-\frac{1}{0.33}}. \tag{4.2}$$

In this study, dendrite arm spacing was measured using specimens deposited in the first and second experiments. The cooling rates were calculated using Eq. (4.2). The results are shown in Figs. 4.16 and 4.17. Note that Eq. (4.1) was proposed for stainless steels and thus requires further investigation to estimate the exact cooling rate for Stellite 1, which was used in this study.

To confirm the validity of the relationship between the dendrite arm spacing and cooling rate, the results were compared with those of previous research. The dendrite arm spacing in this study, ranging from 2.0 to 8.0 μm, was relatively higher than that observed in previous research of 1.0 to 1.6 μm [59]. The difference can be attributed to the feed rate used in the previous research of 4000 to 6000 mm/min which was higher than the 1000 mm/min in this study, as well as the finer microstructure obtained by the higher speed feed rate in the previous research. In this study, the cooling rate ranged from 0.2×10^4 to 3.5×10^4 K/s, thus outside the range typically associated with laser cladding of 5×10^3 to 5×10^5 K/s, as defined by previous research [52]. Considering that Vilar also states that the range is dependent on the processing parameters, the lower cooling rate is assumed to be a direct result of the preheating performed during the experiments in this study. Figures 4.16 and 4.17 show that the dendrite arm spacing tends to become narrower in the case of no preheating or with lower laser power in the case with preheating. Furthermore, under these conditions, the cooling rate is higher and the thermal stress is assumed to be higher, thus cracking occurs.

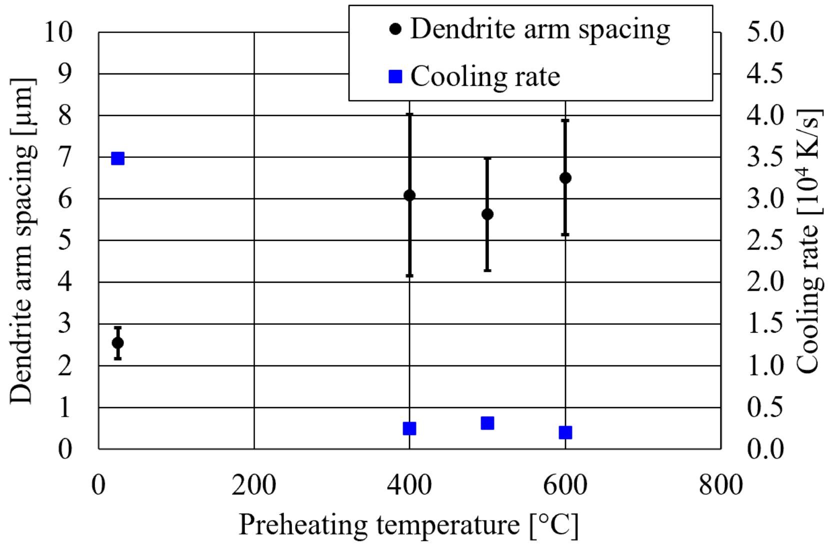

Fig. 4.16 Relationship between preheating temperature and the dendrite arm spacing and cooling rate.

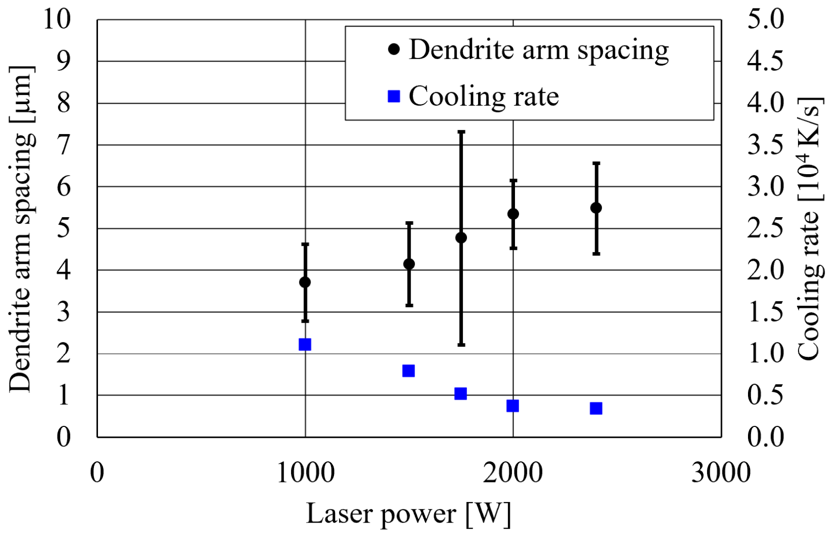

Fig. 4.17 Relationship between laser power and the dendrite arm spacing and cooling rate.

4.5 Summary of Chapter 4

In this chapter, the effects of substrate preheating with an induction heater and laser power on crack development in DED for Co-based superalloy Stellite 1 were investigated. The findings of this chapter are summarized as follows.

1) For a laser power of 2400 W, cracks did not develop when the preheating temperature was 400 ℃ or higher. For a laser power of 1750 W or higher, cracks did not develop when the preheating temperature was 500 ℃. Among the deposition conditions, a sufficient hardness of 642.3 HV was obtained when the preheating temperature and laser power were 500 ℃ and 1750 W, respectively.

2) Although cracking did not occur when the preheating temperature or laser power was high, the hardness decreased. A trade-off exists between high hardness and low crack frequency that is considered to be influenced by thermal stress and the amount of precipitated chromium carbide, which is a hard and brittle material. These two factors are affected by the cooling rate of deposition. The higher the cooling rate, the more chromium carbides precipitate, and the harder the deposited material, the more likely cracks are to develop. In addition, the higher the cooling rate, the greater the thermal stress.

3) Controlling the cooling rate is important for preventing cracking and hardness reduction. The results presented in this study can provide a guideline for the coating and cladding of Co-based superalloys by DED, as Co-based superalloys are widely used for die-cut rolls or screw shafts.

5 Influence of Thermal History

5.1 Introduction

In this chapter, the effects of thermal history on workpiece hardness and cracking in the cladding of M2 high-speed steel were investigated through a combination of numerical and experimental techniques. A simple thermal model was developed to simulate the workpiece temperature during deposition.

The organization of this chapter is as follows. Section 5.2 explains the thermal simulation model used in this study and discusses the validity thereof. Section 5.3 describes the experimental setup and method. Section 5.4 provides the experimental results. Section 5.5 discusses the influence of thermal history on the quality of the workpiece deposited by DED based on the obtained results. Finally, the conclusions of this chapter are outlined in Section 5.6.

5.2 Thermal Simulation

5.2.1 Simulation Specifications

This subsection describes the numerical analysis model for simulating the temperature history of a workpiece. In this analysis, the temperature evolutions of the deposited material and starting substrate are calculated from the transient heat input generated by the laser source. The governing equation for the analysis is a three-dimensional heat conduction equation derived from the conservation of thermal energy in the material and is expressed as follows:

$$\frac{\partial T}{\partial t} = \frac{k}{\rho c}\Delta T + \frac{\dot{q}}{\rho c}, \tag{5.1}$$

where T denotes temperature, t denotes time, k denotes thermal conductivity, ρ denotes density, c denotes specific heat, and q denotes heat generation per unit volume per unit time. Normally, material coefficients such as thermal conductivity, specific heat, and density are a function of temperature; for simplicity, these coefficients are fixed at room temperature in this analytical model. In addition, to simplify the model as far as possible for the thermal analysis of DED, only heat conduction in the rigid body is considered. The heat input from the laser and heat dissipation from the deposited workpiece are combined to calculate q. As shown in Eq. (5.2), the heat input from the laser is assumed to follow the Bouguer–Lambert–Beer Law [60]. In addition, two types of heat dissipation from the deposited workpiece are considered: convective heat transfer and radiation, as shown in Eqs. (5.3) and (5.4).

$$q_{laser}(x,y,z,t) = (1-R)q_0 \exp\left(-\frac{x^2+y^2}{{r_0}^2}\right)\exp(-\alpha z), \tag{5.2}$$

$$q_{convection}(x,y,z,t) = h(T-T_{air}), \tag{5.3}$$

$$q_{radiation}(x,y,z,t) = \varepsilon\sigma\left(T^4-T_{air}^4\right), \tag{5.4}$$

where R denotes reflectance, q_0 denotes incident laser density, r_0 denotes laser radius, α denotes absorption coefficient, $q_{convection}$ denotes the convective heat transfer per unit area, h denotes the heat transfer coefficient of the atmosphere, T_{air} denotes the temperature of the atmosphere, $q_{radiation}$ denotes the thermal radiation per unit area, and σ denotes the Stefan–Boltzmann constant. Here, z in Eq. (5.2) is the coordinate axis taken from the laser irradiation point to the inside of the workpiece, and x and y are axes so that the system is right-handed, as shown in Fig. 5.1. Eq. (5.5) is used to calculate $\dot{q}$ in Eq. (5.1).

$$\dot{q}(x,y,z,t) = q_{convection} + q_{radiation} + \frac{\partial q_{laser}}{\partial z}. \tag{5.5}$$

A finite difference method is used for the numerical calculations. The program is designed to use a computational domain corresponding to the deposited workpiece, which follows the laser path trajectory. A schematic of the algorithm flow of this program is shown in Fig. 5.2.

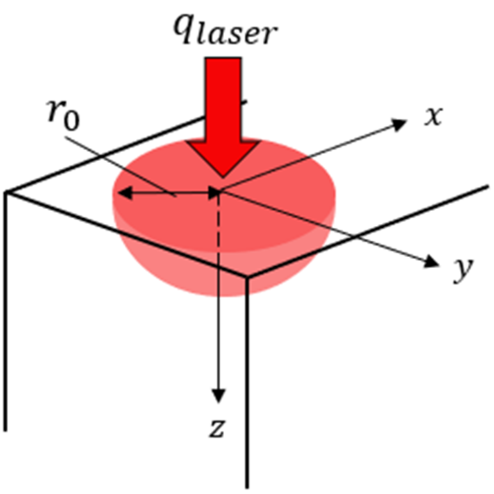

Fig. 5.1 Schematic of the local coordinate system in the laser heat input equation.

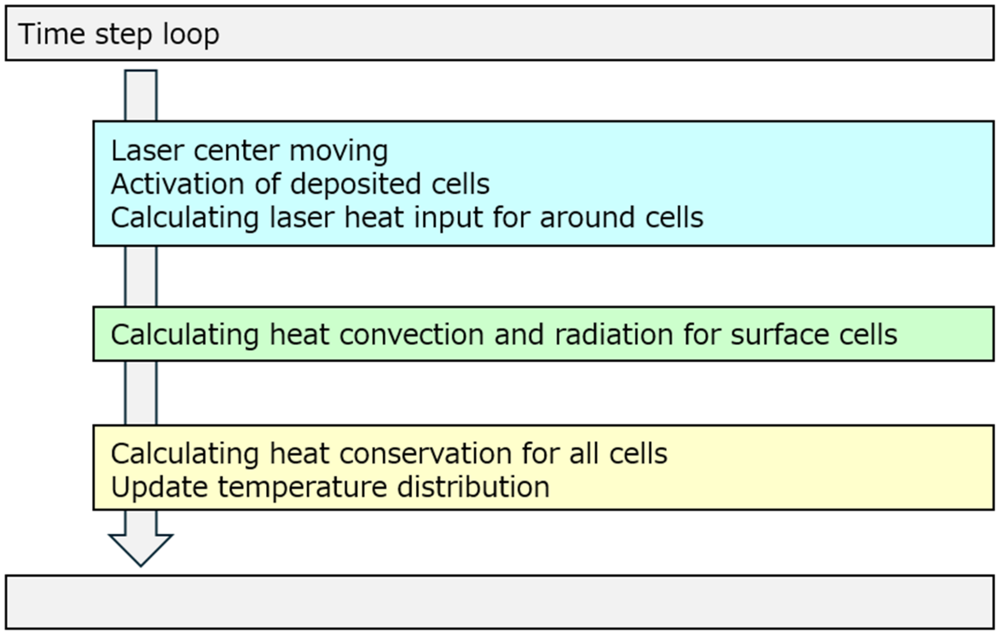

Fig. 5.2 Algorithm flow for heat transfer simulation.

The program has the following features:

1) The laser irradiation point moves along the laser path with the time evolution; concurrently, the heat input calculation is performed on the cells around the irradiation point.

2) The group of cells to be deposited is prepared before the calculation begins, and cell activation is performed at each time step in the vicinity of the laser irradiation point. This allows the DED process to be modeled as the calculation area is added as time evolves.

The aim of this program is to build a model that is simple enough to perform a temperature analysis of the DED process. In particular, note that the following points are not considered.

- Solid–liquid phase changes and associated changes in physical quantities and governing equations
- Formation and transformation of the crystal structure and associated changes in various physical quantities
- Temperature dependence of physical quantities such as specific heat and thermal conductivity
- Cracks and voids in depositions and deformation owing to strain
- Changes in height and shape of the deposit owing to deposition defects
- Simulation of fluid motion inside a melt pool
- Change in reflectance of materials depending on the angle of laser incidence
- Influence of spatter and unmelted powder adhering to objects

In the next section, the qualitative and quantitative validity of the model are discussed.

5.2.2 Simulation Validation

To confirm the validity of the thermal analysis, the temperature measurement results of the simulation were compared with those of the deposition experiment. A thin-wall deposit was produced using SUS304 as the base material and SUS316L as the deposited material. As shown in Fig. 5.3, the surface temperature of the wall was measured by an infrared thermometer to record changes during deposition. A numerical analysis was performed under the same deposition conditions. The average temperature in the same area as the measured range was output at 30 Hz. For computational efficiency, the mesh size was set to (Δx, Δy, and Δz) = (0.5, 1, and 0.1 mm).

Figure 5.4 compares the measured and numerical results. Both models show qualitative agreement, with an initial temperature increase to a peak followed by a gradual temperature decrease. Quantitatively, a difference of up to 20 % is observed; this accuracy is considered sufficient for an analysis approach using a simplified model that does not consider temperature dependent changes in thermodynamic coefficients or phase changes. To further improve the accuracy, the mesh size resolution could be increased to capture powder or fluid movements in the melt pool. However, decreasing the mesh size down to 1 μm for improved resolution would increase the computation time by an estimated 109 times. The accuracy achieved under the current simulation conditions is therefore considered a good balance between accuracy and computation time.

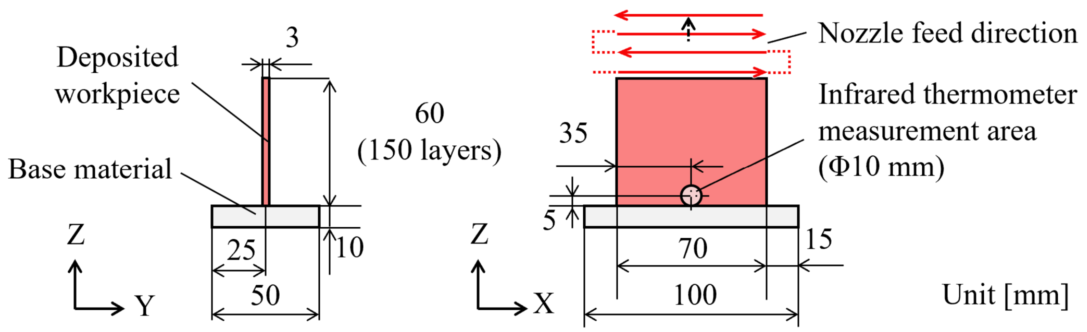

Fig. 5.3 Schematic of the wall deposition experiment.

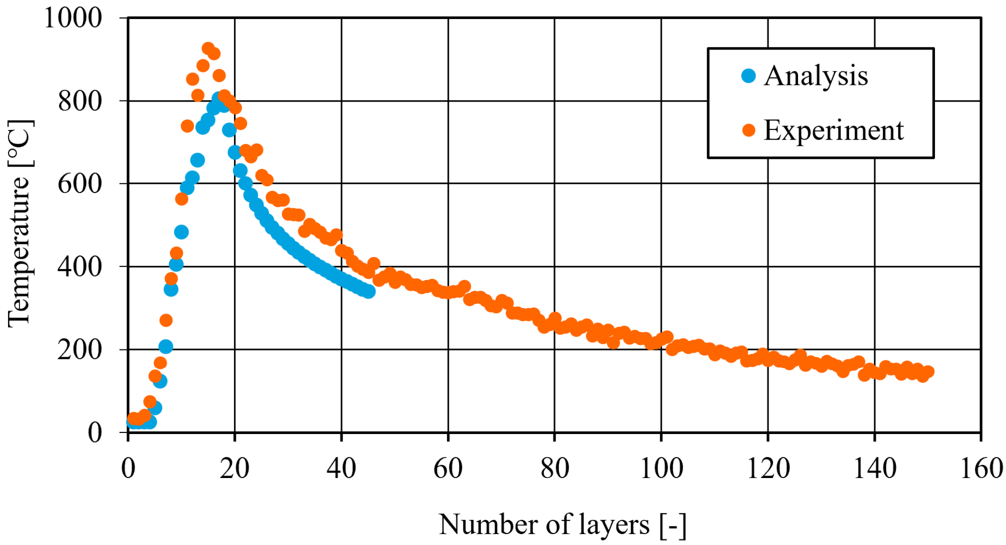

Fig. 5.4 Comparison between the measured and simulated workpiece temperatures during thin-wall deposition.

5.3 Experimental Setup and Method

5.3.1 Experimental Setup and Method

The purpose of the experiment was to investigate the effects of thermal history on crack development and hardness within the deposition tracks and overall workpiece. The experimental apparatus used in this study is shown in Fig. 5.5. The laser beam was irradiated from the deposition head through the center of the laser nozzle with a shield gas to form a melt pool on the base material. Metal powder was simultaneously fed through axisymmetric nozzles for the addition of material. The powder used was M2, a type of high-speed steel that is commonly used in cladding applications. A rectangular block was deposited by fabricating 5 identical layers with 6 linear depositions per layer. The thermal history was varied by changing the interpass dwell time between the lines and layers. Table 5.1 lists the deposition parameters and conditions. The workpieces are hereafter referred to as N1 to N5.

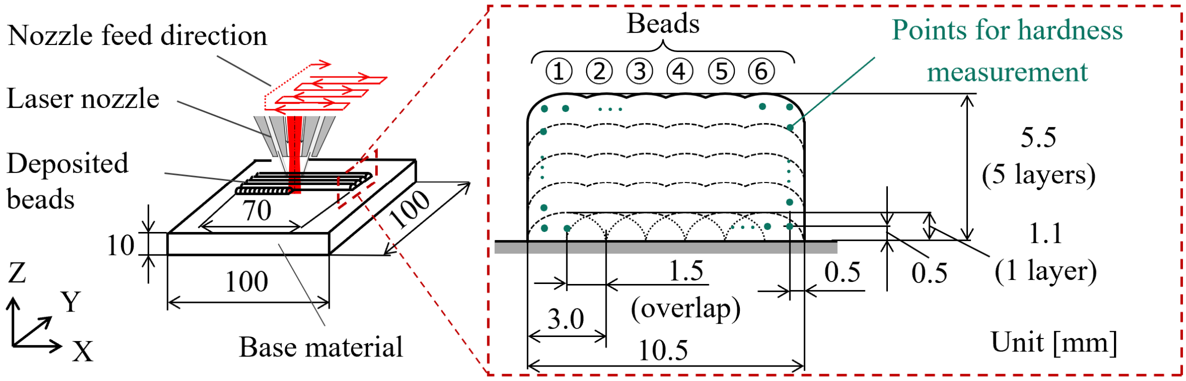

Fig. 5.5 Experimental setup.

Table 5.1 Deposition parameters and conditions for each workpiece.

Workpiece No.	N1	N2	N3	N4	N5
Laser power [W]	2200 (1st layer), 1600 (2nd to 5th layer)				
Feed rate [mm/min]	1000				
Powder feed [g/min]	12				
Layer thickness [mm]	1.1				
Interpass dwell time on a path level [s]	0	3	6	6	6
Interpass dwell time on a layer level [s]	0	0	0	12	24

5.3.2 Evaluation Method

After deposition, the workpiece was sectioned with a grinding disc, and the cross-section was polished. Hardness was measured at 0.5 mm intervals in the build and horizontal directions. The interface between the base material and deposited workpiece was used as the height reference (0 mm) in the hardness measurement. The measuring instrument used was an AAV500 micro-Vickers hardness tester (Mitsutoyo, Japan).

5.4 Investigation

Figure. 5.6 shows images of the deposited workpiece. As shown in the figure, no visible cracking occurred in N1 (zero dwell time). For N2, with an interpass dwell time on a path level of 3 s, a 6 mm visible crack can be observed in the perpendicular direction with respect to the toolpath direction. For N3, with a dwell time of 6 s, the number of visible cracks increased to two, also occurring in the middle of the workpiece in the longitudinal direction. For N4, with an interpass dwell time on the layer level of 12 s, an additional visible crack formed on the right-hand side of the figure, thus totaling three cracks. The cracks were observed to increase in length and span the width. Compared to N4, no change was observed for N5, with an interpass dwell time on the layer level of 24 s. These tendencies observed in terms of number, position, and length of cracking were also observed on other samples deposited under the same deposition conditions.

Figure. 5.7 shows the measurement results for the entire hardness map of the N5 cross-section. More variations in the build and horizontal directions were observed; therefore, finer linear interval hardness measurements were taken. Figs. 5.8 and 5.9 show the hardness distribution in the horizontal direction at a height of 0.5 mm and in the build direction at the mid position of the cross-section, respectively. Although the hardness distributions in both directions exhibit periodic fluctuations, the amplitude of the hardness distribution in the build direction of approximately 200 HV is larger than that in the horizontal direction (approximately 100 HV). Given the higher fluctuation amplitudes in the build direction, subsequent work focused on this orientation. Note that the hardness distribution was also measured for other samples, resulting in similar periodic fluctuations in the directions shown in Figs. 5.8 and 5.9.

As shown in Fig. 5.9(a), the workpieces without dwell time exhibit uniform hardness, whereas cyclic hardness fluctuations are observed for N2, with an interpass dwell time on the path level of 3 s. This is particularly evident within the first layer. For N3, with a dwell time of 6 s, hardness fluctuations are also observed in the second layer. In contrast, as shown in Fig. 5.9(b), the hardness and periodic fluctuation trend did not change when the interpass dwell time changed on the layer level or when the dwell time on the path level was fixed at 6 s. Note that although the EBSD analysis of the workpiece cross-section was performed, no significant difference in grain size was observed at the positions where hardness fluctuations were observed.

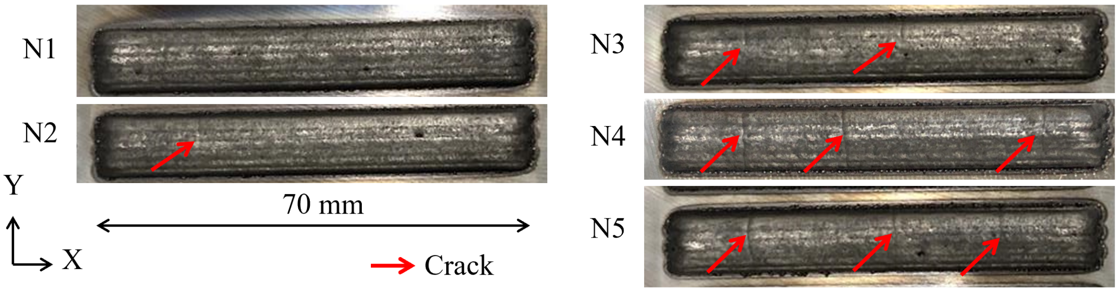

Fig. 5.6 Images of deposited workpieces.

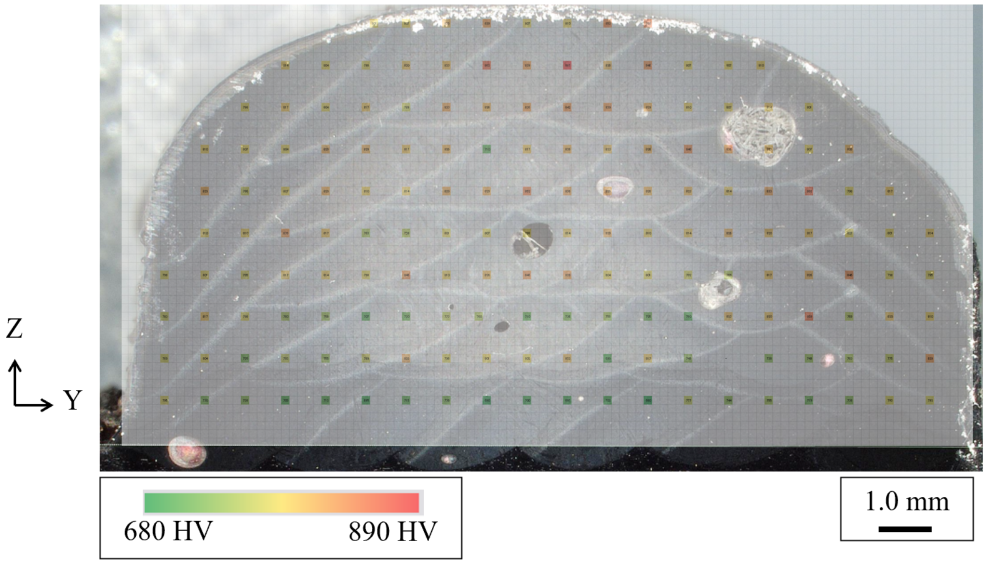

Fig. 5.7 Entire hardness map of the N5 cross-section.

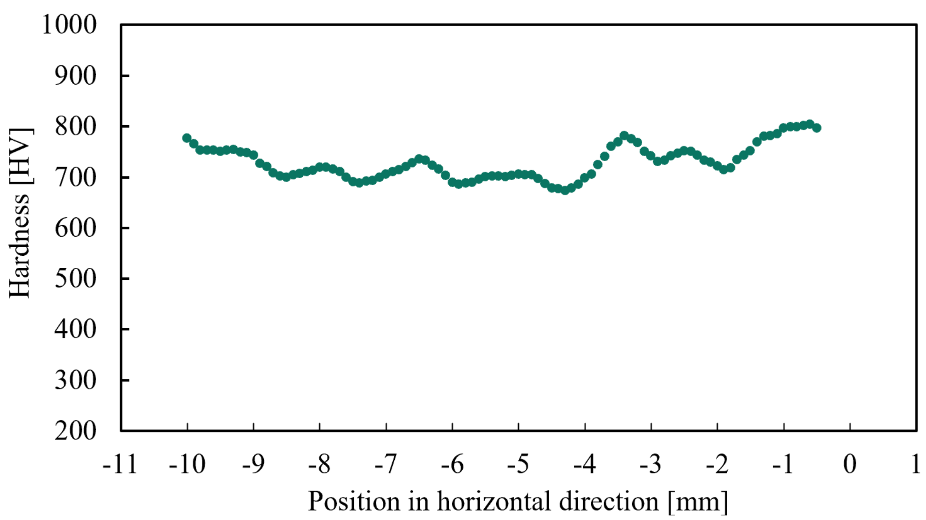

Fig. 5.8 Hardness distribution in the horizontal direction for N5 (0.5 mm height).

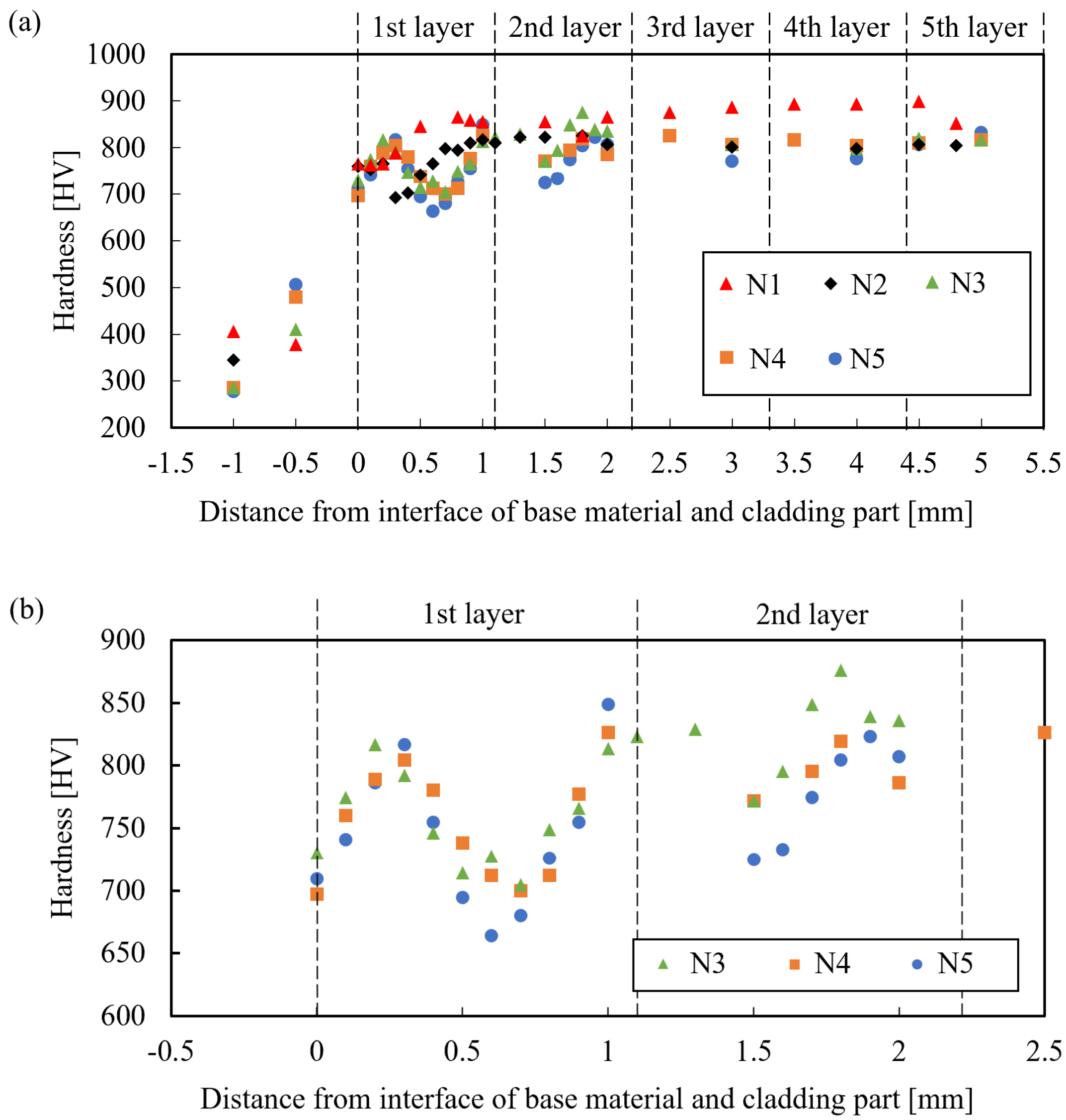

Fig. 5.9 Measured hardnesses for (a) all samples, (b) samples deposited with the same dwell time on the path level and different dwell times on the layer level.

5.5 Discussion

5.5.1 Mechanism Hypothesis

Based on the findings of Costa et al., the vertical variation in hardness can be attributed to tempering [36]. If the hardness measurement point is higher (as in the case of the build direction) within the sample cross-section, tempering is less likely to occur at that point. This is because the thermal history at that point is less likely to have a temperature lower than the martensitic phase change temperature (hereinafter referred to as Ms point). In the next subsection, these hypotheses will be evaluated based on the results of the temperature simulation.

5.5.2 Thermal History Analysis

To calculate the temperature distribution inside the samples, the simulation described in Section 5.2 was performed under the same conditions as the deposition experiment described in Section 5.3. Figure 5.10 shows the results of the thermal history analysis at different build heights. Note that the Ms point was set to 250 ℃, [61]. Figure 5.10(a) shows that the Ms point is never higher than the temperature for the "no dwell time" condition experiment. In other words, the entire sample was considered to have cooled and quenched to the Ms point after the deposition process was completed, and the cyclic hardness change seen in the condition with dwell time did not occur. Moreover, Figs. 5.10(b) and (c) show that in experiments with non-zero dwell times, the temperature is below the Ms point before initiation of the first deposition track of the third layer. Therefore, the Ms phase change is considered to have occurred during deposition. In other words, the hardness is considered to have changed owing to thermal cycling in the subsequent layers.

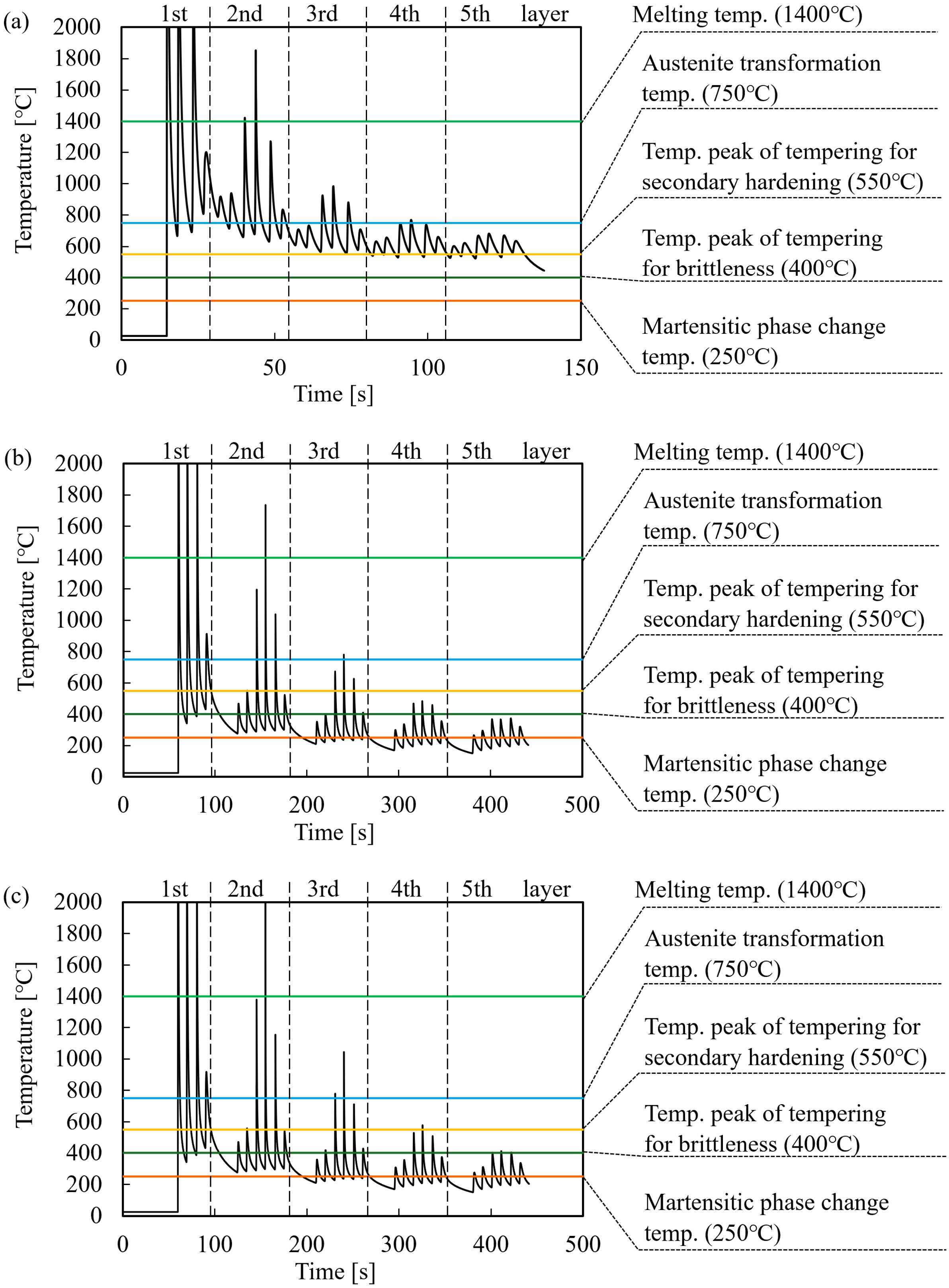

Fig. 5.10 Thermal history simulated by thermal analysis for (a) N1 (0.1 mm height), (b) N5 (0.3 mm height), and (c) N5 (0.6 mm height).

In thermal cycling, remelting of the existing layer is important because the effect of thermal cycling is reset when the material is melted. The bottom position of the melt pool was estimated using the following method. First, the thermal history at each point along the height of the cross-section at the center of the sample was simulated. Thereafter, the points where the peak temperature exceeded 1225 ℃ at the time of heat input were considered melted. Note that 1225 ℃ was used to estimate the bottom position of the melt pool rather than 1400 ℃, which is the actual melting temperature of the material, considering that the analysis had a 12.5% error in the maximum value, as described in Subsection 5.2.2. Figure 5.11 compares the hardness distribution and estimated height of the bottom of the melt pool during the deposition of layers 3, 4, and 5. Here, hardness was measured at intervals of 0.1 mm for a detailed comparison. The melting area is estimated to extend two layers below into deposition layers 3 to 5. The bottom of the melt pool is at a height of 0.9, 1.7, and 2.7 mm in deposition layers 3, 4, and 5, respectively.

Figure 5.11 shows that the hardness decreases below the bottom position of the melt pool estimated by the simulation, that is, in the heat-affected region where tempering takes place at a higher temperature. This suggests that the hardness variation results from thermal effects in the next or subsequent layers. In this case, owing to heat input from the next and subsequent layers, the hardness is found to be high in most melted areas as the layers are cooled and quenched together. However, the hardness in the area 0.2 to 0.3 mm below the remelt is lower owing to tempering at high temperature for a short time, resulting in periodic fluctuations.

To investigate the cause of cracking with and without dwell time, the thermal history near the surface (4.5 mm height) was compared. As shown in Fig. 5.12, in the condition without dwell time, the temperature drops below the Ms point for the first time after deposition is completed, whereas in the condition with dwell time, the temperature drops below the Ms point and then rises to the tempering embrittlement temperature. This thermal history can be considered one of the factors causing cracking, as reported by Li et al. [62].

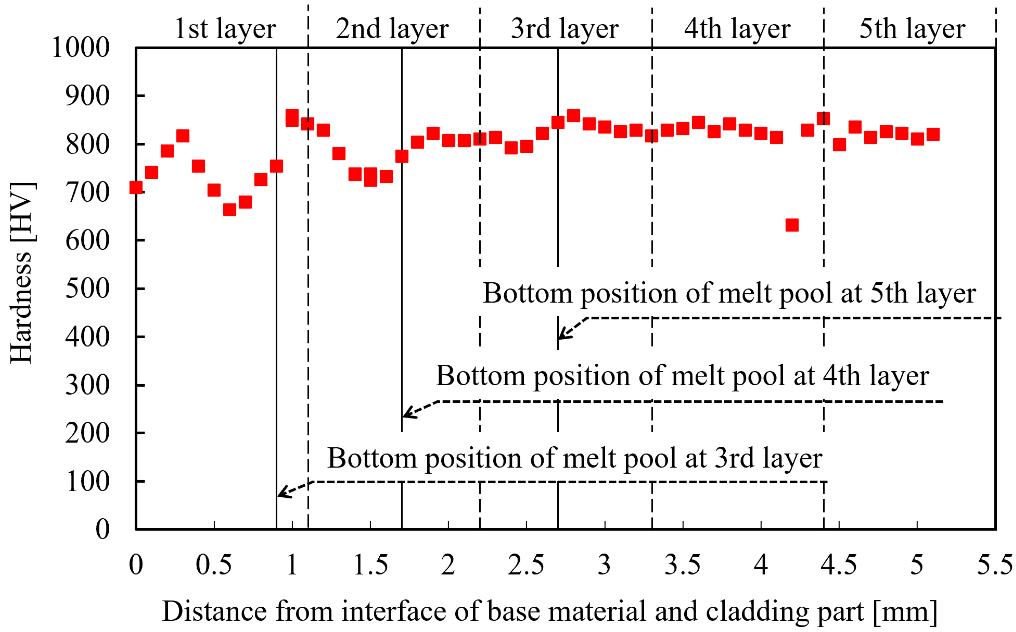

Fig. 5.11 Comparison between the measured hardness and bottom position of the melt pool at each deposition layer estimated by thermal history analysis for N5.

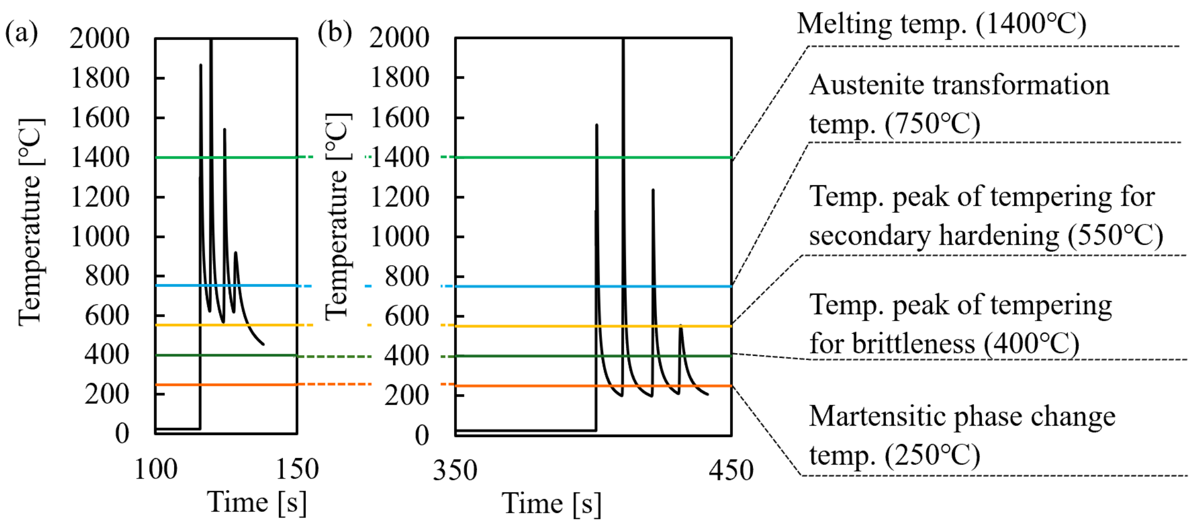

Fig. 5.12 Thermal history simulated by thermal analysis for (a) N1 and (b) N5 (4.5 mm height).

5.6 Summary of Chapter 5

In this chapter, the relationship between the thermal history, cracking, and hardness of M2, a type of high-speed steel, was investigated by performing deposition experiments using DED apparatus with systematically varying interpass dwell times. The following conclusions were obtained.

1) The workpieces deposited without any dwell time exhibited no cracking and a uniform distribution of high hardness. The workpieces with non-zero dwell times demonstrated cracking and hardness variations in both the build and horizontal directions.

2) Costa's suggestion regarding the stainless steel, SUS420, was also valid for M2 [36]. The workpiece temperature should be maintained above the Ms point by continuously applying heat. If the temperature drops below the Ms point even once, temper softening is inevitable in the upper layers. Thus, the interpass dwell time between adjacent lines has a dominant effect on the deposition of three-dimensional shapes.

3) The simplified temperature simulation in this study is effective for the practical analysis of the deposition path strategy because it can predict where temper softening will occur.

6 Case Study

6.1 Introduction

As explained in Section 2.6, the demands for high hardness, crack-free coatings, especially as an alternative to hard chromium plating, are increasing because of environmental issues and carbon dioxide emissions. The surface hardness of chromium plating has a high Rockwell hardness (HRC) value of 65 to 68 and is used for sliding parts that require high hardness.

In this thesis, Chapters 3, 4, and 5 investigated the development of practical high hardness coatings by DED to provide a solution for the above demands. In this chapter, a case study will be presented based on the findings of the preceding three chapters.

The organization of this chapter is as follows. Section 6.2 describes the target workpiece of the case study and requirements for practical use. Section 6.3 reviews the findings of the preceding three chapters and explains the predications for successful hard coating fabrication by DED in terms of thermal history and deposition conditions. Section 6.4 describes the experimental setup and method for validating the predictions. Section 6.5 evaluates the quality of the workpiece deposited in the experiment. Section 6.6 evaluates the influence of the proposed application on the environment. Finally, conclusions of this chapter are outlined in Section 6.7.

6.2 Target Workpiece and its Application

The drawbar is the targeted workpiece for the case study. Figure 6.1 shows the appearance of a drawbar and disc springs. The drawbar is a core component of the milling spindle of a CNC machine tool and essential for clamping and unclamping the tool holder. As shown in Fig. 6.1, drawbars require a hard surface for wear resistance against the abrasion of disc springs that slide along the drawbar during clamping and unclamping.

To obtain a hard surface, drawbars have conventionally been treated with hard chromium plating in the production processes, resulting in a long lead time. Therefore, fabrication of the drawbar in the conventional process requires multiple specialized machines for cutting, heat treatment, strain removal, chromium plating, and grinding.

If DED is utilized and the processes shortened, the lead time can be dramatically shortened and the environmental issues associated with hard chromium plating may be resolved. Hence, the draw bar is a suitable workpiece to realize process integration with the hybrid DED machine described in Chapter 2.

The alternative to hard chromium plating must have a high hardness exceeding HRC 65 on the surface of a drawer. The Co-based super alloy Stellite cannot achieve HRC 65, while the high-speed steel M2 may possibly achieve HRC 65. Therefore, M2 was selected as the deposited material.

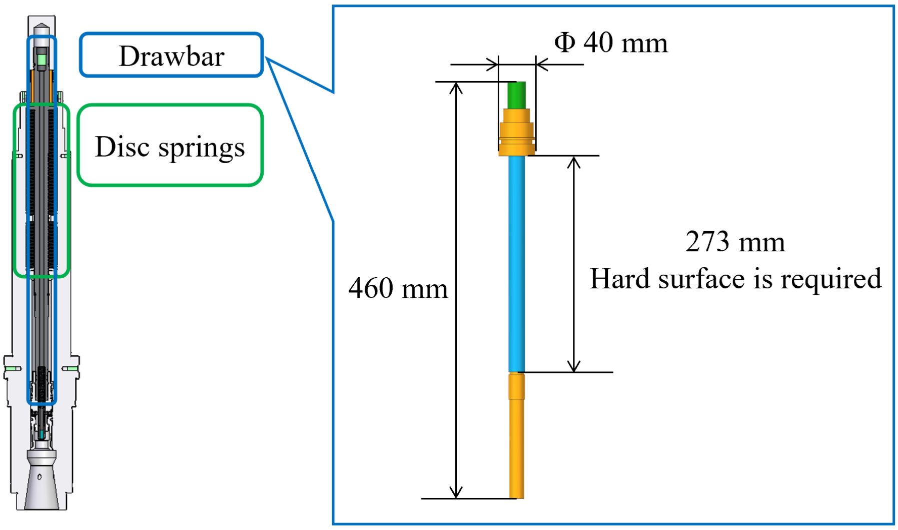

Fig. 6.1 Appearance of a drawbar and disc springs.

6.3 Deposition Strategy

To obtain the required hardness, the factors to be considered are whether dwell time is required, how long the dwell time should be if required, and what type of thermal history is required. Therefore, this section discusses the thermal history simulation performed to predict the methods for achieving HRC 65 with no cracks and the selected deposition conditions.

6.3.1 Thermal History Simulation

The model of the drawbar used for the thermal simulation is shown in Fig. 6.2. As shown in the figure, the portion to be deposited had a pipe shape with an outer diameter of 18.3 mm, inner diameter of 6 mm, and length of 237 mm. The thickness of the cladding was 0.6 to 0.7 mm, similar to that of chrome-plating in the conventional process.

The deposition path is shown in Fig. 6.2. To move the laser nozzle continuously and perform deposition efficiently, the movement of the nozzle in the axial direction of the drawbar was synchronized with the rotation of the drawbar. The movement distance per rotation, which was equivalent to the interval of deposition lines, was set to 1.8 mm.

As described in Section 2.6 and Chapter 5, maintaining the deposited workpiece temperate above the Ms point during the deposition process is important to prevent temper softening. The relative feed rate to the surface to be deposited should be high to ensure subsequent lines are deposited before the pre-deposited line has cooled. In addition, high laser power is preferrable to prevent cracking and ensure the base material and supplied powder are adequately melted, as discussed in Chapter 4. The deposition parameters listed in Table 6.1. for this case study were selected based on these findings.

Interpass dwell time is defined as the time interval between the depositions of one rotation and the next. In this study, interpass dwell times of 0 and 6 s were selected, and thermal simulation was performed to estimate the thermal history of the deposited workpiece and investigate the influence of dwell time on the thermal history.

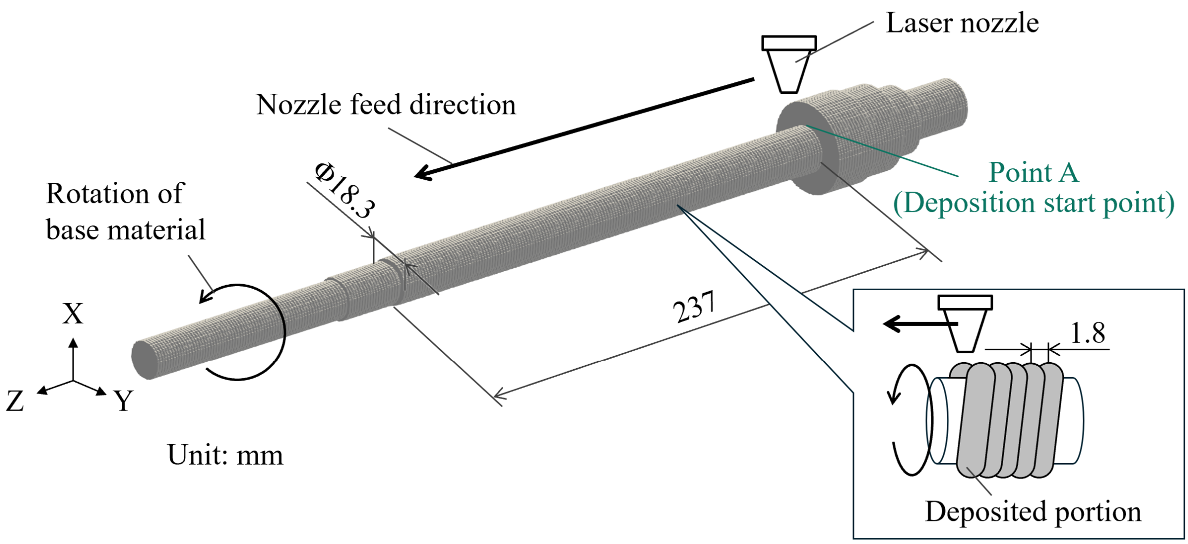

Fig. 6.2 Schematic of DED cladding on a drawbar.

Table 6.1 Deposition parameters and conditions used in the thermal simulation of the DED coating on the drawbar.

Workpiece No.	B1	B2
Laser power [W]	1600	
Relative feed rate to surface to be deposited [mm/min]	5000	
Rotation speed of base material [min^{-1}]	87	
Nozzle feed rate [mm/min]	157	
Powder feed [g/min]	35	
Interpass dwell time [s]	0	6

The results of the thermal history analysis at the start of deposition are shown in Fig. 6.3. The zero dwell time result is shown in Fig. 6.3(a), and 6 s dwell time result is shown in Fig. 6.3(b). In the case of zero dwell time, the thermal history was calculated from the start of deposition to air cooling until 120 s after the end of deposition. In the case of a dwell time of 6 s, the thermal history was calculated from the start to the end of deposition. The results of Chapter 5 indicate that to maintain high hardness, the temperature must not fall below 250 ℃, that is, the martensitic transformation temperature, even once during deposition, and that the deposited workpiece will be cooled and transformed only after deposition has ended. As shown in the thermal analysis in Fig. 6.3(b), when the dwell time is set to 6 s, the temperature cools to approximately 100 ℃ after each rotation of the drawbar. Therefore, the hardness of the deposited material can be inferred to decrease because of reheating after martensitic transformation, with thermal history preventing uniform martensitization. This hardness decrease may be equivalent to that in the first layer of N5, described in Chapter 5. On the other hand, looking at the result of Fig. 6.3(a) with zero dwell time, the subsequent layer is deposited before the layer has cooled as per the deposition conditions selected. Thus, the temperature drop is suppressed to 260 ℃. In addition, over time the deposition points move away from the starting point and the temperature drops to 250 ℃, which is the martensitic transformation temperature. This is similar to the thermal history of N1 in Chapter 5. The decrease in hardness is thought not to result from temper softening under the heat-affected region, and the deposited portion is uniformly martensitized and shows high hardness.

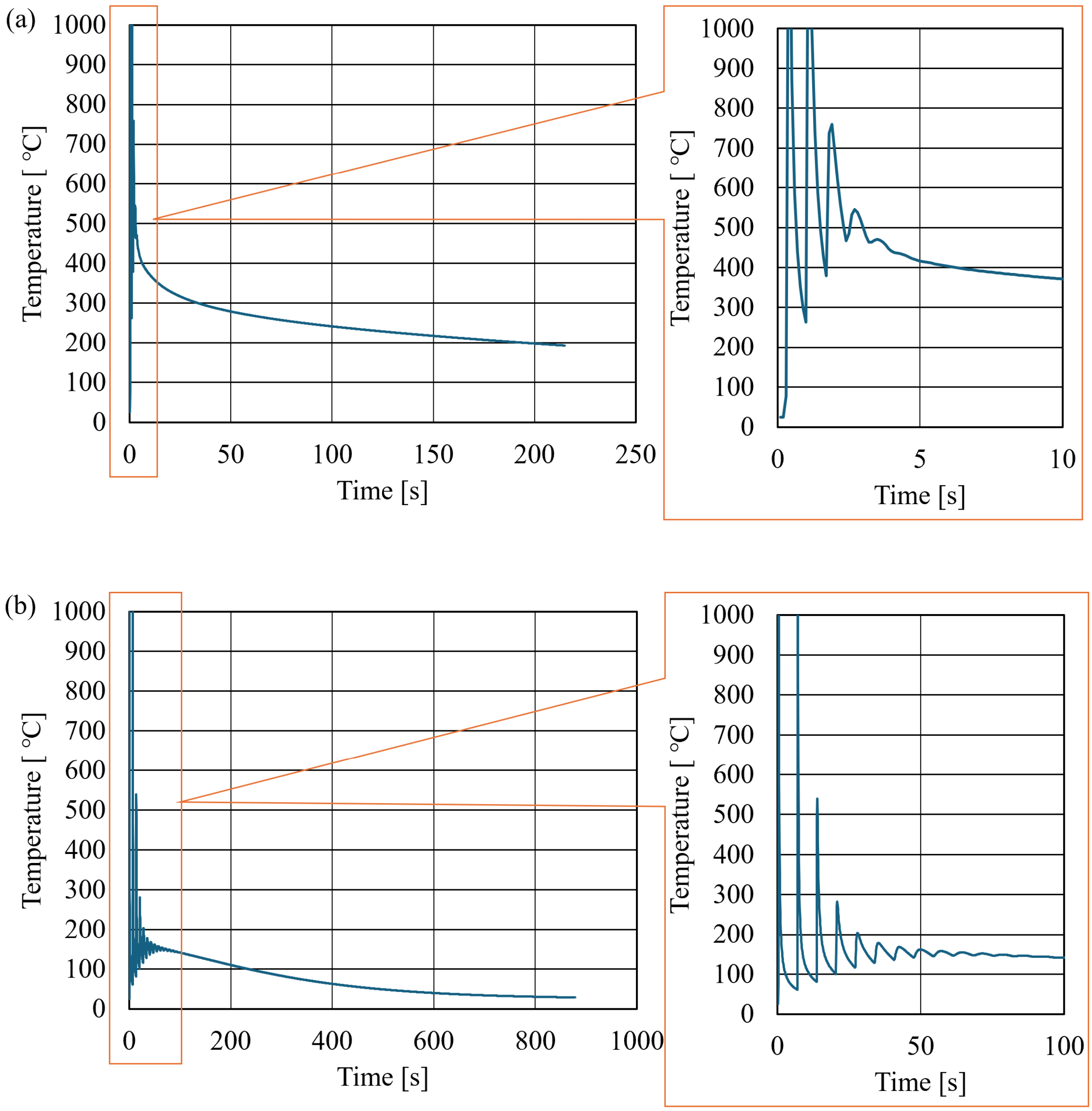

Fig. 6.3 Thermal history of Point A (shown in Fig. 6.2) estimated by thermal simulation for dwell times of (a) 0 and (b) 6 s.

6.3.2 Selected Experimental Conditions

Based on the simulation results of the previous subsection and the findings of Chapters 3, 4, and 5, the deposition parameters and conditions listed in Table 6.2 were selected for the deposition experiment, which will be described in the next section. This hypothesis, if correct, will be evaluated in Section 6.5

Table 6.2 Deposition parameters and conditions for the deposition experiment.

Laser power [W]	2500
Feed rate [mm/min]	5000
Powder feed [g/min]	35
Interpass dwell time [s]	0

6.4 Experimental Setup and Method

6.4.1 Experimental Setup and Materials

Figure 6.4 shows the experimental setup. The hybrid DED machine, LASERTEC 3000 DED hybrid (DMG MORI, Japan), was used. The machine is a hybrid machine based on a turn-mill machine, with 5-axis control, 3 linear axes, 1 inclined axis on the tool side, and rotation axis on the workpiece side. Milling was conducted by clamping the milling tool to the tool spindle, and turning machining was conducted by clamping the turning tool and rotating the workpiece at high speed. Furthermore, clamping allowed laser head deposition to be performed. Fully automatic mounting of the laser head to the tool spindle enabled machining with a single chucking operation. The maximum deposited workpiece size was ⌀400 mm × 1,321 mm when the AM head was vertically oriented downward and ⌀670 mm × 932 mm when the AM head was horizontally oriented. In contrast to the large deposition size of the LASERTEC 3000 DED hybrid, its footprint is rather compact at 6,876 mm × 4,510 mm, and the machine height is only 2,750 mm.

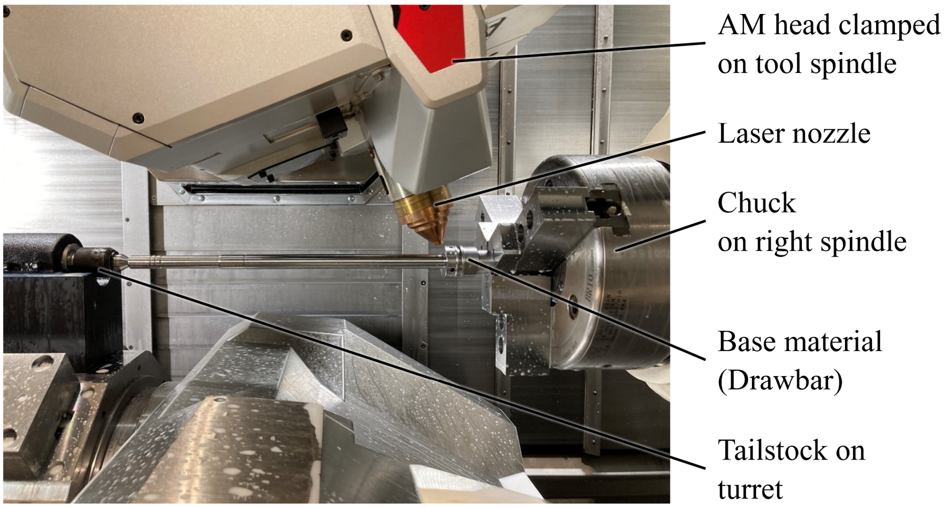

Fig. 6.4 Experimental setup for the DED coating on the drawbar using the LASERTEC 3000 DED hybrid machine.

6.4.2 Experimental Method

The drawbar was clamped to the turning spindle of the LASERTEC 3000 DED hybrid and coated with high-speed steel where it had previously hardened and been chrome-plated. The coating process took approximately 2 min, which is an incredibly short time. In addition to the chrome-plating process, the coating was applied to a material that had not been quenched to omit the quenching process.

The portion of the drawbar to be coated by DED was the same as that in the thermal simulation, as shown in Fig. 6.2. Figure 6.4 shows a photo captured during the experiment.

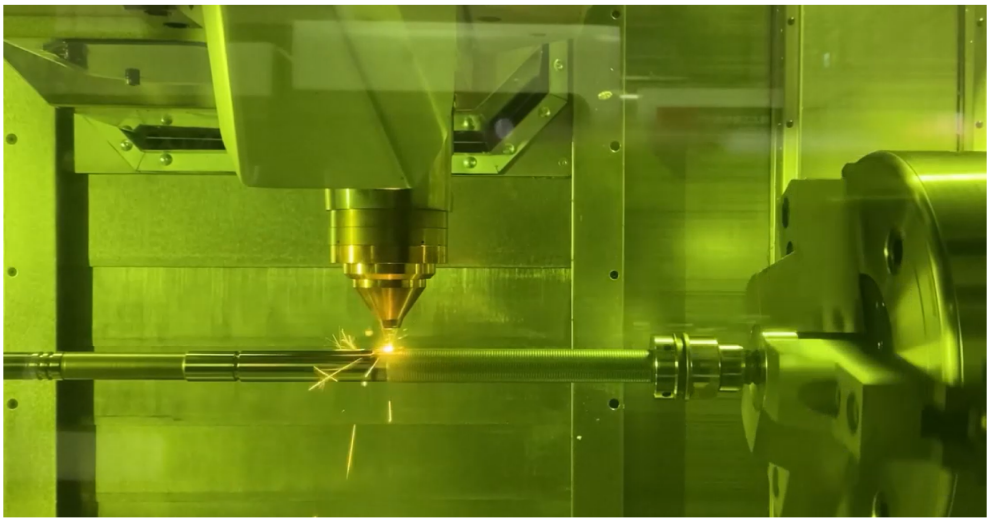

Fig. 6.4 View of the high-speed steel coating of the drawbar.

6.4.3 Evaluation Method

After deposition, a hardness measurement was performed. The deposited workpiece was sectioned with a grinding disc, and the cross-section was polished. Hardness was measured at 0.1 mm intervals in the build direction, and the maximum value was taken to be the hardness of DED coating. The measuring instrument used was an AAV500 micro-Vickers hardness tester (Mitsutoyo, Japan).

The internal defects were also evaluated by X-ray CT scan using a METROTOM 1500 G3 (Carl Zeiss, Germany). Figure 6.5 shows the measurement portion of the drawbar. Measurements were taken every 10 mm with the end face of the deposited portion designated as Z0. The voxel size was approximately 50 μm and could detect defects as small as 50 μm. Figure 6.6 shows an image of the detected defects.

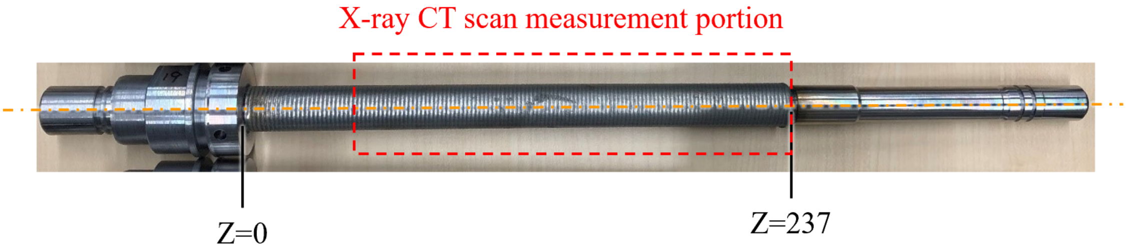

Fig. 6.5 Measurement portion of the X-ray CT scan of the drawbar.

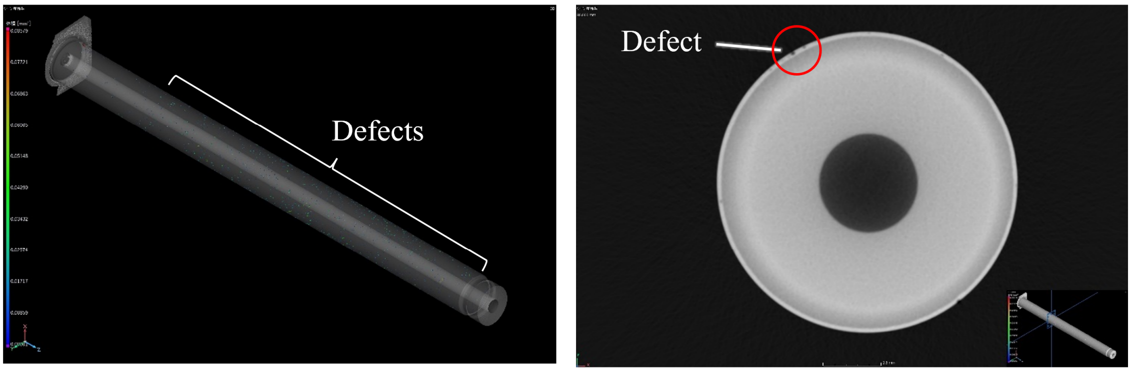

Fig. 6.6 Example image of the X-ray CT scan where defects were detected.

Finally, to evaluate the endurance of the drawbar section coated with high-speed steel by DED, tests were conducted by sliding disc springs on the sliding portion of the drawbar to simulate the actual usage environment. Up to 5 million cycles were conducted, which is the target value for endurance testing, and two drawbars were compared and evaluated. One drawbar was made of carburized and hardened SCM material with chrome-plating, which is the currently available product. The other was made of an S45C base material with high-speed steel M2 coated on the surface by DED to reduce material costs. After testing, the outer diameter of the sliding surface was measured, and the change from the original value was calculated, representing the amount of wear, to evaluate the wear resistance. The wear condition of the disc springs was also observed under a microscope, and the effect of wear on the mating material was evaluated. The durability of the materials was evaluated by three-dimensional measurement.

6.5 Experimental Results

6.5.1 Hardness Measurement Result

Figure 6.7 shows the hardness measurement result. As shown in the figure, the hard values were 0.1 to 0.3 mm from the surface. The maximum hardness of HV 845 (equivalent to HRC 65.5) was 0.1 mm. The base material, S50C, was confirmed as having also increased to HV 600, which is assumed to be a result of the temperature increase to the quenched temperature during deposition.

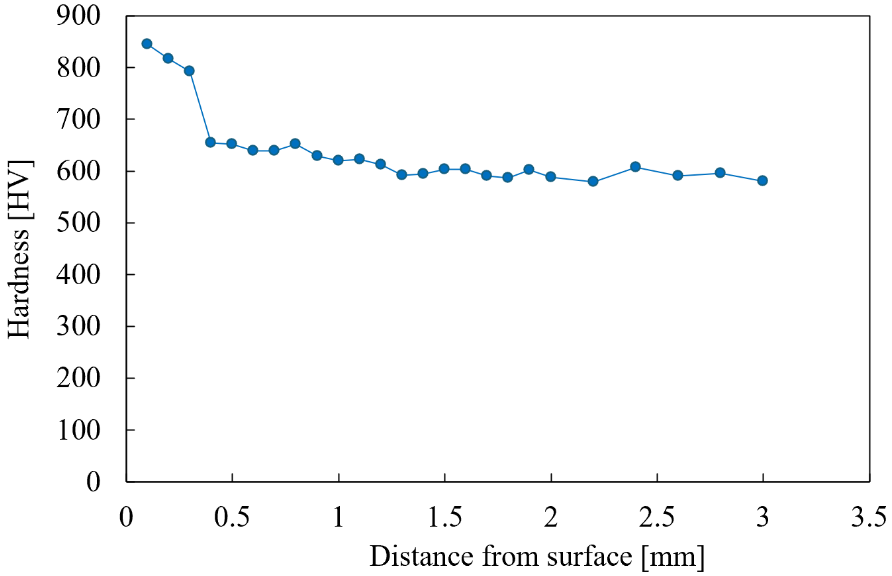

Fig. 6.7 Hardness measurement result of the drawbar coating by DED.

6.5.2 Crack Development Evaluation

Before the endurance test, as in Subsection 6.5.1, the cross-section was polished after cutting and then observed under a microscope. The cut was made at a point 100 mm from the end face of the deposition start point. As shown in Fig. 6.8, no large defects of 50 μm are observed on the coated high-speed steel.

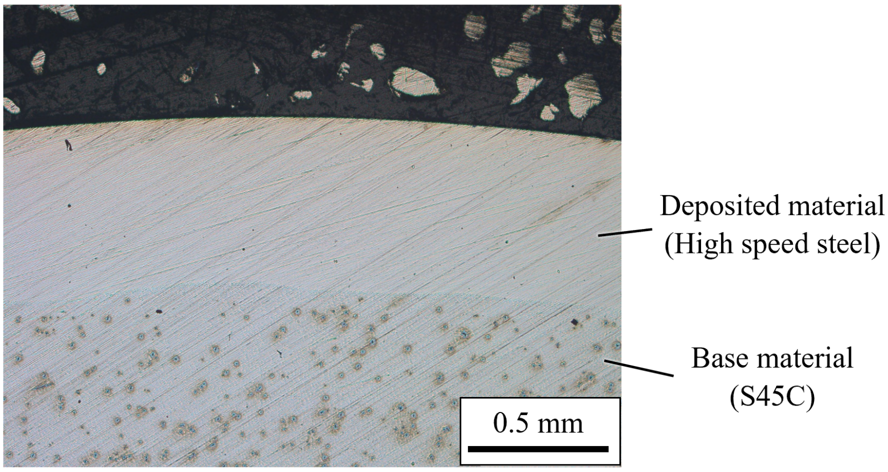

Fig. 6.8 Cross-section of the drawbar cladding by DED.

The specimens were also color-checked after cutting to evaluate crack existence. The evaluation method is shown in Fig. 6.9 as per the standard in JIS Z2343-1:2017 [63]. The method is described as follows. (1) A penetrant application of red paint is applied to the deposited workpiece and penetrates surface discontinuities such as scratches, cracks, and voids. (2) A developer application is applied to bring out the red color of the penetrant application. (3) If the workpiece has any scratches or cracks, the penetrant application that permeated the material will show these as red markings.

As shown in Fig. 6.9, no red flaws are observed on the workpiece, indicating that no defects or cracks developed in the deposited high-speed steel, M2.

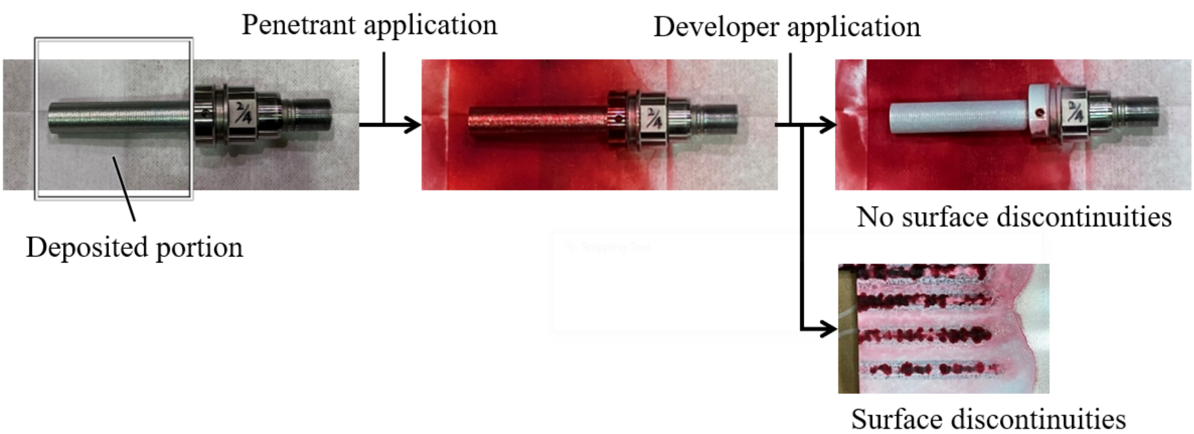

Fig. 6.9 Color-check procedures and result for the drawbar cladding by DED.

Figure 6.10 shows a cross-section view of the X-ray CT imaging result. This result was obtained after 5 million cycles of endurance testing. Internal defects and cracks not visible with the naked eye were revealed during the endurance test. The cross-sections at Z = 20 and Z = 190, in which sliding marks were particularly visible, are shown as representatives of the result. Voids, as shown in Fig. 6.6, were not found in the coating area, indicating that no internal defects formed during the endurance test.

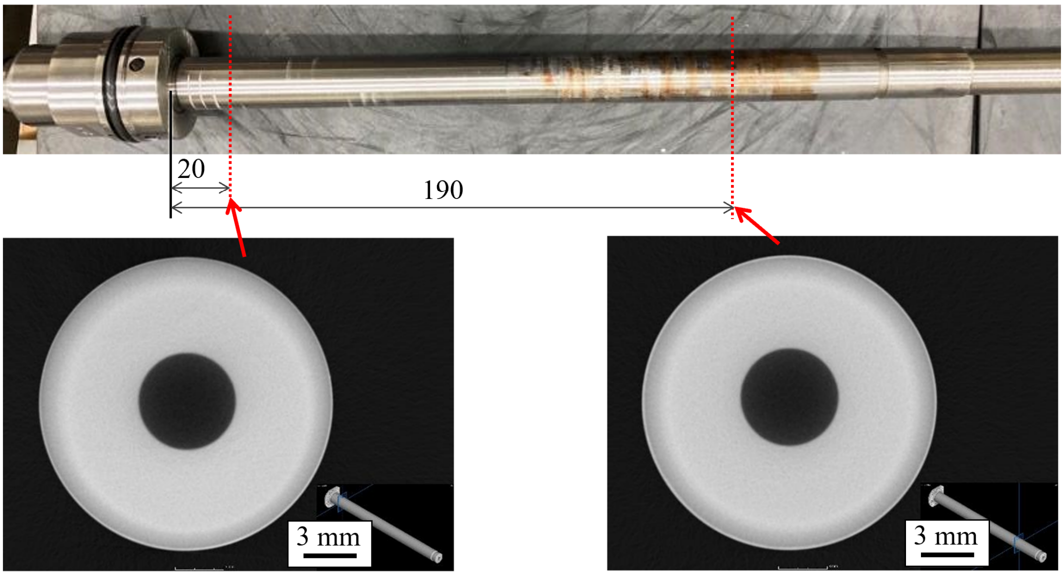

Fig 6.10 Internal crack evaluation by X-ray CT scan.

6.5.3 Evaluation of Wear Resistance

Figure 6.11 shows the results of the wear resistance evaluation. Figure 6.12 shows photos of the drawbar at each sliding time. These figures reveal that the amount of wear on the drawbar sliding surface coated by DED was as low as that of the currently available product.

In addition, because a small coefficient of friction may damage the mating disc springs, which are the sliding part, the amount of wear on the disc springs was also evaluated under a microscope. The amount of wear was found to not differ significantly from that of the disc springs used with the currently available chrome-plated drawbar, suggesting that DED can be used for high-speed steel coating as a replacement process for hard chrome-plating.

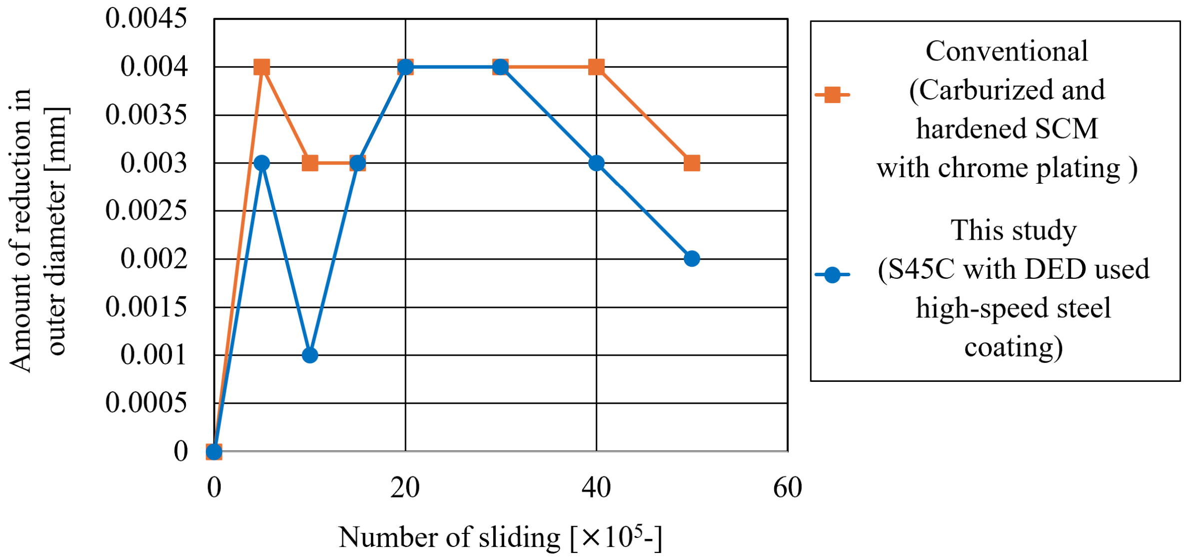

Fig. 6.11 Wear resistance evaluation result for drawbar cladding by DED.

	Conventional (Carburized and hardened SCM with chrome plating)	This study (S45C with DED used high-speed steel coating)
After 0 times sliding	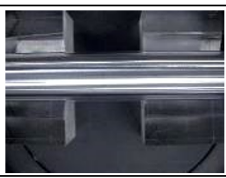 OD: 18.289 mm AW: 0 mm	 OD: 18.289 mm AW: 0 mm
After 5 × 10^5 times Sliding	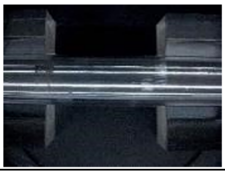 OD: 18.285 mm AW: 0.004 mm	 OD: 18.286 mm AW: 0.003 mm
After 50 × 10^5 times sliding	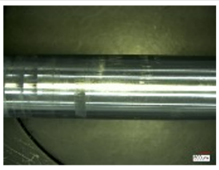 OD: 18.286 mm AW: 0.003 mm	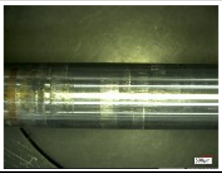 OD: 18.287 mm AW: 0.002 mm

Fig. 6.12 Photos of the drawbar at each sliding time during the endurance test (OD: outer diameter, AW: amount of wear).

6.6 Lead Time and Power Consumption Reductions by Proposed Method

The LASERTEC 3000 DED hybrid machine can produce coatings with a durability equivalent to that of hard chrome-plating, as discussed in Subsection 6.4.3. Because the process can be integrated, the quenching process generally performed before chrome-plating can be omitted. This machine thus makes a strong contribution to energy conservation. Figure 6.13 shows the comparison between the conventional and integration processes for drawbar manufacturing.

The lead time for the conventional sequence, most notably for chrome-plating and transportation to and from the supplier, is 14 d. By contrast, because the surfacing step was conducted by the hybrid machine, every other step could be performed by the hybrid machine as well. Thus, the drawbar manufacturing lead time was not measured in days, but rather took only 2 h.

Regarding environmental impact, accounting for carbon dioxide emissions revealed gains that were nearly as advantageous. In the currently available process, chrome-plating is the step with by far the largest power consumption. Stress relieving and induction heating are second and third. By eliminating these three steps, the power consumption to fabricate each drawbar was reduced from 299.7 to 98.8 kWh. For the Chubu Electric Power plant that serves the Iga production site, DMG MORI says this translates to a drop of 76.7 kg in carbon dioxide emitted per drawbar.

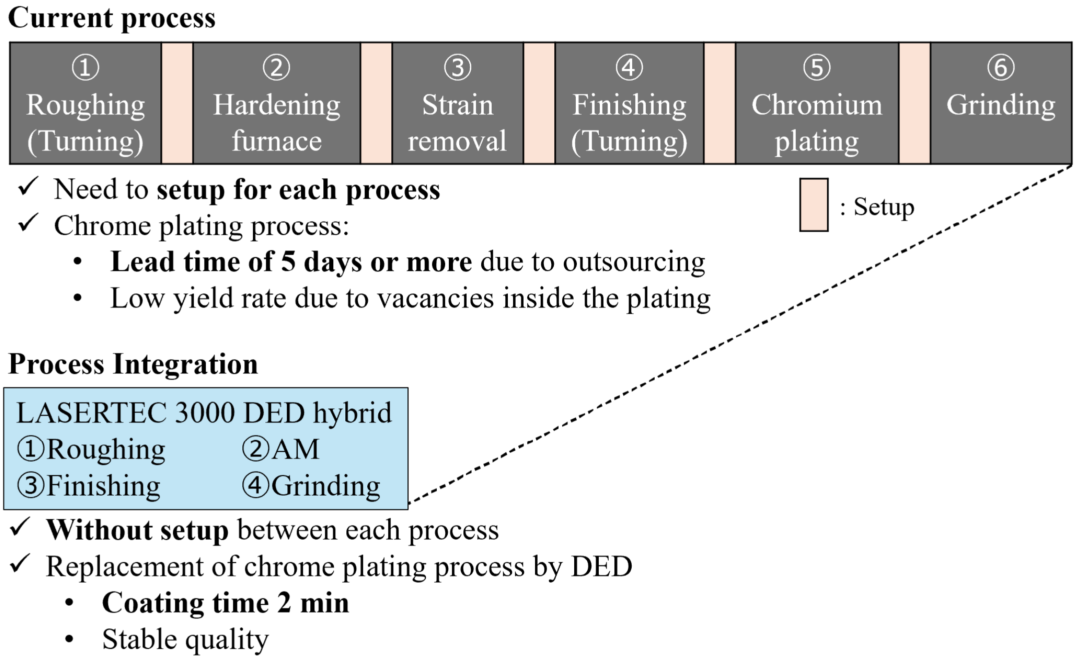

Fig. 6.13 Conventional and integration processes for drawbar manufacturing.

6.7 Summary of Chapter 6

In this chapter, the case study was presented based on the findings of Chapters 3 to 5. A drawbar, which is a key component of the spindle unit, was selected, and deposition conditions were selected based on the thermal simulation. Thereafter, the actual deposition experiment was performed, and the quality of the deposited workpiece was evaluated. The findings of this chapter regarding DED for hard coating are summarized as follows.

1) Thermal simulations were performed and showed that the workpiece temperature could be maintained above Ms during deposition with zero dwell time, whereas the temperature drops with a dwell time of 6 s. Thus, the zero dwell time condition was selected for the deposition experiment.

2) After conducting the deposition experiment, the quality of the deposited workpiece was evaluated. A high hardness of HRC 65.5 was obtained with no cracks. Furthermore, the amount of wear after the endurance test was equivalent to that of conventional products.

3) From the viewpoint of the environmental impact, in contrast to conventional chrome-plating, DED cladding and its integration into a subtractive machine tool make a strong contribution to energy conservation. In this case study, the lead time reduction was estimated to be almost 14 d, and the powder consumption could be reduced by approximately one-third.

7 Conclusions and Future Work

This thesis aimed to use DED to fabricate hard, crack-free coatings for practical application in industrial fields by focusing on high-speed steel and Stellite as the applicable materials. The influence of the cooling rate and thermal history on hardness and crack development was investigated mechanically through a combination of numerical and experimental techniques. The achieved results are summarized as follows.

1) For the deposition of a thin-wall-shaped workpiece using SUS316L, the cooling rate for solidification ranged from 3×10^3 to 10×10^3 K/s and the hardness ranged from 160 to 220 HV. A correlation was found between the cooling rate and hardness in the melting and solidification regions. Furthermore, the cooling rate was not significantly affected by the dwell time, which is a deposition condition that can be changed in practical applications.

2) For the cladding of Stellite, a sufficient hardness of 642.3 HV was obtained when the preheating temperature was 500 ℃ and the laser power was 1750 W. A trade-off between high hardness and low crack frequency was apparent. The composition analysis clarified that this trade-off was influenced by the amount of precipitated chromium carbides, which are hard and brittle materials. The amount of embrittlement chromium phase should be approximately 40% or less to ensure hard, crack-free deposition.

3) In the cladding of M2, which is a high-speed steel, a simple temperature simulation was developed and used to determine the deposition conditions under which the deposition temperature can be maintained above Ms by continuously applying heat. The deposition experiments showed that uniform and high hardness was achieved under the obtained deposition conditions. The results show that the simple temperature simulation developed is effective for predicting where heat-induced softening will occur in a practical time frame and for designing deposition strategies to avoid heat-induced softening.

4) A case study was conducted on drawbars to verify the applicability of the obtained knowledge for the production of actual parts. The workpiece deposited under the obtained deposition conditions had a hardness of HRC 65.5 and met the required specifications. The results show a practical example of high hardness material cladding by DED rather than conventional hard chrome-plating.

Future work should address the following.

1) In the case study, the laser power and nozzle feed rate were determined based on beads shape and porosity, and dwell time was selected from a simple temperature simulation. Whether this deposition strategy can be used in other practical cases should be verified.

2) The dwell time was selected to achieve the desired thermal history. In addition, the preheating temperature should be determined.

3) For the development of a simple temperature simulation, a balance exists between accuracy and computation time. More accuracy should be achieved in a similar timeframe.

4) In Chapter 5, two factors, hardness variation and crack occurrence, with and without dwell time, are discussed in terms of the thermal history obtained from the simulation. From the temperature history, one can infer that the material is embrittled because the tempering embrittlement temperature is exceeded after the temperature drops below the Ms point. Confirmation of this finding must be obtained through actual observation of the microstructure. The creation of a database of standard specimens would be beneficial to more precisely and effectively investigate the relationship between temperature history and microstructure. For example, while measuring temperatures with a thermal camera, heat treatment can be performed using only one line of stacking and a laser. The relationship between heat treatment and the hardness and microstructure should be added to the database to allow comparisons with actual workpieces in the actual process.

5) Fracture toughness and residual stress should be evaluated as a measure of crack resistance.

Acknowledgement

First, I would like to express my deepest gratitude to my supervisor Professor Atsushi Matsubara and Associate Professor Daisuke Kono for the continuous support and exceptional guidance throughout this rewarding research work. I would not have finished my PhD without their valuable advice.

My deep gratitude also goes to my thesis committee, Professor Kazuhiro Izui and Professor Hiroyuki Hirakata at Kyoto University for reviewing the dissertation and providing me with helpful suggestions and comments to improve the quality of my thesis.

I am grateful to Dr. Masahiko Mori and Dr. Fujishima from DMG MORI CO., Ltd. for offering me the great opportunity to proceed my research.

I express my sincere thanks to Professor Emeritus Tojiro Aoyama, Professor Emeritus Hideki Aoyama, Professor Tetsuya Suzuki, Professor Yasuhiro Kakinuma, and Associate Professor Ryo Koike for their helpful discussions.

I would also like to acknowledge the kind support from Dr. Takanori Mori, Dr. Masahiro Ueda, Dr. Hiroyuki Kawakami, Dr. Shogo Sugimoto, and Mr. Yuichiro Miyata from DMG MORI. I would not have been able to complete my study without their help and discussions during my PhD course. My warmest regard goes to all members of DMG MORI for their help and cooperation.

Last but not least, my gratitude goes to my beloved husband Yusuke Yamamoto for his loving encouragement and support.

2024

Yoko Hirono

Reference

[1] C. W. Hull, "Apparatus for production of three-dimensional objects by stereo lithography," United States Patent US 4575330, 1986.

[2] M. Munsch, M. Schmidt-Lehr, E. Wycisk, T. Führer, F. AI-Shwwa, F. Beckmann, B. Bernard, N. Bunt, A. K. R. Crylls, J. Kowen, L. Neumann, F. Sant’Ana, C. M. Seidel and K. Wang, "AMPOWER REPORT 2022 – Additive manufacturing market report," AMPOWER GmbH & Co. KG, 2022.

[3] M. Thompson, G. Moroni, T. Vaneker, G. Fadel, R. Campbel, I. Gibson, A. Bernard, J. Schulz, P. Graf, B. Ahuja and F. Martina, "Design for additive manufacturing: Trends, opportunities, considerations, and constraints," CIRP Ann.—Manuf. Techn., vol. 65, pp. 737–760, 2016.

[4] S. Tofail, E. Koumoulos, A. Bandyopadhyay, S. Bose, L. O’Donoghue and C. Charitidis, "Additive manufacturing: scientific and technological challenges, market uptake and opportunities," Mater. today, vol. 21, no. 1, pp. 22–37, 2018.

[5] B. Blakey-Milner, P. Gradl, G. Snedden, M. Brooks, J. Pitot, E. Lopez, M. Leary, F. Berto and A. d. Plessis, "Metal additive manufacturing in aerospace: A review," Mater. Des., vol. 209, p. 110008, 2021.

[6] V. Madhavadas, D. Srivastava, U. Chadha, S. A. Raj, M. T. H. Sultan, F. S. Shahar and A. U. M. Shah, "A review on metal additive manufacturing for intricately shaped aerospace components," CIRP-JMST, vol. 39, pp. 18–36, 2022.

[7] B. Sarzynski, L. Sniezek and K. Grzelak, "Metal additive manufacturing (MAM) applications in production of vehicle parts and components—A review," Metals, vol. 14, p. 195, 2024.

[8] M. Schmidt, M. Merklein, D. Bourell, D. Dimitrov, T. Hausotte, K. Wegener, L. Overmeyer, F. Vollertsen and G. Levy, "Laser based additive manufacturing in industry and academia," CIRP Ann.—Manuf. Techn., vol. 66, pp. 561–583, 2017.

[9] R. Koike, I. Unotoro, Y. Kakinuma and Y. Oda, "Graded Inconel 625 – SUS316L joint fabricated using directed energy deposition," Int. J. Automation Technol., vol. 13, no. 3, pp. 338–345, 2019.

[10] J. Pragana, R. Sampaio, I. Bragança, C. Silva and P. Martins, "Hybrid metal additive manufacturing A state–of–the-art review," Adv. Ind. Manuf. Eng., vol. 2, p. 100032, 2021.

[11] T. Kuriya, K. R. T. Mori and Y. Kakinuma, "Relationship between solidification time and porosity with directed energy deposition of Inconel 718," J. Adv. Mech. Des. Syst. Manuf., vol. 12, no. 5, pp. 1–11, 2018.

[12] R. Liu, Z. Wang, T. Sparks, F. Liou and J. Newkirk, "13 - Aerospace applications of laser additive manufacturing," in Laser Additive Manufacturing: Materials, Design, Technologies, and Applications, Woodhead Publishing Series in Electronic and Optical Materials, pp. 351–371, 2017.

[13] J. Tuominen, M. Kaubisch, S. Thieme, J. Nakki, S. Nowotny and P. Vuoristo, "Laser strip cladding for large area metal deposition," Addit. Manuf., vol. 27, pp. 208–216, 2019.

[14] S. Cecchel, D. Ferrario, C. Mondini, M. Montani and B. Previtali, "Application of laser metal deposition for a new model of assembled camshaft," J. Mater. Eng. Perform., vol. 28, no. 28, pp. 7756–7767, 2019.

[15] G. Baek, G. Shin, K. Lee and D. Shim, "Mechanical properties of tool steels with high wear resistance via directed energy deposition," Metals, vol. 9, no. 3, p. 9030282, 2019.

[16] M. Zhang, C. Chen, L. Qin, K. Yan, G. Cheng, H. Jing and T. Zou, "Laser additive manufacturing of M2 high-speed steel," Mater. Sci. Technol., vol. 34, no. 1, 2017.

[17] M. Yao, J. Wu and Y. Xie, "Wear, corrosion and cracking resistance of some W- or Mo-containing Stellite hardfacing alloys," Mater. Sci. Eng. A , vol. 407, p. 234–244, 2005.

[18] Z. Smoqi, B. D. Bevans, A. Gaikwad, J. Craig, A. Abul-Haj, B. Roeder, B. Macy, J. E. Shield and P. Rao, "Closed-loop control of meltpool temperature in directed energy deposition," Mater. Des., vol. 215, p. 110508, 2022.

[19] N. U. Rahman, L. Capuano, M. d. Rooij, D. Matthewsa, A. Garcia-Junceda, M. Mekicha, L. Cordova, G. Walmag, M. Sinnaeve and G. Römer, "Laser metal deposition of vanadium-rich high speed steel: Microstructural and high temperature wear characterization," Surf. Coat. Technol., vol. 364, pp. 115–126, 2019.

[20] S. Tekumalla, R. Tosi, X. Tan and M. Seita, "Directed energy deposition and characterization of high -speed steels with high vanadium content," Additive Manufacturing Letters, vol. 2, p. 100029, 2022.

[21] D. Shim, G. Baek and E. Lee, "Effect of substrate preheating by induction heater on direct energy deposition of AISI M4 powder," Mater. Sci. Eng. A, vol. 682, pp. 550–562, 2017.

[22] V. Fallah, M. Alimardani, S. Corbin and A. Khajepour, "Impact of localized surface preheating on the microstructure and crack formation in laser direct deposition of Stellite 1 on AISI 4340 steel," Appl. Surf. Sci., vol. 257, no. 5, pp. 1716–1723, 2010.

[23] J. Bennett, D. Garcia, M. Kendrick, T. Hartman, G. Hyatt, K. Ehmann, F. You and J. Cao, "Repairing automotive dies with directed energy deposition: Industrial application and life cycle analysis," J. Manuf. Sci. Eng., vol. 141, no. 2, p. 021019, 2019.

[24] Y. Umeda, Circular Economy (in Japanese), 2021.

[25] J. Zuback and T. DebRoy, "The hardness of additively manufactured alloys," Mater., vol. 11, p. 11112070, 2018.

[26] S.-H. Li, P. Kumar, S. Chandra and U. Ramamurty, "Directed energy deposition of metals processing microstructures and mechanical properties," Int. Mater. Rev., vol. 68, no. 6, pp. 605–647, 2023.

[27] M. Alimardani, V. Fallah, A. Khajepour and E. Toyserkani, "The effect of localized dynamic surface preheating in laser cladding of Stellite 1," Surf. Coat. Technol., vol. 204, no. 23, pp. 3911–3919, 2010.

[28] S. Zhou, X. Zeng, Q. Hu and Y. Huang, "Analysis of crack behavior for Ni-based WC composite coatings by laser cladding and crack-free realization," Appl. Surf. Sci., vol. 255, no. 5, pp. 1646–1653, 2008.

[29] S. Zhou, X. Dai and X. Zeng, "Effects of processing parameters on structure of Ni-based WC composite coatings during laser induction hybrid rapid cladding," Appl. Surf. Sci., vol. 255, no. 20, pp. 8494–8500, 2009.

[30] B. Bax, R. Rajput, R. Kellet and M. Reisacher, "Systematic evaluation of process parameter maps for laser cladding and directed energy deposition," Addit. Manuf., vol. 21, pp. 487–494, 2018.

[31] O. Lucia, P. Maussion, E. Dede and J. Burdio, "Induction heating technology and its applications: Past developments, current technology, and future challenge," IEEE Trans. Ind. Electron., vol. 61, no. 5, pp. 2509–2520, 2013.

[32] P. Farahmand and R. Kovacevic, "Laser cladding assisted with an induction heater (LCAIH) of Ni–60%WC coating," J. Mat. Proc. Technol., vol. 222, pp. 244–258, 2015.

[33] S. Locs, I. Boiko, A. Leitans and P. Drozdovs, "Experimental study of coaxial laser cladding of tool steel," 16th International Scientific Conference Engineering for Rural Development, Jelgava, 2017.

[34] N. U. Rahman, L. Capuano, A. v. d. Meer, M. d. Rooij, D. Matthews, G. Walmag, M. Sinnaeve, A. Garcia-Junceda, M. Castillo and G. Römer, "Development and characterization of multilayer laser cladded high speed Steels," Addit. Manuf., vol. 24, pp. 76–85, 2018.

[35] R. Fukuyama, N. Nakamura and T. Satsuta, "Removal of internal defects in the LMD overlay layer by laser remelting," J. Jpn. Soc. Precis. Eng., vol. 88, no. 4, pp. 345–351, 2022.

[36] L. Costa, R. Vilar, T. Reti and A. Deus, "Rapid tooling by laser powder deposition: Process simulation using finite element analysis," Acta Materialia, vol. 53, no. 14, pp. 3987–3999, 2005.

[37] M. Farshidianfar, A. Khajepour and A. Gerlich, "Real-time control of microstructure in laser additive manufacturing," Int. J. Adv. Manuf. Tech., vol. 82, pp. 1173–1186, 2016.

[38] M. Farshidianfar, F. Khodabakhshi, A. Khajepour and A. Gerlich, "Closed-loop control of microstructure and mechanical properties in additive manufacturing by directed energy deposition," Mater. Sci. Eng. A, vol. 803, p. 14048, 2021.

[39] A. Emamian, M. Alimardani and A. Khajepour, "Effect of cooling rate and laser process parameters on additive manufactured Fe–Ti–C metal matrix composites microstructure and carbide morphology," J. Manuf. Process., vol. 16, pp. 511–517, 2014.

[40] Y. Huang, M. Ansari, H. Asgari, M. Farshidianfar, D. Sarker, M. Khamesee and E. Toyserkani, "Rapid prediction of real-time thermal characteristics, solidification parameters and microstructure in laser directed energy deposition (powder-fed additive manufacturing)," J. Mater. Process. Technol., vol. 274, p. 116286, 2019.

[41] H. Kim, K.-K. Lee, D.-G. Ahn and H. Lee, "Effects of deposition strategy and preheating temperature on thermal-mechanical characteristics of Inconel 718 super-alloy deposited on AISI 1045 substrate using a DED process," Mater., vol. 14, p. 14071794, 2021.

[42] K. Ren, Y. Chew, J. Fuh, Y. Zhang and G. Bi, "Thermo-mechanical analyses for optimized path planning in laser aided additive manufacturing processes," Mater. Des., vol. 162, pp. 80–93, 2019.

[43] M. Sefidi, R. Israr, J. Buhl and M. Bambach, "Rule-based path identification for direct energy deposition," Procedia Manuf., vol. 47, pp. 1134–1140, 2020.

[44] M. Yokota, Y. Ikeda, R. Koike, T. Maki, K. Takaki, T. Mori, Y. Hirono and Y. Kakinuma, "Tool steel coating on gears by directed energy deposition with heat sink," in Proceedings of the Machining Innovations Conference for Aerospace Industry, 2023.

[45] C. Guévenoux, S. Hallais, A. Charles, E. Charkaluk and A. Constantinescu, "Influence of interlayer dwell time on the microstructure of Inconel 718 laser cladded components," Opt. Laser Technol., vol. 128, p. 106218, 2020.

[46] D. Feron, "Nuclear corrosion science and engineering," in Nuclear Corrosion Science and Engineering, Woodhead Publishing Series in Energy, pp. 31–56, 2012.

[47] C. Kledwig, H. Perfahl, M. Reisacher, F. Brückner, J. Bliedtner and C. Leyens, "Analysis of melt pool characteristics and process parameters using a coaxial monitoring system during directed energy deposition in additive manufacturing," Mater., vol. 12, p. 12020308, 2019.

[48] J. Caniou, "Passive Infrared Detection: Theory and Applications," Dordrecht: Kluwer Academic Publishers, 1999.

[49] Japanese Industrial Standard, Steels – Micrographic determination of the apparent grain size JIS G 0551:2020, 2020.

[50] N. Hirota, F. Yin, T. Inoue and T. Azuma, "Recrystallization and grain growth behavior in severe cold-rolling deformed SUS316L steel under anisothermal annealing condition," ISIJ Int., vol. 48, no. 4, pp. 475–482, 2008.

[51] X. Zhao, Y. Liu, Y. Wang, P. Feng and H. Tang, "Recrystallization and grain growth of 316L stainless steel wires," Metall. Mater. Trans. A, vol. 45A, pp. 3446–3453, 2014.

[52] R. Vilar, "Laser cladding," J. Laser Appl., vol. 11, no. 2, pp. 6–79, 1999.

[53] Y. Huang, "Characterization of dilution action in laser-induction hybrid cladding," Opt. Laser Technol., vol. 43, no. 5, pp. 965–973, 2011.

[54] S. Huang, M. Samandi and M. Brandt, "Abrasive wear performance and microstructure of laser clad WC/Ni layers," Wear, vol. 256, no. 11–12, pp. 1095–1105, 2004.

[55] S. B. C. LTD., "Surface hardening alloy general catalog (online)," [Online]. Available: http://www.sanko-stellite.co.jp/products/pdf/kennametal_catalog.pdf. [Accessed 13 March 2023].

[56] A. Koutsomichalis, M. Vardavoulias, A. Lontos and N. Vaxevanidis, "Tensile and bend behavior of nanostructured HVOF and flame sprayed stellite coatings," MATEC Web of Conf., vol. 188, p. 04015, 2018.

[57] Y. Kato and T. Yashiro, "Plasma powder welding overlay with Co-Cr-Mo-V system alloy powder DAPKV series (in Japanese)," DENKI-SEIKO, vol. 72, no. 3, pp. 195–200 , 2001.

[58] Y. Chen, K. Zhang, J. Huang, S. R. E. Hosseini and Z. Li, "Characterization of heat affected zone liquation cracking in laser additive manufacturing of Inconel 718," Mater. Des., vol. 90, pp. 586–594, 2016.

[59] Z. Yang, Y. Jian, Z. Chen, H. Qi, Z. Huang, G. Huang and J. Xing, "Microstructure, hardness and slurry erosion-wear behaviors of high-speed laser cladding Stellite 6 coatings prepared by the inside-beam powder feeding method," J. Mater. Res. Technol., vol. 19, pp. 2596–2610., 2022.

[60] E. Sobol, "Phase transformations and ablation in laser-treated solids," Hoboken, NJ: A Wiley-Interscience, 1995.

[61] K. Itoh, Y. Hitachi and Y. Matsuda, "The effect of the cooling rate in quenching on the hardness of tempered high-speed tool steels (in Japanese)," DENKI-SEIKO, vol. 53, no. 4, pp. 248–255, 1982.

[62] J. Li, C. Zhang and Y. Liu, "Influence of carbides on the high-temperature tempered martensite embrittlement of martensitic heat-resistant steels," Mater. Sci. Eng. A, vol. 670, no. 18, pp. 256–263, 2016.

[63] J. I. Standard, Non-destructive testing-Penetrant testing- Part 1: General principles-Method for liquid penetrant testing and classification of the penetrant indication JIS Z 2343:2017, 2017.

Supplementary Materials

1. Articles in periodicals (related to the thesis)

[1] Y. Hirono, T. Mori, M. Ueda, and D. Kono, Cracking suppression by substrate preheating using an induction heater in directed energy deposition, Journal of Advanced Mechanical Design, Systems and Manufacturing, Vol.17, No 3, (2023), pp.1-15.

[2] Y. Hirono, T. Mori, S. Sugimoto, and Y. Miyata, Investigation on influence of thermal history on quality of workpiece created by directed energy deposition, CIRP Annals, Available online 7 May 2024, In Press, Corrected Proof.

[3] Y. Hirono, T. Mori, H. Kawakami, M. Ueda, and D. Kono, Investigation of Effect of Cooling Rate on Mechanical Properties in Directed Energy Deposition, Int. J. Automation Technol., Vol.19, No.1, (2025).

2. Articles in international conference proceedings (reviewed full-length articles)

[4] Y. Hirono, T. Mori, and D. Kono, Cracking suppression by substrate preheating using an induction heater in directed energy deposition, The 10th International Conference on Leading Edge Manufacturing in 21st Century (LEM21), Kitakyushu, Japan, 2021.

[5] Y. Hirono, T. Mori, H. Kawakami, and D. Kono, An investigation of the effect of cooling rate on mechanical properties in directed energy deposition, Proceedings of the 19th International Conference on Precision Engineering (ICPE 2022), Nara, Japan, 2022.

3. Articles in domestic conference proceedings (reviewed full-length articles)

[6] Y. Hirono, T. Mori, M. Ueda, H. Kawakami, Y. Miyata, S. Sugimoto, and D. Kono, Investigation on influence of thermal history on quality of workpiece created by directed energy deposition, Proceedings of Japan Society for Precision Engineering Spring Conference, Tokyo, Japan, 2024.

Appendix

A.1 Additive Manufacturing (AM)

The AM industry has developed remarkably since the first patent rights were granted in 1986 [1]. The entire metal and polymer AM market size in 2021 was valued at EUR 8.33 billion [1], [2]. AM processes are divided into seven categories, as defined by the American Society for Testing and Materials (ASTM) International Committee F42 [A1]. The substantial growth in AM technology has partly been driven by commercial and performance benefits in the aerospace industry [5], [6]. However, AM is not only increasing in aerospace fields, but also in vehicular fields, [7]. People's interests have shifted from rapid prototyping for the purpose of accelerating development to functional prototyping to developing new technologies [4].

In recent years, metal AM has been expanding into several industrial fields because of the various opportunities in terms of improved flexibility of design and manufacturing and improved productivity. AM has spread to various industries, introducing new capabilities. In addition, simulations enhance the metal AM optimization process, as well as a potential modeling workflow for process optimization [A2].

Papers have reviewed the published data on the mechanical properties of AM metallic materials because more and more industries are trying to utilize metal AM in practical industrial applications [A3]. Several papers focused on sustainability assessment studies of metal AM from a life cycle perspective [A4]. However, as-built components still face various issues to dimension accuracy, surface quality, and mechanical properties such as internal defects. Process monitoring and control are considered for achieving high-quality parts [A5]. A new type of hybridization combining AM with traditional manufacturing processes has emerged [10]. The demands for practical application have been brought into existence by these studies.

Metal hybrid laser additive manufacturing (LAM) technology includes multi-process hybrid laser AM, additive-subtractive hybrid manufacturing, multi-energy hybrid AM, and multi-material hybrid AM [A6]. Laser is mainly used for metal AM, popular LAM techniques such as selective laser sintering/melting, laser directed energy deposition, and laser direct writing [A7]. One of the criterions that distinguishes different AM processes is the deposition method. Metal AM processes can be divided into four classes: local melting, sintering, sheet forming, and electrochemical methods [A8]. Metal AM can also be divided according to the type of material used. One of the most used materials is powder. In powder-based AM, powder is bonded together to create solid functional parts [A9].

Figure A.1.2 shows the global metal and polymer AM market trends and forecasts [A10]. As shown in Fig. A.1.2, the metal and polymer AM market had a compound annual growth rate (CAGR) of 15.3% between 2020 and 2022. In 2023, the market size reached EUR 10.50 billion, representing a CAGR of 10.3% from 2022. In addition, a CAGR of 13.9% by 2028 is predicted, and the total market is expected to generate a revenue of EUR 20.20 billion by 2028.

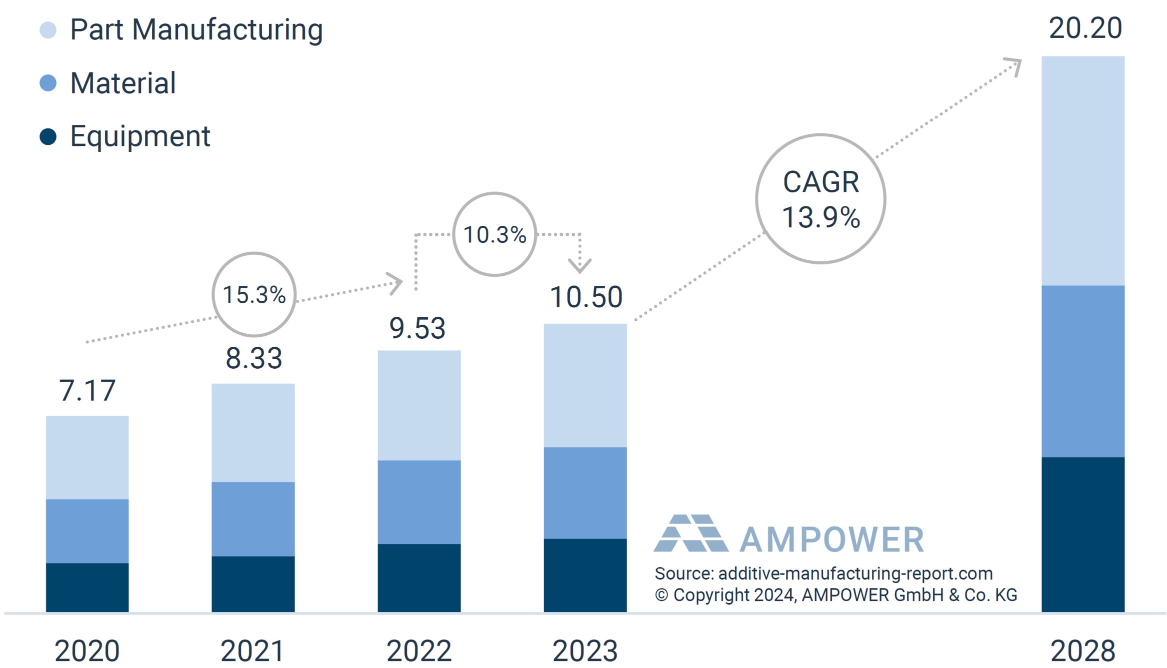

Fig.A.1.2 Global metal and polymer AM market from 2020 to 2023 and forecast to 2028 [EUR billion] (AMPOWER REPORT 2024 Management Summary).

Powder bed fusion (PBF) is highly compatible with topology optimization and other benefits such as the ability to integrate internal piping. Therefore, it is not hard to imagine applications increasing more and more in the future. However, designing to take full advantage of AM is a challenge that is tackled by the discipline ‘Design for AM’. Changing existing designs is a big job. However, with DED, often changes to the geometry of the product are not required. The adoption of DED has led to the consensus that DED is cheaper, produces less waste, and reduces energy consumption, that is, CO_2 emissions, with little or no changes to the overall manufacturing process. This low adoption hurdle has led to the market expectation the CARG of DED will be the highest among various AMs. Carbon neutrality and the circular economy are new and driving forces within today’s industry landscape according to the 2021 White Paper on Environment, Circular Society, and Biodiversity [A11].

The Paris Agreement has triggered a global trend among corporations and financial institutions to incorporate decarbonization into corporate management (decarbon management), coupled with the environmental, social and governance finance movement. Professor Umeda, a senior researcher at the 21st Century Policy Research Institute, cites the transformation of the way in which manufacturing is done and life cycle thinking in product design as possible future events in the idea of circular economy in his book ‘Circular economy’ [24]. DED, as a manufacturing method that will lead to these major goals, is truly attracting attention today. Optimizing carbon emissions in DED manufacturing has gained significant attention [A12]. Life cycle assessment is a valuable tool for determining environmental impacts and comparing systems [A13].

In particular, DED has achieved high adoption within in the aerospace industry [11], [12]. High deposition rate laser directed energy deposition technology has been investigated by many researchers in an attempt to fulfil the requirements of rapid and near-net manufacturing for large-scale and high-performance components [A14]. Characteristics of the primary defects in DED processed materials and their characterization techniques have been reported [A15]. The stepover of adjacent deposition beads is also important to minimize voids in the parts produced by the DED process [A16]. DED is known for the fabrication of high-value metallic alloys in addition to the exploration of multi-material composites and components [A17]. The comparison has been made by papers with emphasis on the typical microstructures of PBF, DED, and conventional methods [A18]. Other research to bring DED into practical use are proceeding [A19], [30], [A20]. Figure A.1.2 shows the relationship between the technology matures and industrialization indexes. As shown in Fig. A.1.2, DED is now positioned as a technology that has been already matured and industrialized [A21].

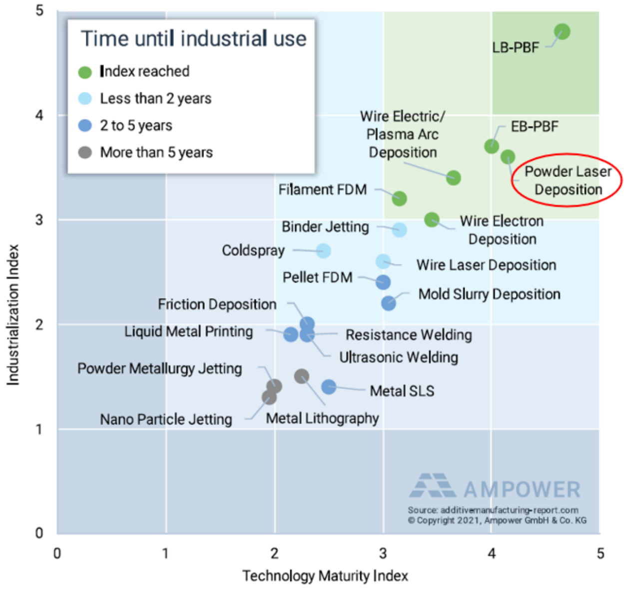

Fig. A.1.2 Comparison of the various AM methodology types until achieving industrial use (AM POWER REPORT 2021 Metal Additive Manufacturing).

A.2 Numerical calculation of stress distribution

The same thermal analysis simulation as that in Section 5.3 was used to select the deposition parameters. The coating process for the drawbar was calculated to check whether the melt pool was properly formed. The analysis conditions are listed in Table A.2.1. The results of the temperature distribution analysis of the drawbar immediately after completion of deposition using these parameters are also shown in Fig. A.2.1.

Table A.2.1 Parameters for the thermal calculation.

Laser power [W]	1600
Feed rate [mm/min]	1000
Layer thickness [mm]	0.6
Laser radius [mm]	1.5
Base material	S45C
Powder material	M2
The number of grids	100 × 100 × 300
Time step [s]	0.001

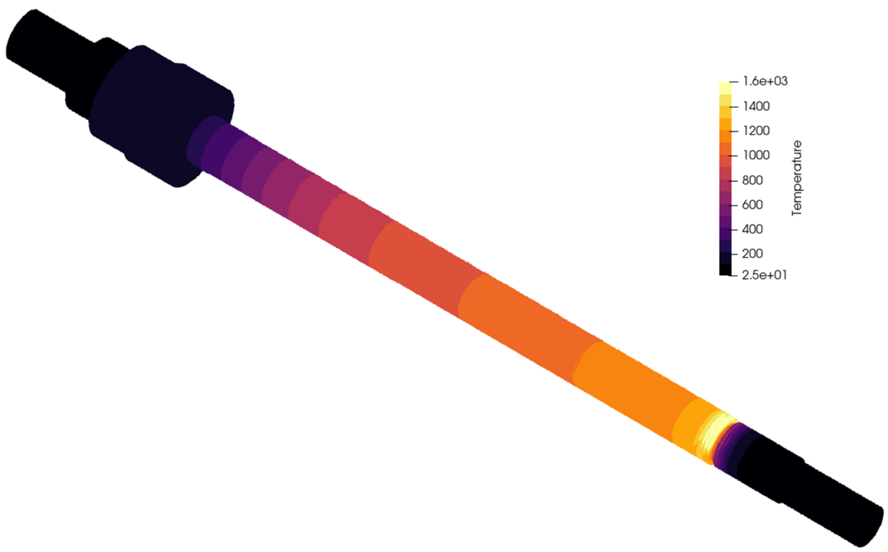

Fig. A.2.1 Temperature distribution of the drawbar immediately after completion of deposition.

The temperature of the area where the laser had been irradiated until just before exceeds the melting point of the base material was approximately 1500 ℃, indicating that a melt pool had been formed. By contrast, the temperature of the area where deposition has already been completed was approximately 1200 ℃ at the maximum, indicating that solidified had already occurred at completion of deposition.

Based on these results, a setting was devised in which the laser power was increased only at the start of deposition, when the base material temperature was low and then maintained at a constant 1600 W. Shield gas and carrier gas flow rates, which are not taken into account in the simulation, were determined separately using past empirical rules.

Thereafter, the stress distribution for the selected parameters was numerically calculated to determine whether there was any risk of cracking or delamination. Ansys additive was used for the numerical analysis. The commercial numerical analysis software allowed the stress to be analyzed while adding deposited portions according to the deposition path. Stress calculations were performed using the settings listed in Table A.2.2. The final stress distribution after 2 min of air cooling on completion of deposition is shown in Fig. A.2.2.

Table A.2.2 Parameters of the stress calculation.

Volume rate [mm^3/s]	105
Volume cluster [mm^3]	18
Print cross-sectional area [mm^2]	0.7 × 1.8
Base material	S45C
Powder material	M2
The number of elements	12761

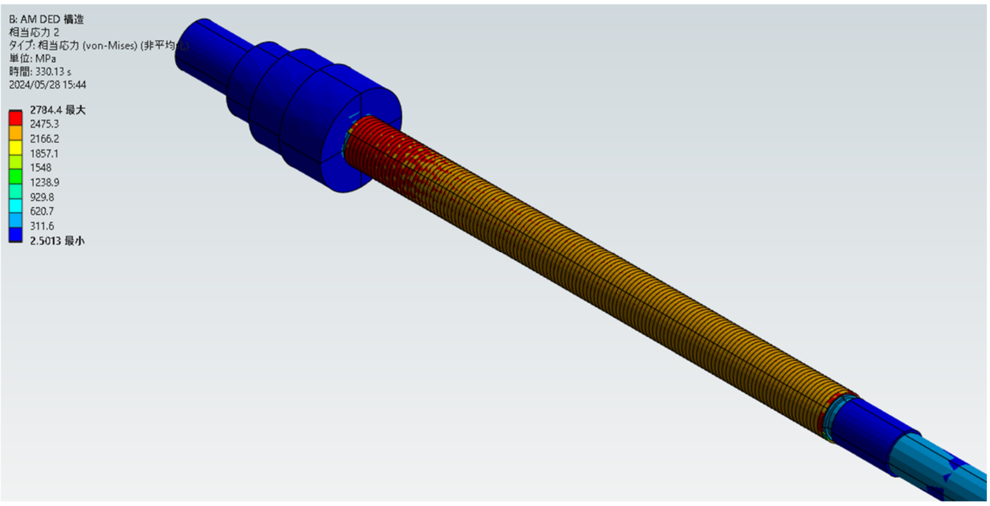

Fig. A.2.2 Stress distribution of the drawbar after completion of deposition.

[A1] K. Ransikarbum, R. Pitakaso and N. Kim, "A Decision-Support Model for Additive Manufacturing Scheduling Using an Integrative Analytic Hierarchy Process and Multi-Objective Optimization," Appl. Sci., vol. 10, p. 5159, 2020.

[A2] A. Bandyopadhyay and K. D. Traxel, "Invited review article Metal-additive manufacturing—Modeling strategies for application-optimized designs," Additive Manufacturing, vol. 22, pp. 758-774, 2018.

[A3] J. J. Lewandowski and M. Seifi, "Metal Additive Manufacturing A Review of Mechanical Properties," Annual Review of Materials Research, vol. 46, pp. 151-186, 2016.

[A4] V. Pusateri, M. Z. Hauschild, S. Kara, C. Goulas and S. I. Olsen, "Quantitative sustainability assessment of metal additive manufacturing: A systematic review," CIRP Journal of Manufacturing Science and Technology, vol. 49, pp. 95-110, 2024.

[A5] Y. Cai, J. Xiong, H. Chen and G. Zhang, "A review of in-situ monitoring and process control system in metal-based laser additive manufacturing," Journal of Manufacturing Systems, vol. 70, pp. 309-326, 2023.

[A6] W. Yue, Y. Zhang, Z. Zheng and Y. Lai, "Hybrid Laser Additive Manufacturing of Metals A Review," Coatings, vol. 14, p. 315, 2024.

[A7] G. Gong, J. Ye, Y. Chi, Z. Zhao, Z. Wang, G. Xia, X. Du, H. Tian, H. Yu and C. Chen, "Research status of laser additive manufacturing for metal: a review," Journal of materials research and technology, vol. 15, pp. 855-884, 2021.

[A8] M. Tebianian, S. Aghaie, N. S. R. Jafari, S. R. E. Hosseini, A. B. Pereira, F. A. O. Fernandes, M. Farbakhti, C. Chen and Y. Huo, "A Review of the Metal Additive Manufacturing Processes," Materials, vol. 16, p. 7514, 2023.

[A9] R. Shanthar, K. Chen and C. Abeykoon, "Powder-Based Additive Manufacturing A Critical Review of Materials, Methods, Opportunities, and Challenges," Adv. Eng. Mater., vol. 25, p. 2300375, 2023.

[A10] AMPOWER, "AMPOWER REPORT 2024 Management Summary," 2024.

[A11] Ministry of the Environment Government of Japan, "Annual Report on the Environment, the Sound Material-Cycle Society and Biodiversity in Japan 2021," 2021.

[A12] A. Liu, X. Jiang, B. Song, K. Chen, X. Xu, G. Yang and W. Liu, "A multi-objective optimization method of directed energy deposition manufacturing process considering carbon emission," Journal of Cleaner Production, vol. 452, p. 142144, 2024.

[A13] M. Santiago-Herrera, E. Igos, J. Alegre, S. Martel-Martín and R. Barros, "Ex-ante life cycle assessment of directed energy deposition based additive manufacturing A comparative gearbox production case study," Sustainable Materials and Technologies, vol. 39, p. e00819, 2024.

[A14] Z. Li, S. Sui, X. Ma, H. Tan, C. Zhong, G. Bi, A. T. Clare, A. Gasser and J. Chen, "High deposition rate powder- and wire-based laser directed energy deposition review," International Journal of Machine Tools & Manufacture, vol. 181, p. 103942, 2022.

[A15] D. Svetlizky, M. Das, B. Zheng, A. L. Vyatskikh, S. Bose, A. Bandyopadhyay, J. M. Schoenung, E. J. Lavernia and N. Eliaz, "Directed energy deposition (DED) additive manufacturing: Physical characteristics, defects, challenges and applications," Materials Today, vol. 49, pp. 271-295, 2021.

[A16] K. S. Ribeiro, F. E. Mariani and R. T. Coelho, "A Study of Different Deposition Strategies in Direct Energy Deposition (DED) Processes," Procedia Manufacturing, vol. 48, p. 663–670, 2020.

[A17] D. Feenstra, R. Banerjee, H. Fraser, A. Huang, A. Molotnikov and N. Birbilis, "Critical review of the state of the art in multi-material fabrication via directed energy deposition," Current Opinion in Solid State and Materials Science, vol. 25, no. 4, p. 100924, 2021.

[A18] Y. Li, Y. Wang, J. Niu, S. Liu, Y. Lin, N. Liu, J. Ma, Z. Zhang and J. Wang, "Microstructure and mechanical properties of M2 high speed steel produced by electron beam melting," Materials Science and Engineering: A, vol. 862, p. 144327, 2023.

[A19] S. Pandey, R. Srivastava and R. Narain, "Mathematical prediction of melt pool geometry and temperature profile for direct energy deposition of 15Cr5Ni SS alloy," Progress in Additive Manufacturing, vol. 8, p. 1127–1140, 2023.

[A20] J. L. Bennett, S. J. Wolff, G. Hyatt, K. Ehmann and J. Cao, "Thermal effect on clad dimension for laser deposited Inconel 718," Journal of Manufacturing Processes, vol. 550–557, p. 28, 2017.

[A21] AMPOWER, "AMPOWER REPORT 2021 Metal Additive Manufacturing," 2021.